Nanoindentation-induced Deformation Mechanisms in Germanium

David John Oliver

A thesis submitted for the degree of
Doctor of Philosophy
of
The Australian National University

November 2008

CERTIFICATE

This thesis, to the best of my knowledge and belief, does not contain any results previously published by another person or submitted for a degree or diploma at any university except where due reference is made in the text.

David J. Oliver

Acknowledgements

I firstly wish to thank my supervisors, Dr Jodie Bradby and Prof Jim Williams, for their expert guidance, patience, and assistance in all aspects of research. Their enthusiasm for doing and communicating quality research has been inspirational. I acknowledge and thank Dr Bradby for performing most of the TEM contained in this thesis.

I sincerely thank Prof Mike Swain of the University of Sydney for sharing the wealth of his expertise on indentation with me, which greatly helped to inform the theoretical interpretation of the results presented here.

I would like to thank Dr Simon Ruffell for carrying out the ion implantation in this thesis, and for helpful discussions of results. I also thank Martin Conway for assistance with ion implantation.

I thank Dr Rui Rao for her assistance in using the Hysitron nanoindenter and Quesant AFM.

I acknowledge Prof Paul Munroe at the University of New South Wales for access to the FIB system and helpful scientific input. Thanks also go to Dr Damien McGrouther and Dr Charlie Kong at the University of NSW for their cheerful and highly capable assistance in the use of the FIB.

My thanks to Dr Brian Lawn and Dr Robert Cook for hosting me at the National Institute of Standards and Technology and sharing with me their formidable combined experience on the topic of indentation fracture. I thank Dr Mark Reitsma, Dr Sanjit Bhowmick, and Dr James Lee for support, company, and experimental assistance during my stay at NIST. I acknowledge the Australian Research Network for Advanced Materials for providing travel support for the visit.

I acknowledge Prof Peter Simpson of the University of Western Ontario for the positron measurements in this study.

I acknowledge Prof Arne Nylansted Larsen for generously providing the thin film Ge on Si samples examined in this thesis.

I am deeply grateful to the people who have supplied support and encouragement over the course of this project. These include my parents, Anna Correll and Nick Oliver, my brother Michael and sister Beth, and my good friends at Graduate House and University House. I am also grateful to my fellow students in Electronic Materials Engineering, and I must particularly thank Bianca Haberl for stimulating discussions and good company on weekend FIB trips, and for performing some of the TEM.

Finally, my deepest gratitude goes to my girlfriend and best friend Hannah Joyce for her solidarity, companionship, and support throughout my PhD, and for proof-reading this thesis.

Abstract

Germanium (Ge), a Group IV elemental semiconductor, is an important electronic material used in many technological applications. Although it is frequently considered to be a classic brittle material, deforming elastically under mechanical stress up to the point of fracture, in practise this is not the case. Instead, under indentation with a sharp tip, plastic deformation plays a dominant role and other deformation mechanisms may be activated. In the literature there is some controversy as to what is the dominant indentation response of Ge at room temperature, shear-induced plasticity or high-pressure phase transformation. This thesis addresses that controversy by investigating the indentation response of germanium over a range of loading regimes and sample preparation conditions. A diverse range of responses is observed, shedding light on the behaviour of Ge at nano- and microscale contact events.

A wide range of techniques has been employed in this work to investigate the sharp contact response of Ge. Instrumented nanoindentation with a sharp diamond tip has been used to introduce mechanical damage at small scales. Features of the indentation force-displacement (P-h) curve can be linked to changes induced in the material. A number of techniques have been applied to characterise the damage produced, including cross-sectional transmission electron microscopy (XTEM), micro-Raman spectroscopy, atomic force microscopy (AFM), scanning electron microscopy (SEM), and focussed ion beam (FIB) analysis. In addition, high-energy ion implantation has been used to introduce structural defects and disorder or to completely amorphise the material.

Loading conditions are found to profoundly effect the deformation response of Ge. Rapid loading rates promote the formation of high-pressure phases during indentation, due to the rate-limited nature of shear plasticity mechanisms. These high-pressure phases transform to amorphous Ge (a-Ge) or metastable crystalline phases on load release. At high maximum load values, cracking becomes an important response. Lateral cracking in the vicinity of the indent is found to cause spallation and debris expulsion, resulting in a dramatic 'giant pop-in' event observed in the P-h curve.

Implantation-induced disorder is found to have a pronounced effect on the mechanical properties of Ge. Implantation-induced defects in crystalline Ge lower the hardness and elastic modulus, suppressing cracking and causing enhanced plasticity and quasi-ductile extrusion. In ion-implanted a-Ge, high-pressure phase transformation is the dominant indentation response. Intriguingly, this phase transformation results in the formation of crystalline Ge on unloading.

Finally, it is found that the deformation response can be altered by confining Ge in the form of a thin film. Thin films of crystalline Ge on Si deform by high pressure phase

transformation, resulting in the formation of a-Ge on unloading. The threshold film thickness at which this occurs is associated with the geometry of the stress fields under the indenter.

These results show that a diverse range of indentation responses are possible in Ge and that the dominant response can be controlled via loading conditions and sample preparation. End phases of a-Ge and Ge-III are obtained under appropriate conditions with novel electronic, optical, and chemical properties. Furthermore, many of the findings here should be generalisable to other technologically important covalent semiconductors, opening new avenues of research.

Contents

1 Introduction **1**

1.1 Literature review . . . 2

1.1.1 High-pressure behaviour of Ge and Si . . . 2

1.1.2 Nanoindentation studies of Ge and Si . . . 4

1.2 Thesis structure . . . 5

2 Experimental Techniques **7**

2.1 Indentation . . . 7

2.1.1 Historical background of hardness testing . . . 7

2.1.2 Nanoindenter operation . . . 9

2.1.3 Nanoindentation Theory . . . 12

2.1.4 Indentation fracture . . . 16

2.2 Ion implantation . . . 18

2.2.1 High-energy ion implantation . . . 19

2.2.2 Theory of ion implantation . . . 20

2.3 Raman microspectroscopy . . . 21

2.3.1 Raman penetration depth . . . 23

2.4 Scanning electron microscopy . . . 23

2.5 Transmission electron microscopy . . . 24

2.6 Focussed ion beam system . . . 25

2.7 Atomic Force Microscopy . . . 26

2.8 Positron Annihilation Spectroscopy . . . 27

3 Rate-dependent indentation behaviour of Ge **29**

3.1 Introduction . . . 29

3.2 Experimental details . . . 30

3.3 Results . . . 31

3.4 Discussion . . . 36

3.5 Concluding remarks . . . 40

4 Nanoindentation of implanted crystalline Ge **41**
4.1 Introduction 41
4.2 Experimental details 42
4.3 Results 43
4.4 Discussion 52
4.5 Concluding remarks 55

5 Nanoindentation of amorphous Ge **57**
5.1 Introduction 57
5.2 Experimental details 59
5.3 Results 60
5.4 Discussion 63
5.5 Concluding remarks 66

6 Nanoindentation of germanium thin films on silicon **67**
6.1 Introduction 67
6.2 Experimental and Modelling Procedures 67
6.3 Results 69
6.4 Discussion 80
6.5 Concluding remarks 82

7 Giant pop-ins in Ge and Si **85**
7.1 Introduction 85
7.2 Experimental details 86
7.3 Results and interpretation 86
7.3.1 Giant pop-ins in Ge 86
7.3.2 Observational details and mechanisms of giant pop-in 90
7.3.3 Phase transformation in Ge after giant pop-in 99
7.4 Concluding remarks 104

8 Synopsis and concluding remarks **107**
8.1 General observations 107
8.2 Deformation mechanisms in germanium 109
8.3 Future directions 112

List of Figures

1.1 Schematic of the high-pressure phase transformations of crystalline Ge under diamond-anvil cell (DAC) loading. 3
1.2 Metallic transition pressure vs indentation hardness for selected elemental and compound covalent semiconductors. 6

2.1 Load vs time functions illustrating (a) continuous loading cycle and (b) partial unload loading cycle. 10
2.2 Schematic of the UMIS-2000 indentation instrument. (Taken from UMIS manual.) 11
2.3 Schematic of the Hysitron transducer. (Taken from Triboindenter manual.) 11
2.4 Schematics of (a) indentation geometry and (b) force-displacement curve, showing key parameters in the Oliver and Pharr analysis. 13
2.5 Schematic of PL test force-displacement data, showing parameters in the Field and Swain analysis. 15
2.6 Schematics of the main modes of cracking during indentation: (A) Hertzian cone cracking, (B) radial cracking, (C) median cracking, (D) full half-penny cracking, and (E) lateral cracking. 17
2.7 Schematic showing the key features of the tandem accelerator. 19
2.8 An energetic ion entering a sample will trigger a displacement cascade. . 20
2.9 (a) Raman spectrum of diamond cubic structure Ge (Ge-I). (b) Raman spectrum of amorphous Ge. (c) Raman spectrum of st-12 structure Ge (Ge-III). 22
2.10 Schematics of focussed ion beam (FIB)-milled transmission electron microscopy (TEM) cross-sections: (a) H-bar cross-section, (b) cross-section for pluck-out. 26
2.11 Schematic of FIB-milled cross-section for viewing with the scanning electron microscopy (SEM) column. 27
2.12 Definition of S-parameter for a Doppler-broadened positron annihilation spectroscopy (PAS) spectrum, $S = A/C$. 28

3.1 Load vs time functions for the Hysitron with (a) a slow loading rate (dP/dh = 0.5 mN·s^{-1} on loading, dP/dh = 10 mN·s^{-1} on unloading), and (b) a fast loading rate (dP/dh = 900 mN·s^{-1} on loading, dP/dh = 10 mN·s^{-1} on unloading). 30
3.2 Load vs time plots for UMIS high loading rate indents. (a) Test with a rapid unloading rate (dP/d$h \approx$ 140 mN·s^{-1} on loading, dP/d$h \approx$ 15 mN·s^{-1} on unloading), and (b) a slow unloading rate (dP/d$h \approx$ 165 mN·s^{-1} on loading, dP/d$h \approx$ 0.7 mN ·s^{-1} on unloading). 31
3.3 P-h curves for Hysitron Berkovich indents to 9 mN at different loading rates: (a) loading rate of 1 mN·s^{-1}, (b) loading rate of 150 mN·s^{-1}, with elbow, (c) loading rate of 150 mN·s^{-1}, with pop-out. For all curves the unloading rate is 10 m·s^{-1}. (d) Dependence of measured hardness on loading rate. 32
3.4 P-h curves from a high loading rate indent with the Hysitron with a hold period of 5 s at maximum load. 33
3.5 Raman spectra from indents made with the UMIS. (a) Spherical tip, dP/dh $\approx$ 15 mN·s^{-1} on loading, dP/d$h \approx$ 1 mN·s^{-1} on unloading. (b) Spherical tip, dP/dh 100 mN·s^{-1} on loading, dP/d$h \approx$ 1 mN·s^{-1} on unloading. For all plots, solid lines are Raman spectra taken from indents (made under the same conditions in each plot), dotted line is the spectrum of pristine Ge. 34
3.6 Raman spectra from indents made with the UMIS. (a) Spherical tip, dP/dh 100 mN·s^{-1} on loading, dP/d$h \approx$ 15 mN·s^{-1} on unloading. (b) Berkovich tip, dP/dh 100 mN·s^{-1} on loading, dP/d$h \approx$ 15 mN·s^{-1} on unloading. For all plots, solid lines are Raman spectra taken from indents (made under the same conditions in each plot), dotted line is the spectrum of pristine Ge. 35
3.7 XTEM from a high loading rate UMIS Berkovich indent (dP/d$h \approx$ 60 mN·s^{-1} on loading, dP/d$h \approx$ 15 mN·s^{-1} on unloading). (a) BF micrograph of the whole indent, showing phase transformation and shear damage. (b) SADP from the phase-transformed zone. (c) SADP from pristine material for comparison. 37
3.8 BF micrograph of a different rapid loading rate UMIS Berkovich indent (dP/d$h \approx$ 140 mN·s^{-1} on loading, dP/d$h \approx$ 15 mN·s^{-1} on unloading). Inset: SADP from the phase-transformed zone. 38
3.9 BF image of a high loading rate UMIS spherical indent (dP/d$h \approx$ 165 mN·s^{-1} on loading, dP/d$h \approx$ 1 mN·s^{-1} on unloading). Inset: SADP from the phase-transformed zone. 38

4.1 TRIM simulation results for 800 keV Ge ions implanted in Ge to 3×10^{13} ions·cm^{-2}. (a) Distribution of implanted ions. (b) Distribution of vacancies generated during implantation. 42
4.2 XTEM of implanted layers. (a) BF image of 1×10^{13} ions·cm^{-2} dose implanted layer. (b) BF image of 3×10^{13} ions·cm^{-2} dose implanted layer. 43
4.3 Results of positron analysis on as-implanted and annealed samples. (a) S parameter vs. positron energy for all doses, as-implanted and annealed at 200 °C. (b) S parameter vs. positron energy for 3×10^{13} ions·cm^{-2} dose, annealed at 3 different temperatures. 45
4.4 AFM micrographs of indents to 100 mN. (a) Indent in unimplanted Ge (10×10 μm image). (b) Indent in sample implanted to 3×10^{13} ions·cm^{-2} and unannealed (7×7 μm image). 46
4.5 Raman spectra from pristine Ge and from the 3×10^{13} ions·cm^{-2} dose as-implanted sample. 47
4.6 XTEM of indent to 100 mN in 3×10^{13} ions·cm^{-2} as-implanted sample. (a) BF image of indent. (b) SADP from indent damage region within implanted layer. (c) SADP from implanted layer outside indented region. (d) SADP from underlying pristine Ge. 48
4.7 (a) BF TEM image of indent to 100 mN in 3×10^{13} ions·cm^{-2} implanted 200 °C annealed sample. (b) Enlargement of damage region, showing microcrack. (c) BF TEM image of a different 100 mN indent in the same sample. 49
4.8 Nanoindentation hardness vs implanted ion dose for as-implanted and annealed Ge samples. 50
4.9 Elastic modulus E vs implanted ion dose for as-implanted and annealed Ge samples. 51
4.10 (a)P-h curve to 50 mN in unimplanted Ge. (b) P-h curve to 50 mN in 3×10^{13} ions·cm^{-2} as-implanted Ge. 51
4.11 Raman spectra from sample regions that were indented to 100 mN and subsequently implanted. 52

5.1 Schematic of high-pressure phase transformations of a-Ge observed in diamond-anvil cell (DAC) experiments. 58
5.2 P-h curves for indents in a-Ge samples, (a) unrelaxed and (b) relaxed. . . 60
5.3 P-h curve to 100 mN in unrelaxed a-Ge sample. 60
5.4 P-h curve to 50 mN, with a 30 s hold at maximum load, in unrelaxed a-Ge sample. 61

5.5 Hardness vs implanted dose for unrelaxed and relaxed a-Ge samples. . . 62

5.6 Raman spectra taken from indents in a-Ge, (a) unrelaxed and (b) relaxed. Undeformed a-Ge spectra shown for comparison. 62

5.7 TO linewidth measured from Raman spectra for unindented specimens plotted vs implantation dose, for both unrelaxed (as-implanted) and relaxed (250 °C annealed) specimens. 63

5.8 (a) BF XTEM micrograph of an indent to 60 mN in unrelaxed a-Ge. (b) SADP from the amorphous layer, away from the indent. (c) SADP from recrystallised region under indent. 64

5.9 (a) BF XTEM micrograph of an indent to 60 mN in relaxed a-Ge. (b) SADP from the amorphous layer away from the indent. (c) SADP from recrystallised region under indent. 64

6.1 Load-50% partial unload P-h curve for bulk Ge, showing departure from elastic response at yield load P_c. 69

6.2 Raman spectra for indents in thin film samples: (a) 50 nm film, (b) 100 nm film, and (c) 200 nm film. 70

6.3 XTEM micrograph of 100 mN indent in 50 nm thin film Ge on Si sample, (a) whole indent and (b) close-up of film. Inset: selected area diffraction pattern (SADP) from transformed region (Si and Ge). 72

6.4 XTEM micrograph of 100 mN indent in 100 nm thin film Ge on Si sample, (a) whole indent and (b) close-up of film, with SADP inset. 73

6.5 XTEM micrograph of 100 mN indent in 200 nm thin film Ge on Si sample, (a) whole indent and (b) close-up of film, with SADP inset. 74

6.6 XTEM of 100 mN indent in 400 nm Ge film on Si. (a) Bright-field (BF) image, showing twinning and punched-out dislocations. (b) Dark-field (DF) image taken using the boxed reflection in the inset diffraction pattern, showing twins. 75

6.7 SEM micrographs of 100 mN indents in thin film Ge on Si samples. (a) 50 nm film. (b) 100 nm film. (c) 200 nm film. 76

6.8 P-h curves to 50 mN and 100 mN in thin Ge films on Si. (a) 50 nm film, (b) 100 nm film, (c) 200 nm film, and (d) 400 nm film. 77

6.9 Derivative of 100 mN P-h curve in Fig. 6.8(b), plotted versus depth. . . . 77

6.10 Isobaric plots of (a), (c), (e) hydrostatic stress and (b), (d), (f) von Mises stress (shear stress) beneath a spherical indenter, for different combinations of tip radius, film thickness, and applied load. (g) Shear yield point and hydrostatic yield point plotted as a function of Ge film thickness, for the 4.3 μm tip. 78

6.11 Deformation mechanism diagram, showing dominant initial deformation mechanism in Ge films on Si as a function of indenter tip radius and Ge film radius. Circles show critical transition points obtained from Elastica simulations. The boundary between the two regions is given by the relationship $R_c \approx 70h_f$. 79

7.1 (a,b) Force-displacement curves for 350 mN indents in Ge, created using identical test parameters. Curves in (a) feature a giant pop-in event. Curve in (b) features only small pop-ins. 87

7.2 P-h curves for Ge to 500 mN. 88

7.3 Histograms of (a) the load at which the giant pop-in occurs, and (b) the magnitude of the giant pop-in for 400 indents made with a spherical tip of radius 4.3 μm loaded to 500 mN. 88

7.4 Partial unload results for Ge. (a) Force-displacement data. (b) Contact pressure as a function of load, calculated by Field and Swain method. . . 89

7.5 SEM images of 350 mN load indents: (a) one of the indents in Fig. 7.1(a) (giant pop-in) and (b) indent in Fig. 7.1(b) (no giant pop-in). 90

7.6 (a) Force-displacement curve for 350 mN Ge indent featuring giant pop-in. (b) FIB ion-beam image (prior to Pt deposition) of the indent. (c) FIB electron-beam cross-sectional image of indent (a). (d) Force-displacement curve for a 350 mN indent with no giant pop-in. (e) FIB ion-beam image of the indent. (f) FIB electron-beam cross-sectional image of indent (d). . 91

7.7 (a) P-h curves for Si to 900 mN. (b) Top-down and (c) cross-sectional FIB images of an indent in Si to 550 mN that has undergone a giant pop-in. 93

7.8 Optical micrographs of 350 mN indents: (a) with a large maximum pop-in (1.96 μm), (b) with a small maximum pop-in (0.17 μm). 94

7.9 The amount of debris around 350 mN indents plotted against the size of the largest pop-in for the indent. The dotted line is a guide for the eye. . . 94

7.10 Pop-in size as a function of pop-in load for (a) Si and (b) Ge. Points are experimental data. The solid line is the indenter contact radius, calculated from $a_* = (P_*/\pi H)^{1/2}$. Inset: Schematic showing P_* and h_*. 96

7.11 Schematic representation of the deformation process. (a) a shallow lateral crack opens, which (b) triggers material removal (shaded area), causing the indenter depth to increase by h_x. Initial unloading occurs by elastic recovery in the bulk. (c) When bulk recovery is complete, the tip loses contact with the base of the indent. Beyond this point, the force on the tip is due to lateral plates of material, until the tip is fully unloaded [diagram (d)]. (e) Force-displacement curve schematic, with points in the loading cycle corresponding to the diagrams marked. 99
7.12 (a) Raman spectra from indents in Fig. 7.1(a) (giant pop-in), with spectrum from undamaged Ge for comparison, (b) Raman spectrum from indent in Fig. 7.1(b) (no giant pop-in). 100
7.13 Cross-sectional bright-field TEM of a 400 mN indent without a giant pop-in. Inset: diffraction pattern from deformed region. 102
7.14 a) A multiple-loading (5 x 200 mN) P-h curve for Ge, featuring a giant pop-in. b) Raman spectra from the indent and from undeformed Ge. c) XTEM image of the indent, with inset SADP from region directly below indent showing the presence of a phase-transformed amorphous zone. . . 103

8.1 Schematic of elastic stresses (shear stress and hydrostatic stress) as a function of indenter load during an indentation test and point of intersection with yield stresses, illustrating the case for c-Ge at moderate loading rates. 110
8.2 Schematic of elastic stresses and yield stresses for various cases: (a) c-Ge indented at rapid loading rates, (b) ion-implanted c-Ge with defects, (c) amorphous Ge, (d) thin film Ge. 111

Table of acronyms

a-Ge	amorphous Ge
a-Si	amorphous Si
AFM	atomic force microscopy
BSE	back-scattered electron
BF	Bright field
c-Ge	crystalline Ge
c-Si	crystalline Si
DAC	diamond anvil cell
DF	Dark field
DP	diffraction pattern
DLTS	deep-level transient spectroscopy
FESEM	field-emission SEM
FIB	focussed ion beam
hda-Ge	high-density amorphous Ge
LVDT	linear variable differential transformer
MEMS	microelectromechanical systems
NEMS	nanoelectromechanical systems
PAS	positron annihilation spectroscopy
SADP	selected area diffraction pattern

SEM scanning electron microscopy

TEM transmission electron microscopy

UMIS ultra-micro indentation system

XTEM cross-sectional transmission electron microscopy

Publications

1. D. J. Oliver, J. E. Bradby, J. S. Williams, M. V. Swain and P. Munroe. Thickness-dependent phase transformation in nanoindented germanium thin films. *Nanotechnology* 19(47):475709, 2008.

2. D.J. Oliver, B.R. Lawn, R.F. Cook, M.G. Reitsma, J.E. Bradby, J.S. Williams and P. Munroe. Giant pop-ins in nanoindented silicon and germanium caused by lateral cracking. *Journal of Materials Research* 23(2):297-301, 2008.

3. D. J. Oliver, J.E. Bradby, J.S. Williams, M.V. Swain, D. McGrouther, and P. Munroe. Indentation-induced damage mechanisms in germanium. *Mater. Res. Soc. Symp. Proc.* 983E:0983-LL08-02, 2007.

4. D.J. Oliver, J.E. Bradby, J.S. Williams, M.V. Swain and P. Munroe. Giant pop-ins and amorphization in germanium during indentation. *Journal of Applied Physics* 101(4):043524, 2007.

CHAPTER 1

Introduction

Germanium (Ge) is a semiconductor with a long history in electronic applications. It was used by John Bardeen and Walter Brittain to produce the first point-contact transistor at Bell Laboratories in 1947, and later to manufacture the first junction transistors. [1] The development of high-purity sources allowed silicon (Si) to displace Ge as the dominant semiconductor material; silicon has a higher temperature of operation and lower leakage currents. After the development of integrated circuits, the stable oxide of Si was another point in its favour. In recent times, however, Ge has made a comeback. Ge and Si-Ge alloys are being used in new high-speed processors, due to higher mobilities and compatibility with many existing Si processing methods. [2,3] With the expansion of new high-k dielectric materials, the instability of the native Ge oxide becomes less of an issue. [4] Ge, with a smaller band-gap than Si, is also increasingly utilised for integrated optoelectronics applications. [5,6]

Mechanical behaviour is a key technological consideration. With the growth of nanotechnology and the push to ever-smaller functional devices the deformation behaviour of materials at microscale and nanoscale contacts is an increasingly important topic. At small-scale contacts, behaviours emerge that are absent or hidden at larger scales. Understanding these behaviours is critical for designing micro- and nanoelectromechanical systems (MEMS and NEMS), and predicting how devices will respond to handling, machining, impact, wear, and the presence of debris particles during manufacture and use.

The ideal tool for studying small-scale contact deformation is instrumented indentation, or 'nanoindentation'. In an indentation test a sharp, hard tip (usually made from diamond) is pressed into the surface of a specimen. Due to the mixed stress state induced, this conceptually simple procedure can generate a wide variety of deformation modes in the material, such as elastic deformation, dislocation slip, mechanical twinning, high-pressure phase transformation, fracture and spallation. Ge is noteworthy in that it displays all of those modes of deformation under different loading conditions. Indentation acts as a simple and accessible model for more complex and realistic contact processes.

The development of nanoindentation over the past two decades has opened a window

into microscale and nanoscale contacts by allowing accurate testing at very low forces and depths. Analysing the deformation modes operating at such small contacts is challenging, but here too new techniques have been successfully applied. Scanning electron microscopy (SEM) and atomic force microscopy (AFM) can provide high-resolution images of the surface morphology of contacts. Raman microspectroscopy and TEM with the aid of FIB sample preparation provide information on damage within the material. The utility of these methods relies upon their ability to selectively examine very small volumes of material.

The focus of this work has been the nanoindentation response of Ge. As detailed in the literature review below, Ge is unique in that it is susceptible to both shear-dominated and hydrostatic phase transition-dominated deformation behaviour within different loading regimes and sample preparation conditions. Despite this, there have been relatively few published nanoindentation studies on Ge, compared to the very large body of literature on Si. This thesis presents an extensive study on the behaviour of Ge under a range of conditions, from the onset of plasticity through to fracture at very high loads. A variety of forms of Ge is also examined, including thin-film, ion-implanted, and amorphous structures. The diversity of responses observed illustrates the richness and complexity of small-scale contact processes.

1.1 Literature review

1.1.1 High-pressure behaviour of Ge and Si

Throughout this literature review, work on both Ge and Si will be covered. Both materials are often investigated in the same study, and a comparison between them is frequently instructive.

It was first reported by Minomura and Drickamer that at elevated hydrostatic stresses in a diamond anvil cell (DAC) test, semiconducting Ge and Si undergo a sharp transition to a conductive metallic phase. [7] This conductive phase was shown for both materials to have the β-tin structure, a tetragonal sixfold coordinated structure. [8] The stable phase at ambient pressure and temperature is diamond cubic, referred to as Ge-I and Si-I; the β-tin phase is referred to as Ge-II and Si-II. Later studies with more accurate pressure calibration found the transition pressure under pure hydrostatic stress to be 10.6 GPa for Ge and 12.5 GPa for Si. [9, 10] A component of shear stress can lower the transition pressure by 3 GPa or more, [9, 11] an important point when considering indentation tests in which large shear stresses are inevitably present.

The diamond-cubic $\rightarrow$ β-tin phase transition in Ge and Si is irreversible at room tem-

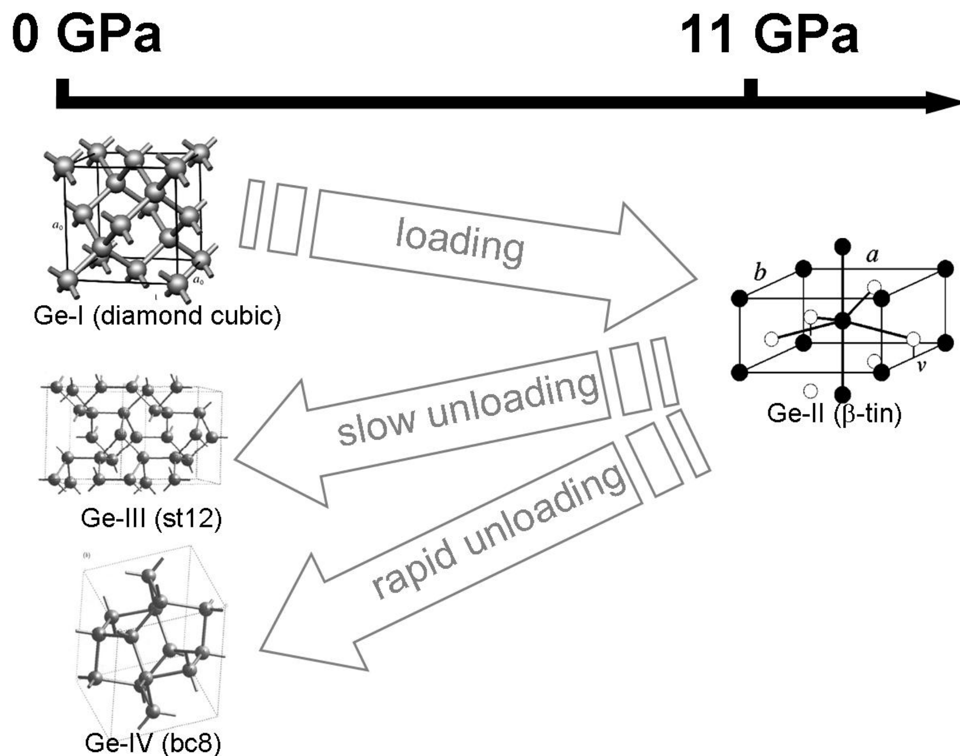

Figure 1.1: Schematic of the high-pressure phase transformations of crystalline Ge under diamond-anvil cell (DAC) loading.

perature. Upon release of pressure, the β-tin phase transforms to one of several metastable crystalline phases. These phases share the properties of having complex structures with large unit cells and a density intermediate between diamond-cubic and β-tin. The sequence of transformations is shown in Fig. 1.1. In Ge, the predominant phase on unloading is the st12 structure, a simple tetragonal structure with 12 atoms in the unit cell, labelled Ge-III. [12] Ge-III has a lifetime measured in years at room temperature, but anneals rapidly to diamond-cubic Ge-I at temperatures of 100-200 °C and above. [13] On very rapid depressurisation (10 GPa·s^{-1}), Ge-II transforms to Ge-IV with the bc8 structure, a body-centred cubic structure with 8 atoms in the unit cell. [14] This phase is unstable at room temperature, and transforms within a day to diamond-hexagonal Ge-V. [14] In Si, the predominant phase on unloading, Si-III, also has the bc8 structure. [12, 15] Like Ge-III, Si-III is metastable with a long lifetime at room temperature, but is unstable at moderately elevated temperatures. Metallic Si-II does not transform immediately to Si-III on unloading, but passes through an intermediate phase, Si-XII, which has the r8 rhombohedral structure. [16] This phase is normally unstable at ambient pressure, but can be stabilised by the presence of shear stresses.

1.1.2 Nanoindentation studies of Ge and Si

Ge and Si are commonly considered to be classic brittle materials, deforming elastically up to the point of failure by fracture. This is true in a uniaxial tensile strength test; in an indentation test, however, the large component of hydrostatic stress suppresses fracture, allowing Ge, Si, and other brittle materials to plastically deform at room temperature.

It was first proposed by Gridneva et al. in 1972 that Ge and Si could undergo a high-pressure phase transition during indentation, in order to account for a low-temperature 'plateau' in the microhardness vs temperature relationship for each material. [17] Gridneva *et al.* also performed electrical measurements demonstrating a reversible resistance drop in Si directly beneath the indenting tip. It was noted that the hardness of Ge and Si at room temperature ($\sim$8 GPa and $\sim$ 12 GPa respectively) is close to the critical pressure for the phase transition. [17, 18] Further evidence for a phase transformation was found by Clarke *et al.* in 1988, who observed amorphous material by TEM in residual indents in Ge and Si, and in addition observed a resistance drop similar to that of Gridneva *et al.* [19] After this, interest in the indentation response of Si and Ge swelled, motivated partly by the rising commercial importance of MEMS systems and facilitated by the development of depth-sensing nanoindentation, which has proved to be an ideal tool for investigating indentation-induced phase transformations.

For Si, nanoindentation studies have broadly confirmed the view that hardness is controlled by the β-tin phase transition. [20] Si-III and Si-XII phases have been observed in indents with the use of TEM and Raman microspectroscopy. [21–23] The phase transition has been shown to affect the nanoindentation P-h curve of Si: the formation on unloading of Si-III and Si-XII causes a pop-out in the P-h curve, whereas the formation of amorphous Si (a-Si) causes an elbow. The transformation of Si-II to a-Si which is not observed in DAC experiments is thought to be caused by the small transformed volume and relatively rapid unloading rates preventing the nucleation and growth of the Si-III and -XII phases. Shear stress may also play a role. Phase transformation also plays a role in scratching [24] and machining [25] processes.

For Ge, the picture is less clear. Kailer *et al.* reported the presence of amorphous Ge (a-Ge) and Ge-III phases in Vickers microindents. [26] However, a later Raman study by the same group, on nanoindents in Ge, found phase transformation to be weak or entirely absent in most cases. [27] An electrical resistance study on Ge and Si using nanoindentation confirmed the resistance drop observed by Clarke *et al.* [28] A TEM study by Lloyd *et al.* of nanoindents in Ge reported the observation of a 'transformed zone' beneath the indent, which was attributed to a high-pressure phase transformation; however, they report that the zone contains mainly fcc Ge (Ge-I), making its identification as a 'transformed zone' somewhat confusing. [29] A combined TEM and Raman study by Bradby

et al. found no evidence of phase transformation after nanoindentation, and instead identified twinning as the primary deformation mechanism. [30] Most recently, Jang *et al.* found that transformed phases could be reproducibly generated in nanoindented Ge, but only when a cube-corner indenter was used and only at higher loading rates. [31] Thus there is a discrepancy between studies that observe a phase transformation in indented Ge, and those that do not. This discrepancy has been attributed to various factors including tip geometry, maximum load, loading rate, and sample preparation, but no clear explanation has been established.

Gilman predicted in 1992 that a metallic phase transformation occurred during indentation, not only for Si and Ge, but for a wide range of semiconducting materials. [32] This prediction was based on a correlation between a theoretically determined critical transition pressure and microindentation hardness. Nanoindentation studies on a number of III-V and II-VI semiconductors have not supported Gilman's prediction, instead showing shear deformation mechanisms of twinning and slip to predominate in those materials. [29, 33–35] The failure to observe phase transformation stems from the fact that for these materials, the critical metallic transition pressure tends to lie well above the material hardness as illustrated in Fig. 1.2, and thus sufficient pressures for phase transition are not achieved during an indentation test. This is equivalent to saying that shear-related mechanisms offer an easier deformation pathway than densification by phase transformation during indentation in these materials. For Ge, the metallic transition pressure lies just above the hardness, suggesting that shear deformation is favoured but phase transformation is possible during indentation under the right conditions.

1.2 Thesis structure

This thesis attempts to redress the gaps identified in the literature and provide a fuller understanding of the indentation responses of germanium. The structure of the thesis is as follows. Details of the experimental techniques used in this project and their underlying theory are given in Chapter 2. In Chapter 3, the effect of loading rate on the nanoindentation response is investigated. Rapid loading rates are found to favour phase transformation in Ge, due to the differing rate sensitivities of the available deformation mechanisms.

In Chapters 4 and 5, ion implantation is employed to modify the atomic structure of Ge. The indentation response in a defect-rich crystalline layer is investigated in Chapter 4. As-implanted material has a reduced hardness. Defect evolution after thermal annealing reduces this effect. The mechanical behaviour of fully amorphous Ge is investigated in Chapter 5. Unlike crystalline Ge (c-Ge), a-Ge is found to deform via phase transformation under all loading conditions.

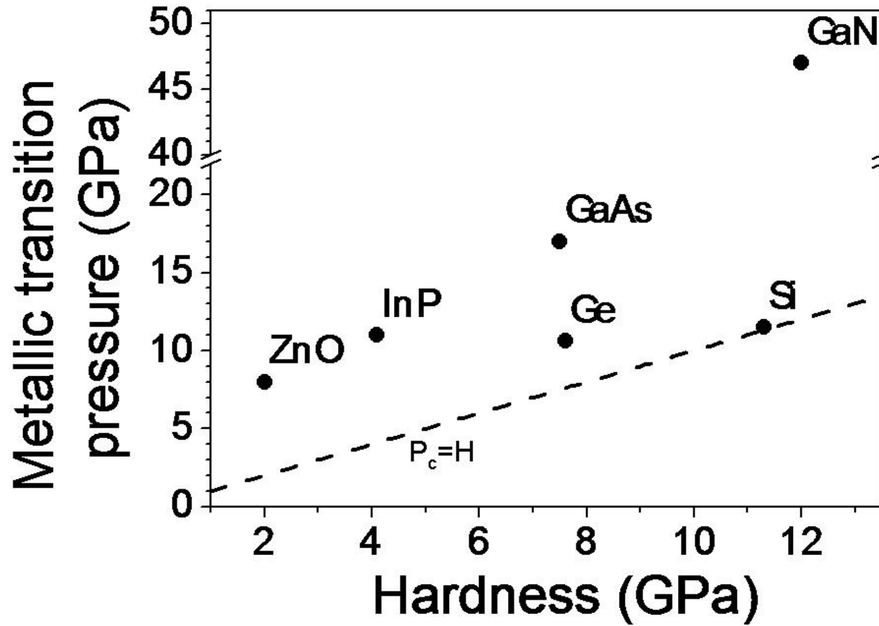

Figure 1.2: Metallic transition pressure vs indentation hardness for selected elemental and compound covalent semiconductors. Values from Ref. [36]. The dotted line is where transition pressure is equal to hardness.

Thin film Ge is investigated in Chapter 6. For thin sub-100 nm films, indentation-induced phase transformation is observed. Indentation of Ge at higher loads is investigated in Chapter 7. A ‘giant pop-in’ event occurs which is shown to involve spallation and catastrophic material removal. Finally, conclusions and directions for future work are presented in Chapter 8.

CHAPTER 2

Experimental Techniques

This chapter will describe the operation and principles of the key experimental techniques used in this thesis. The first and most central technique to be outlined is nanoindentation, also known as instrumented indentation, which was used in this study to introduce plastic deformation, phase transformation, and cracking into a highly localised region of the sample of interest. High-energy ion implantation was used as a part of the study to modify the near-surface region of samples and examine the interaction with indentation processes. A number of techniques were used to characterise the effects of nanoindentation and ion implantation, in particular Raman microspectroscopy, SEM, TEM, and AFM. Finally a FIB system was used to produce thin cross-sectional samples for TEM and cross-sections for SEM imaging of cracking.

2.1 Indentation

2.1.1 Historical background of hardness testing

The concept of hardness, as a material property, is probably equally old as humanity's usage of materials. It is intuitively meaningful to describe a material as 'hard' or 'soft.' However, it is more difficult to put hardness on a quantitative footing. Hardness can be broadly defined as 'the resistance of a material to permanent (plastic) deformation.' Hardness is more difficult than other mechanical properties to relate to fundamental material properties, because it depends in general on the detailed material microstructure, as well as, to an extent, the method by which it is measured. However, it is of undeniable technological significance, which is why it is so widely used and widely measured.

The first significant attempt to put hardness on a semi-quantitative footing was made by Friedrich Mohs, who developed the Mohs scale of hardness in which different minerals are ranked on a scale of 1 to 10 according to their scratch resistance. [37] The Mohs scale suffers from several flaws: it gives no sense of the 'absolute' magnitude of the hardness, and it is biased towards softer materials, so that the majority of technologically

useful materials are clustered close to the top of the scale. It does, however, capture an important quality of hardness: when two bodies are brought into contact, the softer of the two is more likely to undergo permanent plastic deformation.

New hardness tests based on indentation emerged in the early 20th century in response to industrial requirements. Amongst these were the Brinell, Rockwell, Vickers, and Knoop tests. [38] Although these tests differ in the indenter geometry used and the details of the testing procedure, they all rest on the principle of applying a hard indenter to a specimen using a fixed maximum load, and measuring the dimensions of the resulting permanent impression in the specimen. The hardness value is then given in terms of the ratio of the applied force to the dimension of the impression. The basic underlying definition of hardness is:

$$H = P/A \tag{2.1}$$

where H is hardness, P is the maximum applied load, and A is the (projected) area of the residual impression. [39]

Technological progress in indentation testing has been driven largely by the desire to measure properties at smaller and smaller characteristic dimensions: thin coatings, fine-grained structures, microstructural components, etc. This requires that the scale of contact deformation during the test be reduced accordingly. A commonly-cited rule of thumb for layered systems is that the indentation depth must be less than $1/10$ of the layer thickness to avoid substrate influence on the measured hardness. [40] The first move in this direction was microindentation, in which an optical microscope is used to measure the dimensions of the contact impression which is too small to be accurately measured with the naked eye.

As indentation moved to smaller scales, measurement of the contact impression by optical microscopy became increasingly difficult and inaccurate. Alternative microscopy methods such as SEM were found to be prohibitively time-consuming and costly. To eliminate the need for direct measurement of the contact impression, instrumented indenters were developed in the 1980s. These instruments, now commonly known as nanoindenters, measure applied force and indenter penetration depth continuously throughout the loading cycle of an indentation test. Methods based on a physical analysis of the indentation process have been developed to extract hardness, as well as elastic modulus, from the resulting data. Increasing sensitivity and improved noise reduction techniques now allow current state-of-the-art instruments to measure properties of structures with dimensions as small as 10s of nms, and modern nanoindenters share some of capabilities of atomic force microscopes. Interestingly the difficulties with high resolution microscopy that motivated the development of nanoindenters have been overcome to an extent. Microscopy of the

residual indent is now routinely carried out.

2.1.2 Nanoindenter operation

In a typical nanoindentation test, a sharp tip made from a hard material, usually diamond, is pressed into the sample to be tested. The load applied and the displacement of the tip into the sample are measured continuously throughout the cycle of load application and release. From this data the mechanical properties of the sample can be extracted. The key requirement for accurate measurement is that the load and displacement are measured with a high resolution. This demands high performance components. In practice, the force and displacement resolutions of an instrument in use are usually limited by electrical and mechanical noise in its environment. Steps are taken to limit the effects of noise. Other requirements are a stiff instrument frame, to minimise machine compliance, and a stable temperature environment, to minimise thermal drift. [41]

The nanoindenters used in this study can be operated in either closed loop or open loop mode. In closed loop mode, a feedback loop is used to obtain a precise value of load (or depth) at each measured increment on the loading cycle. In open loop mode, no feedback is used, the load signal is simply ramped up at a fixed rate. The closed loop mode gives more control over the loading cycle; the open loop mode allows a higher rate of data collection, and allows higher maximum loading rates.

The simplest loading cycle is to increase the load, at some constant loading rate, from zero to some maximum load; then to release the load at a constant rate until zero load is reached. This is termed a continuous load (CL) cycle [Fig. 2.1(a)]. An alternative is to partially release load after each loading increment: this is termed a partial unload (PL) cycle [Fig. 2.1(b)]. Data from a CL test can be analysed with the Oliver and Pharr method, which will be described shortly, to provide a value of hardness and of elastic modulus. The force-displacement curve from a CL test may also show qualitative features such as pop-ins and pop-outs that mark discrete events during the loading cycle. PL test data is generally used in combination with the Field and Swain method, also described in the following sections, to obtain a series of hardness values as a function of indenter penetration into the sample. PL data can also be used to detect the onset of plastic deformation.

Two nanoindentation instruments were used in this study. The first, the UMIS-2000 (CSIRO, Lindfield, Australia) was used to create indents in the range 50-1000 mN. The second, the Hysitron Triboindenter (Minneapolis, USA) was used to create smaller indents in the range 0.1-10 mN. The operating principles of each instrument will be briefly described here.

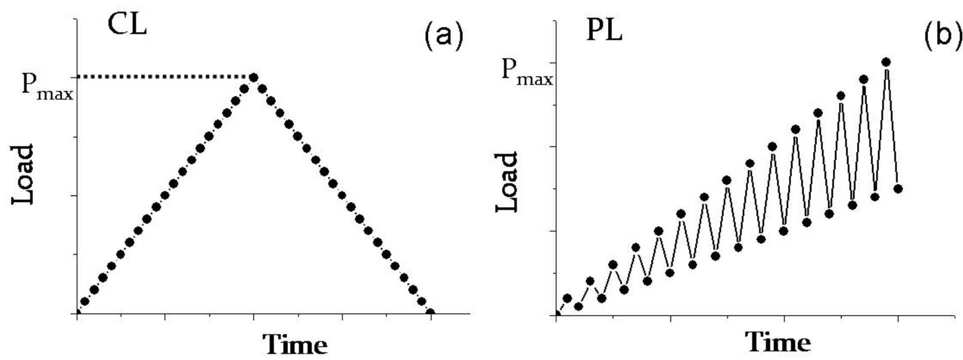

Figure 2.1: Load vs time functions illustrating (a) continuous loading cycle and (b) partial unload loading cycle.

UMIS-2000

Fig. 2.2 illustrates the operation of the UMIS-2000. During a test, a piezoelectric actuator applies load to the main carriage. Leaf springs transfer force from the carriage to the indenter shaft. A linear variable differential transformer (LVDT) measures the displacement of the indenter shaft relative to the carriage: from this, using the spring constant of the leaf springs, the force on the indenter tip can be calculated. Another LVDT attached to the frame of the indenter measures the depth.

Hysitron Triboindenter

The most important component in the Hysitron is the transducer, shown in Fig. 2.3. The transducer consists of two parallel outer electrodes, called drive plates, and a central plate in between. The indenter shaft is attached to this central plate. AC signals $180°$ out of phase are applied to the drive plates. Because the plates are parallel and closely spaced, the electric field potential between them will vary linearly with displacement. Since the potential of the central plate will vary according to its position relative to the drive plates, the output signal can be measured to determine the displacement.

Force on the indenter is supplied by applying a large DC bias to the bottom drive plate. This will create an electrostatic attraction with the central plate, pulling it down. The force is calculated from the magnitude of the voltage applied. Forces of up to 10 mN can be applied.

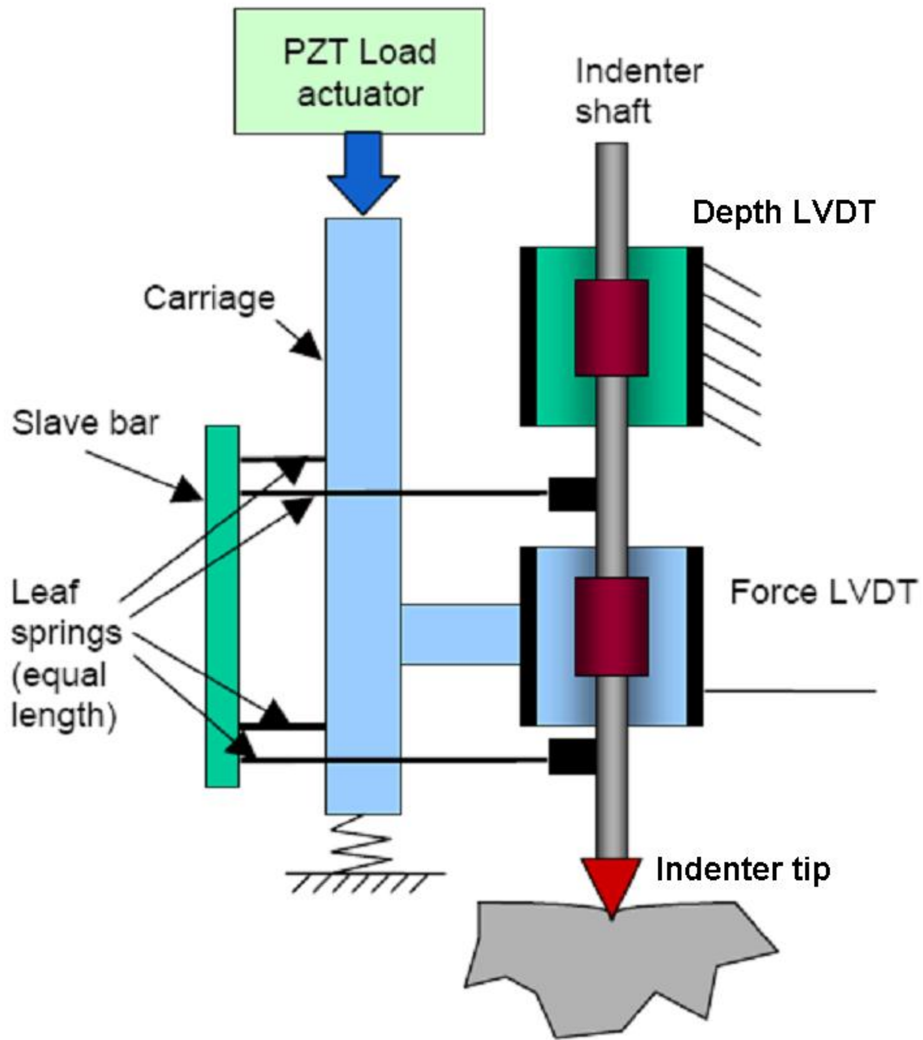

Figure 2.2: Schematic of the UMIS-2000 indentation instrument. (Taken from UMIS manual.)

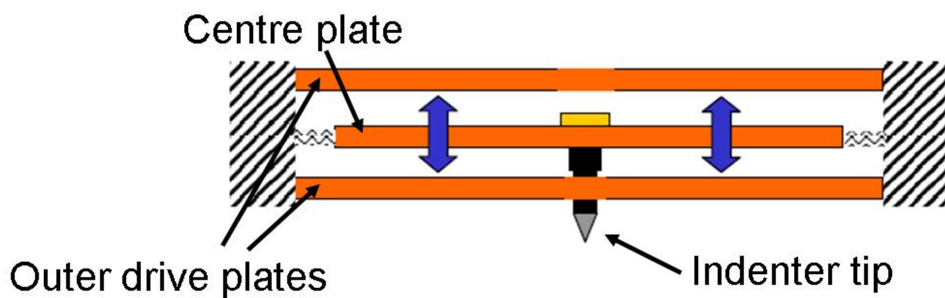

Figure 2.3: Schematic of the Hysitron transducer. (Taken from Triboindenter manual.)

2.1.3 Nanoindentation Theory

Oliver & Pharr method

The most commonly used method to analyse nanoindentation data was developed by Oliver and Pharr in 1992. [42, 43] It was developed for pyramidal indenters, but applies equally well to spherical and other indenter geometries. It is based on the solutions of Sneddon for an elastic half-space indented by a rigid, axisymmetric indenter. [44]

The key assumption made by Oliver and Pharr is that deformation during the unloading cycle is entirely elastic. As a consequence, the area of the residual impression after unloading is approximately equal to the contact area of the indenter at maximum load [Fig. 2.4(a)].

The elastic analysis shows that the depth of the contact area below the free surface, h_s, is given by:

$$h_s = \epsilon \frac{P_{max}}{S} \tag{2.2}$$

where P_{max} is the maximum load, S is the measured unloading stiffness [Fig. 2.4(b)], and ϵ is a geometry-dependent constant that is usually taken as $\epsilon = 0.75$. The contact depth, h_c, is given by $h_c = h_{max} - h_s$, where h_{max} is the total depth. The contact area, A, can then be calculated from:

$$A = F(h_c) \tag{2.3}$$

where $F(h)$ is known as the tip area function. For an ideal tip geometry, the area function is a simple analytical formula; in practice, however, any real tip will deviate from the ideal due to blunting and imperfections. To obtain accurate values with a given tip, the real area function must be calibrated by indenting a sample with known properties, such as fused silica or aluminium. Once the contact area is obtained, the hardness is given by:

$$H = \frac{P_{max}}{A} \tag{2.4}$$

The elastic modulus can be calculated from the unloading stiffness and contact area, through the relation:

$$S = \beta \frac{2}{\sqrt{\pi}} E_{eff} \sqrt{A} \tag{2.5}$$

where E_{eff} is the effective elastic modulus, defined as:

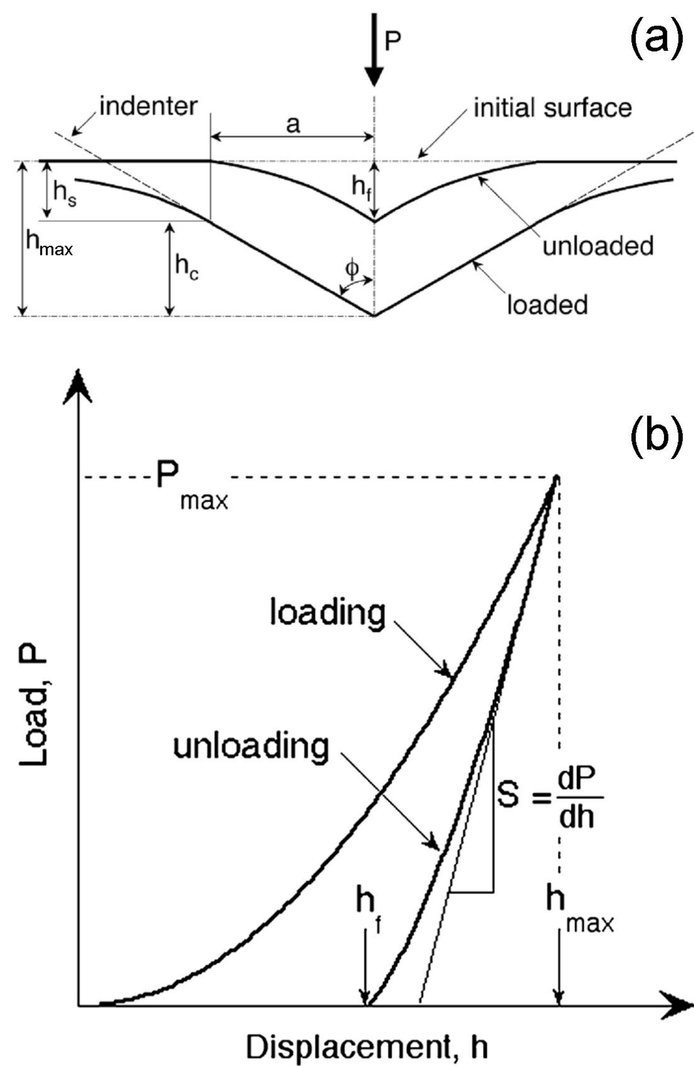

Figure 2.4: Schematics of (a) indentation geometry and (b) force-displacement curve, showing key parameters in the Oliver and Pharr analysis. (Taken from Ref. [43])

$$\frac{1}{E_{eff}} = \frac{1-\nu^2}{E} + \frac{1-\nu_i^2}{E_i} \tag{2.6}$$

The quantities E, ν, E_i, and ν_i are the Young's moduli and Poisson's ratios of the specimen and the indenter respectively. The parameter β in Eq. 2.5 is a dimensionless constant that is usually close to unity. Thus, from nanoindentation test data and a knowledge of the geometry of the indenting tip, the hardness H and Young's modulus E of the indented specimen can be calculated.

Field & Swain method

The analysis developed by Field and Swain is a useful alternative for analysing data from spherical nanoindentation. [45] The chief advantage is that only one unloading data point is needed to perform the analysis. When used to analyse PL data, in which the indenter is unloaded at each step (Fig. 2.5), the hardness (and modulus) can be calculated at each step, giving a profile of hardness/indentation pressure as a function of penetration depth in a single indent. This can be used to probe compositional changes with depth or to inform on events occurring during loading. Additionally, because strain continuously increases with depth in a spherical indentation test, the Field and Swain analysis can be used to extract an indentation stress-strain relationship.

The approach and assumptions of Field and Swain are similar to those of Oliver and Pharr: a flat elastic half-space deformed by a rigid indenter, and purely elastic unloading. The focus on spherical geometry allows a more detailed quantitative description of the deformation sequence, particularly the transition from solely elastic deformation to elastic-plastic deformation (i.e. permanent deformation). Using Field and Swain's analysis, a simulated force-displacement curve can be generated for a complete loading-unloading cycle, using the known elastic and plastic parameters of a material.

It was shown by Francis [46] that the onset of plastic deformation under a spherical indenter is governed by the ratio p_m/Y, where p_m is the mean pressure over the contact area of the indenter, and Y is the yield strength of the material in simple compression or tension. The contact pressure during elastic loading is given by: [47]

$$p_m = \frac{(16/9)^{2/3}}{\pi} \left(\frac{E_{eff}}{R}\right)^{2/3} P^{1/3} \tag{2.7}$$

where P is the load, R is the radius of the indenter, and E_{eff} is the effective modulus as defined in Eq. 2.6. Whilst $p_m < 1.1Y$, loading is purely elastic. At $p_m/Y = 1.1$, plastic yielding initiates in a localised region beneath the centre of the contact area. As p_m/Y increases, this plasticised region grows, but for $p_m < 3.0Y$ it is fully enclosed

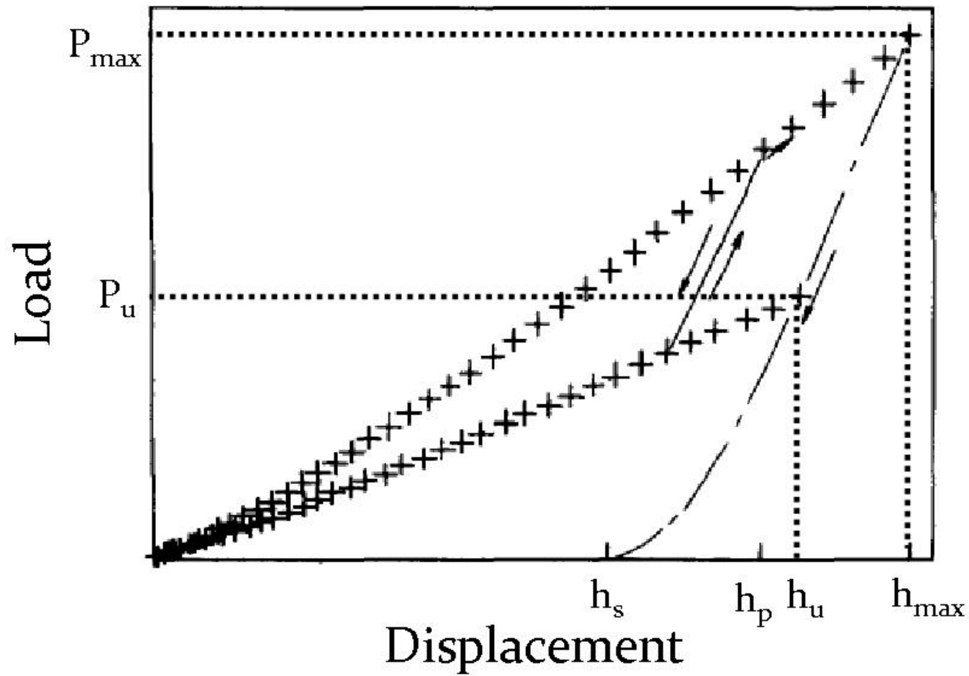

Figure 2.5: Schematic of PL test force-displacement data, showing parameters in the Field and Swain analysis. (Adapted from Ref. [45])

by elastically strained material. Field and Swain make the assumption that this limited plasticity has little measurable effect, and the displacements and stresses are still described in this range by the elastic solution.

At $p_m/Y = 3.0$, the zone of plastically yielded material is large enough to exceed the contact area of the indenter and meet the free surface, and full plastic flow is initiated. Beyond this point, the plastic zone can grow to accommodate the indenter and a constant value of $p_m = 3.0Y$ is maintained. This assumes that no work hardening takes place.

From Eq. 2.7, a critical load P_c for the onset of full plastic flow can be obtained:

$$P_c = (9/16)(R/E_{eff})^2(3\pi Y)^3 \tag{2.8}$$

Hardness and modulus values can be obtained from unloading data as shown in Fig. 2.5 by calculating the residual impression depth, h_s, according to the formula:

$$h_s = \frac{h_u(P_{max}/P_u)^{2/3} - h_{max}}{(P_{max}/P_u)^{2/3} - 1} \tag{2.9}$$

where P_u and h_u are the load and depth after partial unloading. After calculating the 'plastic component' of the penetration depth h_p:

$$h_p = \frac{h_{max} + h_s}{2} \tag{2.10}$$

the radius a of the circle of contact can be calculated according to the relation:

$$a = \sqrt{2Rh_p - h_p^2} \tag{2.11}$$

The hardness and elastic modulus can then be obtained from the relations:

$$H = P/A = \frac{P}{\pi a^2} \tag{2.12}$$

$$E_{eff} = \frac{3}{4}\frac{P}{a\delta} \tag{2.13}$$

where $\delta = h_{max} - h_s$ is the 'elastic component' of the penetration depth.

2.1.4 Indentation fracture

The initial response of a material under indentation with a sharp tip is elastic and plastic deformation. Above some critical load, tensile fracture will also occur. This is often seen as an undesirable circumstance in indentation testing, as fracture tends to increase the compliance of the system and spuriously affect the measured property values. On the other hand, indentation fracture is of considerable interest in its own right, as a model for the formation of strength-diminishing flaws and as a means of determining the fracture properties of materials. This section will describe the main crack types observed during indentation and means of analysing them.

Indentation crack types

Fig. 2.6 illustrates the main types of cracking that occur during indentation. The first, cone cracking, was originally described by Hertz in the 19th century. [48] It occurs under blunt spherical indenters, with radii in the mms or greater. Hertzian cone cracking is not preceded by plastic deformation, and thus can be described simply by the elastically-induced stress state in the material.

The remaining modes of indentation fracture occur when plastic deformation has taken place. In this case the presence of the zone of plastically deformed material has a pronounced effect on the stress state in the vicinity of the indent, and must be taken into account. All these crack modes occur for both pyramidal and (small radius) spherical indenters. Two common modes are radial and median cracking; in both these cases the

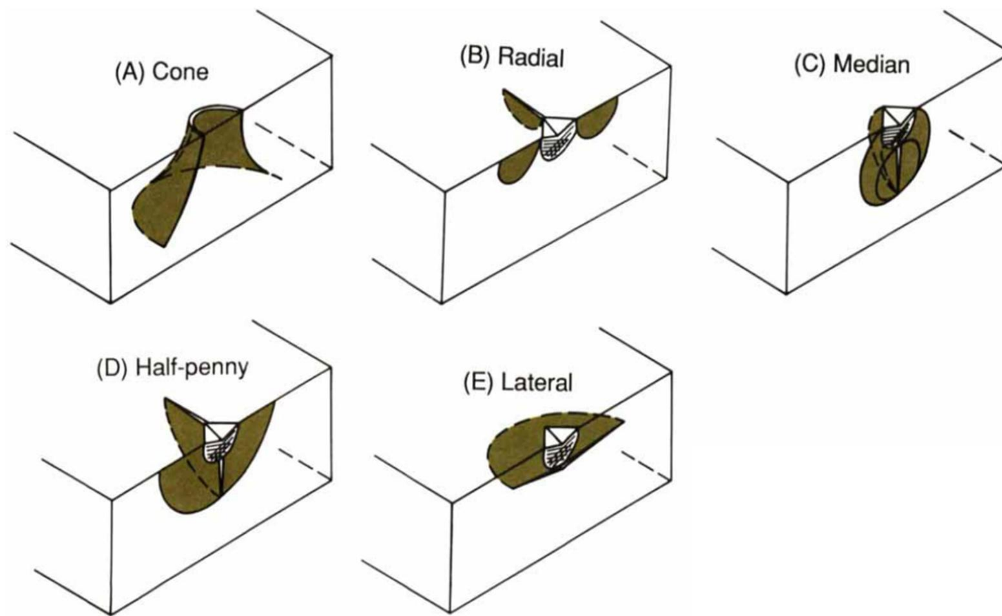

Figure 2.6: Schematics of the main modes of cracking during indentation: (A) Hertzian cone cracking, (B) radial cracking, (C) median cracking, (D) full half-penny cracking, and (E) lateral cracking. (Taken from Ref. [49])

crack plane is orthogonal to the surface. Radial cracks are half-penny type cracks initiated at the edges of the contact impression (Fig. 2.6(b)); median cracks are full-penny cracks which initiate at the base of the plastic zone, but may grow to reach the full surface (Fig. 2.6(c)). The actual sequence of cracking seems to vary by material, [49] but median cracking is more likely to develop during the loading part of the cycle, whilst radial cracking is more likely to develop during the unloading part. The final crack configuration is often a half-penny encompassing the entire indent (Fig. 2.6(d)), which may be a result of the growth of either the radial or median crack types, or a coalescence of both types.

Finally, lateral cracks are cracks running parallel to the surface, initiated at the base or at the edge of the plastic zone (Fig. 2.6(e)). This type of cracking is favoured on unloading, but may initiate during the loading cycle at sufficiently high maximum loads. [49] Lateral cracks typically initiate after other types of crack have already formed.

Indentation fracture theory

The mechanics of fracture at sharp contacts was extensively studied in the 1970s and 1980s by Lawn and co-workers. [50–56] The key to their approach was the recognition that the complex elastic-plastic stress field could be resolved into two components: a reversible elastic component due to the applied force of the indenter; and an irreversible residual component due to the region of plastically strained material. [50, 54] This frame-

work allows analytical expressions to be derived for parameters such as crack length and crack initiation threshold to be derived as a function of applied load, indenter geometry, and material properties.

For well-developed radial/median cracks, the crack length c can be found as: [48]

$$c^{3/2} = \xi \frac{E^{1/2}}{H^{1/2} T_0} P \tag{2.14}$$

where E and H are the Young's modulus and hardness, T_0 is the fracture toughness, ξ is a dimensionless constant, and P is the applied load. Since radial crack length can be readily measured, this offers a means of determining the fracture toughness of a specimen from an indentation test. [55] This has the advantage over other fracture testing methods of being very simple and requiring little to no specimen preparation.

Critical thresholds for initiation of cracking can be obtained by examining the stresses imposed on a crack in the vicinity of an indent. [51, 53] Lawn and Evans argued [51] that the peak stress of the sharp-indenter field must be proportional to the hardness, and thus be approximately constant; however, the spatial extent of the stress field will be proportional to the characteristic contact dimension, and will therefore scale with the size of the indent. Thus, the total resolved stress on a crack near the indent will increase as the applied load is increased. This gives rise to a minimum load P_* and minimum crack size c_* for a stable crack configuration: [53]

$$P_* = \lambda_0 T_0 (T_0/H)^3 \tag{2.15}$$

$$c_* = \mu_0 (T_0/H)^2 \tag{2.16}$$

where λ_0 and μ_0 are geometrical constants. Because it determines the threshold load above which cracking can occur, Lawn and Marshall proposed the ratio H/T_0 as a simple index of a material's intrinsic brittleness. [53] Materials with a higher H/T_0 ratio are generally more prone to fracture during contact events, and will tend to undergo fracture at lower loads during indentation. The implications of this are explored in Chapter 7.

2.2 Ion implantation

Ion implantation is the process of bombarding a specimen with high energy ions, usually at a fixed energy, in order to change its composition and structure. It is widely used in the semiconductor industry as the preferred method for high-precision incorporation of dopants into devices. There is a large amount of research into the fundamental processes

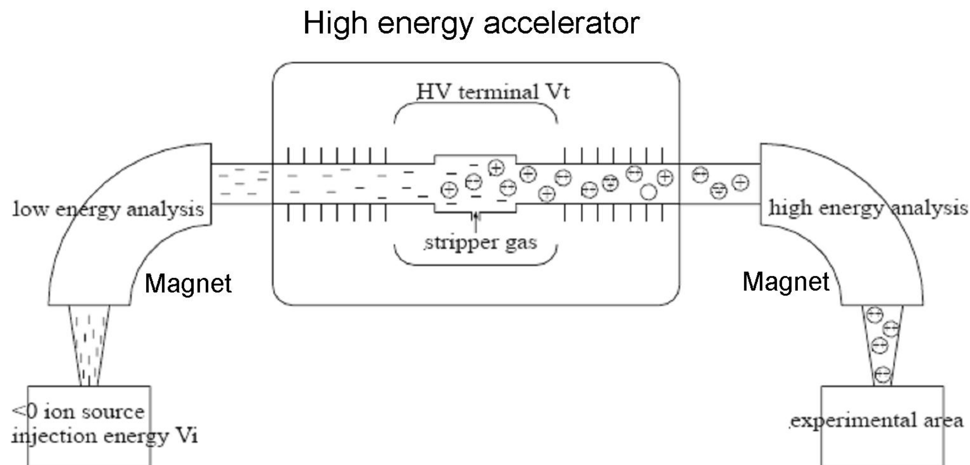

Figure 2.7: Schematic showing the key features of the tandem accelerator. (Taken from [57])

of ion implantation and the modifications to the structure and properties of the implanted material. In this study, ion implantation was used to structurally modify the surface of Ge. This allowed study of the resulting changes to the mechanical properties of Ge.

2.2.1 High-energy ion implantation

High-energy ion implantation was carried in this study using the 1.7 MV NEC tandem accelerator at the ANU. The operation of this instrument will be briefly described.

At the ion source, shown in Fig. 2.7, cesium gas is used to sputter negative ions from a cathode. A wide variety of ion species can be implanted, simply by varying the cathode source material. The ions are accelerated away from the source at ∼100 keV. After leaving the source, the ions pass through an analysing magnet, which selects for the desired ionic species. The ion beam then passes through the high-energy accelerator. The central terminal of the accelerator is held at a high voltage V_t. In the ANU accelerator, this voltage is attained with a Pelletron system, which uses a chain of metal pellets linked by nylon connectors to transport charge. The negative ions are accelerated towards the central terminal. At the terminal, a small quantity of gas is introduced. The gas strips away electrons from some of the negative ions. The resulting positive ions are then accelerated away from the terminal. The ions thus gain a total energy of $2 \times q \times V_t$.

Another analysing magnet is used to select for the desired energy and charge species. Finally, the ion beam reaches the sample chamber, where it is raster-scanned to achieve a uniform implantation in the specimen over a selected area.

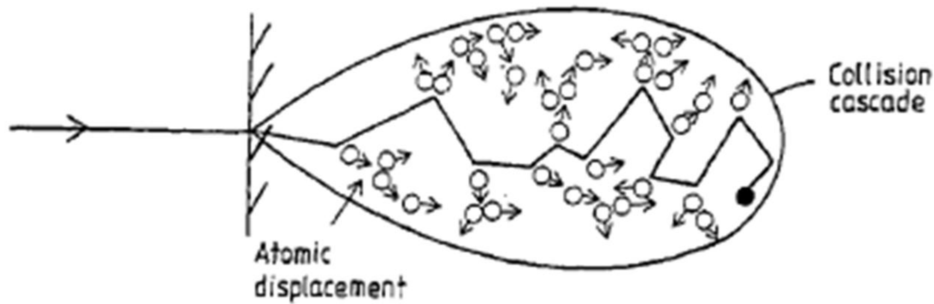

Figure 2.8: An energetic ion entering a sample will trigger a displacement cascade. (Taken from Ref. [58])

2.2.2 Theory of ion implantation

When a high energy ion enters a solid, it will lose energy via a variety of collisional processes until it finally comes to rest within the sample. [58] These collisional processes can be divided into nuclear and electronic proceses. Nuclear processes involve collisions of the ion with nuclei in the target solid. This often displaces the target nucleus from its lattice position. A single heavy energetic ion can cause hundreds of such displacements, resulting in a damage cascade as depicted in Fig. 2.8. Electronic processes involve interactions of the ion with the lattice electrons. These processes may cause lattice damage through heating and may generate radiation such as x-rays and Auger or secondary electrons. The impacting ion will come to rest in the solid after it has lost all its energy.

The immediate effect of an ion displacement cascade is to generate vacancies and interstitials in the crystal. At higher temperatures, dynamical effects during implantation can occur, including recombination of vacancies and interstitials, or agglomeration of point defects to form extended defect clusters. [59] Above some threshold ion fluence, the crystal structure will collapse to form a completely amorphous structure. [60, 61]

Key variables in ion implantation are the distributions of deposited energy, displaced atoms, and vacancies produced, which are dependent on the ion energy, ion species, and composition of the target. These distributions can be approximately obtained analytically, but highly accurate distributions must be obtained by numerical Monte Carlo methods. A freely available software package, SRIM (standing for Stopping and Range of Ions in Matter, J. F. Ziegler, www.srim.org), can perform these numerical simulations and was used in this study to simulate implanted damage.

Ions incident on crystalline materials along a low-index crystallographic axis will experience channelling effects, resulting in an increased and less easily predicted range. To avoid these effects, implants were carried out at an incidence angle of 7° to the specimen

surface (usually the {100} plane).

2.3 Raman microspectroscopy

Raman spectroscopy is a vibrational spectroscopic technique that makes use of the 'Raman effect' discovered by Chandrasekhara Venkata Raman. [62] When light is scattered in a solid, most photons are elastically scattered, referred to as Rayleigh scattering. A small fraction, however, are inelastically scattered, exchanging energy with phonon modes in the solid. The Raman-scattered photons may either lose energy to a vibrational mode, referred to as Stokes scattering, or absorb energy from a vibrational mode, referred to as anti-Stokes scattering. [63]

Raman spectroscopy consists of shining monochromatic light, generally from a laser source, onto a specimen and measuring the energy shift of the resultant inelastically scattered light. [63] In Raman microspectroscopy, a microscope objective is used to focus the incident light on a very small spot, giving spatially dependent information with a resolution of $\sim 1\ \mu m^2$. For crystalline solids, the observed Raman modes are governed by selection rules due to the lattice symmetry. The Raman spectrum (intensity of scattered light as a function of the energy shift) of a crystal is thus characteristic of the crystal structure, usually consisting of one or more sharply defined bands. For amorphous solids, there is no symmetry and no selection rules, and the Raman spectrum is simply the phonon density of states of the material, and usually consists of several broader bands with a Gaussian profile. Raman microspectroscopy can thus be used to determine the structural phase of a material at a precise location (such as an indent). Vibrational modes are sensitive to elastic strain, so Raman spectroscopy can also be used to measure stresses in the material. Representative Raman spectra from different structural phases of Ge are shown in Fig. 2.9.

The advantages of Raman microspectroscopy as a characterisation technique in comparison to TEM analysis is that no sample preparation is required and measurements relatively rapid, spectra typically taking on the order of a minute to collect.

In this study, Raman microspectroscopy was carried out using either a Dilor Super LabRam or a Renishaw 2000 instrument. In both cases, a helium-neon exciting laser (λ = 632.8 nm) was used, with a spot size of $\sim$ 1-2 μm. As Ge metastable phases were found to be sensitive to laser-induced annealing at higher intensities, the laser power was kept below 100 μW.

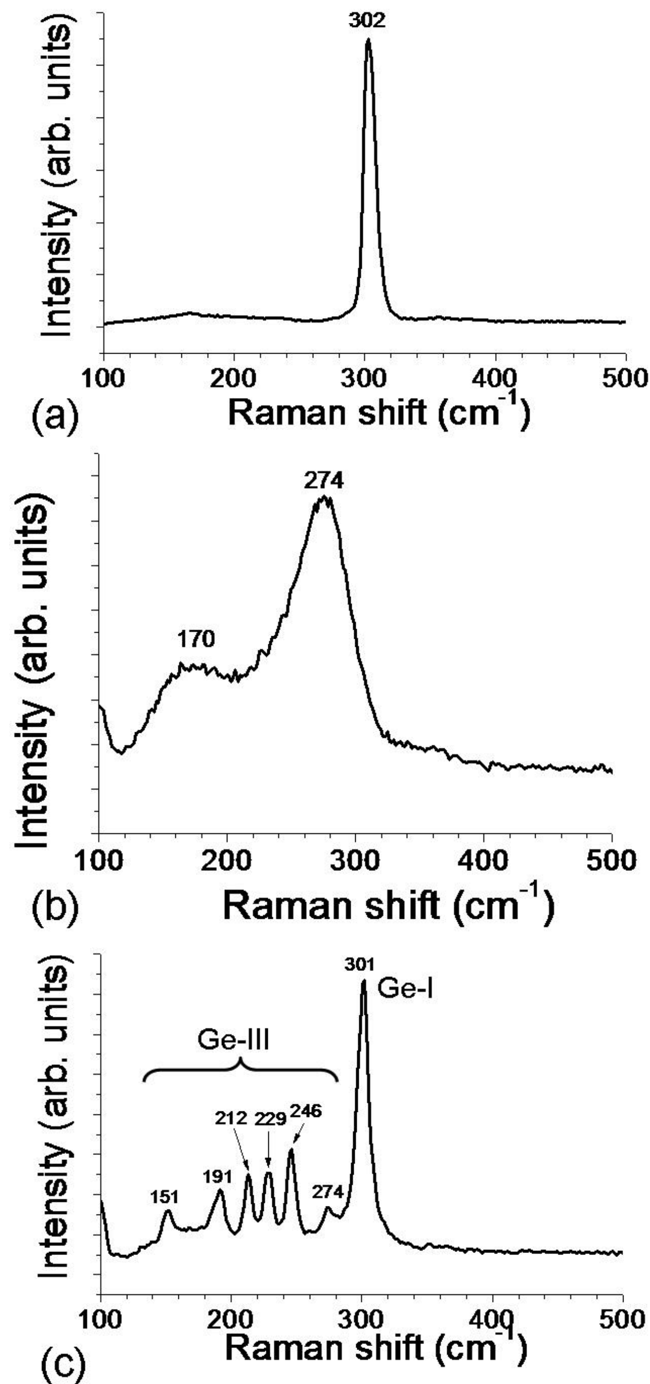

Figure 2.9: (a) Raman spectrum of diamond cubic structure Ge (Ge-I). (b) Raman spectrum of amorphous Ge. (c) Raman spectrum of st-12 structure Ge (Ge-III).

2.3.1 Raman penetration depth

The surface sensitivity of the Raman technique depends on how strongly the incident laser light is absorbed by the sample. The total amount of light scattered by Raman processes between the surface of the sample and a depth d is given by: [64]

$$I_s = I_0\mathrm{D}\int_0^d e^{-2\alpha x}\mathrm{d}x = \frac{I_0 D}{2\alpha}(1 - e^{-2\alpha d}) \tag{2.17}$$

where I_0 is the incident light intensity, D is the Raman scattering cross section, and α is the photoabsorption coefficient of the material at the incident wavelength. Similarly, the amount of light scattered below that depth is given by:

$$I_d = I_0\mathrm{D}\int_d^\infty e^{-2\alpha x}\mathrm{d}x = \frac{I_0 D}{2\alpha}e^{-2\alpha d} \tag{2.18}$$

The penetration depth d_p of the Raman laser can be defined as at which 90% of the signal is attenuated, or

$$\frac{I_d}{I_s + I_d} = 0.1 \tag{2.19}$$

Eqs. 2.17, 2.18, and 2.19 combine to give the following formula for d_p:

$$d_p = \frac{-\ln(0.1)}{2\alpha} \simeq \frac{1.15}{\alpha} \tag{2.20}$$

For Ge, the absorption coefficient at $\lambda = 632.8$ nm is approximately 1.4×10^5 cm^{-1}, so that the penetration depth is $\sim$80 nm.

2.4 Scanning electron microscopy

SEM is an electron microscopy technique in which an energetic beam of electrons is raster-scanned over a specimen, and the resulting intensity of collected electrons or other forms of radiation is measured at each point in the scan and converted into an image. The principle was first demonstrated by Max Knoll in 1935, but SEMs did not become commercially available until the 1960s. [65] SEM provides topographical information similar to optical microscopy, and may also provide compositional, crystallographic, and other information depending on the exact method used. The primary advantages of SEM over optical microscopy are a much higher resolution (as fine as 1-5 nm) due to the short wavelength of electrons, and a very large depth of field.

The two main methods used to generate an SEM image are secondary electron detection, and back-scattered electron (BSE) detection. The first method collects low-energy ‘secondary electrons’ generated by near-surface interactions of the electron beam with the

specimen. This method usually gives good topographical contrast. The second method is to collect electrons that are elastically backscattered along the path of the incident electron beam. This method allows crystallographic and chemical compositional contrast to be obtained.

SEM was used in this study to examine the morphology of indents and the fracture patterns around indents. A Hitachi S4500 field-emission SEM (FESEM) operating in secondary electron mode was used. SEM images were also obtained with the dual-beam FIB as described below.

2.5 Transmission electron microscopy

In a transmission electron microscope, a high-energy of beam of electrons is focussed onto a thin (electron transparent) sample. The transmitted electron beam is used to form an image. TEM offers exceptionally high resolution and the ability to visualise alterations to the crystal structure including dislocations, twin bands, and transformed phases. [66] The disadvantages of TEM include the laborious sample preparation required to obtain electron transparent specimens for viewing and the potential for changes in the material as a result of the thinning process.

The main imaging mode in TEM is Bright field (BF) mode, in which the central transmitted electron beam is used to form the image, and all electrons diffracted by the sample are excluded. This mode gives strong contrast to crystal defects and also reveals areas of phase-transformed material. An alternative imaging mode is Dark field (DF), in which the image is formed from one of the diffracted beams. This mode strongly illuminates the features in the sample responsible for the selected diffraction spot, such as transformed phase regions or twin bands. The generated diffraction pattern can also be studied. The diffraction pattern gives information on the crystal structure, including whether it is single-crystal or polycrystalline, whether there are additional phases, and whether there is amorphous material present. By inserting an aperture at an image plane, the diffraction pattern corresponding to a small area of the specimen can be obtained. This is called a selected area diffraction pattern (SADP).

The instrument used in this study was a Philips CM 300. Electron-transparent cross-sections of indents were prepared using a FIB system, which will be described in the next section.

2.6 Focussed ion beam system

The operating principles of a FIB system are similar to those of the SEM described above. Instead of a beam of electrons, a beam of energetic gallium (Ga^+) ions is raster scanned over a sample region. The secondary electrons generated in the process can be used for image formation in much the same manner as with an SEM. Unlike an SEM, however, the Ga^+ ions have sufficient mass and momentum to ablate material under the ion beam. Because the area under the Ga^+ ion beam can be precisely specified, the FIB has become a powerful and flexible tool for milling small-scale structures for a variety of purposes. An instrument with an ion beam column only is referred to as a single-beam FIB; many instruments now combine an ion beam with a SEM electron beam, and these are referred to as dual-beam FIBs. In this study both a single and dual-beam FIB were used to create cross-sections for both TEM and SEM examination.

The steps for TEM cross-section production are as follows. Protection of the region of interest (ROI) must be considered, since even imaging of the sample at low ion currents will produce a thin amorphised layer in semiconductor materials. To protect the sample, a thin ($\sim$ 100-200 nm) layer of gold may be deposited by thermal evaporation or some other method before the sample is inserted into the FIB. This step is important when a thin surface layer is to be investigated and FIB damage must be avoided.

Once the specimen is inserted into the FIB, the ROI must be located. In a dual-beam FIB, it is found using the electron beam; in a single-beam FIB, by imaging with the ion beam at low beam currents ($>$0.1 nA). Before any milling is done, a layer of Pt is usually deposited over the area where the cross-section is to be. This is done by injecting a Pt-containing organic compound gas near the sample surface and scanning the ion beam over the area to be coated. The ion beam decomposes the gas to form a Pt layer.

There are two main methods of TEM cross-section production in the FIB: the H-bar method, and the pluck-out method. In the H-bar method, the specimen is pre-thinned by mechanical polishing to 30-50 μm thickness. The FIB is then used to thin the ROI to electron transparency (generally $\sim$ 100 nm or less), resulting in an H-geometry (Fig. 2.10(a)) that gives the method its name. In the pluck-out method, the cross-section is milled out in the centre of a trench (Fig. 2.10(b)). The cross-section is then plucked free using a micromanipulator and glass needle (*ex situ*, in this study) and placed on a carbon-coated grid for TEM examination. The pluck-out method offers the advantages of reduced specimen preparation and less milling time.

In both cases, after Pt deposition, rough large-area milling is done at high beam currents ($>$1 nA). The cross-section is then thinned from both sides at progressively lower beam currents. Each step down in beam current decreases the ablation rate but produces a

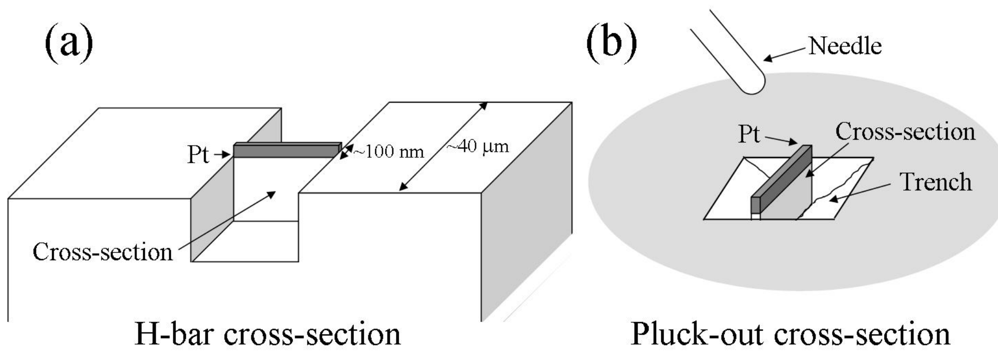

Figure 2.10: Schematics of FIB-milled TEM cross-sections: (a) H-bar cross-section, (b) cross-section for pluck-out.

more tightly focussed beam and a smoother cross-section. The final milling step is usually done at a beam current of 0.1 nA.

The dual-beam FIB was also used to prepare cross-sections to view sub-surface indentation cracking using SEM. In this case, as electron transparency is not a requirement, only one cross-sectional face needs to be milled. The method is similar: Pt is deposited to protect the location of the cross-section; rough milling is used to make a trench for viewing; and finer mills are used to clean the face of the cross-section. The cross-section can be viewed *in situ* with the electron beam. The geometry is illustrated in Fig. 2.11.

Two FIBs were used in this study: a single-beam FEI xP 200, and a dual-beam FEI xT Nova NanoLab 200. Cross-sections milled with the single-beam instrument were made by the H-bar method; cross-sections made with the dual-beam were prepared by the pluck-out method.

2.7 Atomic Force Microscopy

AFM is a scanning probe technique in which a sharp tip attached the end of a cantilever is scanned across a surface. The deflection of the cantilever is measured by a reflected laser spot as the tip is scanned, allowing a topographical image of the surface with nm resolution in the vertical direction to be obtained. A piezoelectric tube allows very precise movement of the tip relative to the sample in the horizontal plane. AFM was invented by Binnig and Rohrer in the 1980s as an extension of scanning tunneling microscopy allowing non-conducting samples to be imaged. [67]

AFM was used in this study as a complementary technique to SEM to examine morphology of indents. AFM was found to give a good quantitative representation of aspects such as indent shape and extruded material around indents, but poor resolution of fracture

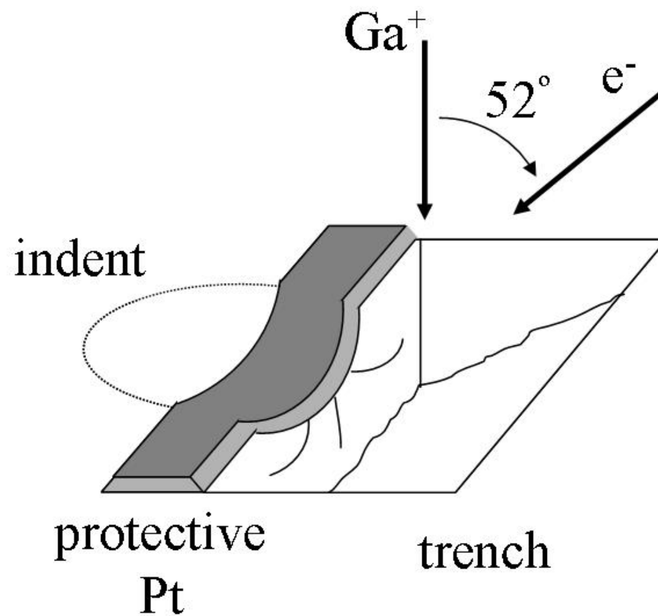

Figure 2.11: Schematic of FIB-milled cross-section for viewing with the SEM column.

features in the vicinity of indents. This is because the radius of the probe tip is large relative to the width of the cracks.

Two AFMs were used: a Digital Instruments Multimode SPM, and a Quesant AFM installed as an attachment to the Hysitron Triboindenter. In both cases imaging was conducted in contact mode, using silicon nitride cantilevers.

2.8 Positron Annihilation Spectroscopy

Positron annihilation spectroscopy (PAS) is a technique used to analyse defects and defect complexes in solids. [68, 69] The technique involves a low-energy positron beam interacting with the specimen of interest, producing energetic photons by the annihilation of positrons with electrons in the material. Analysis of the γ-ray photons produced provides information on the local environment 'seen' by the positron and electron, and thereby on the structure of the material. PAS is useful in characterising small open-volume defects in materials.

In this study, a monoenergetic positron beam was used to carry out depth-resolved Doppler broadening positron measurements. When a γ-ray photon is produced by positron-electron annihilation, it will be Doppler shifted due mainly to the momentum of the electron. When a number of photons are collected in an experiment, the recorded energy peak

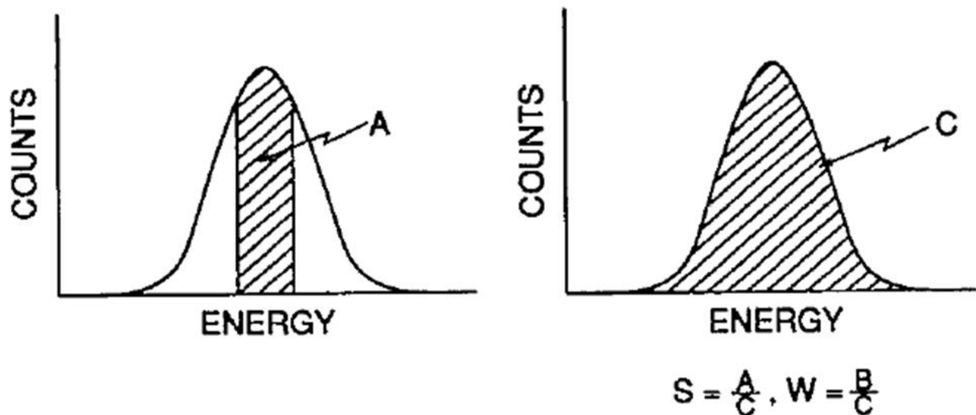

Figure 2.12: Definition of S-parameter for a Doppler-broadened PAS spectrum, $S = A/C$. (Adapted from Ref. [69].)

will be broadened due to this process, which is referred to as Doppler broadening. The degree of broadening is related to the electron momentum distribution and hence to the number and type of defects in the material. [69] A convenient means of quantifying the degree of broadening for a given peak is by determining the 'S-parameter', defined as the ratio of the central area under the peak to the total area, as illustrated in Fig. 2.12. Because the central area can be chosen arbitrarily, the quantity of physical relevance is the relative value of the S-parameter compared to the S-parameter of pristine material. Greater S-parameter values relative to pristine material often indicate the presence of open volume defects. [70] The S-parameter is proportional to both defect density and individual defect volume. To obtain a depth-sensitive measurement, the S-parameter is determined for a range of incident positron energies, as the incident energy determines the average penetration distance of the positron into the sample.

PAS for this study was carried out at the University of Western Ontario by Prof. Peter Simpson.

CHAPTER 3

Rate-dependent indentation behaviour of Ge

3.1 Introduction

The nature of the indentation response of Ge has attracted some controversy. There are conflicting reports as to whether it undergoes a pressure-induced phase transformation during indentation. Several studies of Ge using high-load Vickers microindentation have observed evidence of a metallic phase transformation. [17,19,26] Other studies employing low-load nanoindentation, however, have failed to find evidence of a high-pressure phase transformation in crystalline Ge. [27,30,31] These previous studies are described in detail in Chapter 1.

The inconsistency between these two sets of studies presumably stems from the the difference in loading conditions between conventional microindentation and instrumented nanoindentation systems. Apart from the maximum applied load, the most important such difference is the rate of loading. In a nanoindentation test this is typically 0.1 to 10 mN·s^{-1}. For a microindenter the loading rate is orders of magnitude faster, typically 10 to 10^4 mN·s^{-1} depending on the instrument. [71] In a previous study by Jang *et al.*, Ge was indented at loading rates of 0.5 and 5 mN·s^{-1}. [31] Phase transformations were observed for the faster loading rate, but only reproducibly for a sharp cube-corner indenter, not for the more common Berkovich or spherical indenter geometries.

For this study, the deformation mechanism of Ge was investigated over 3 orders of magnitude variation in loading rate, from 0.5 to 900 mN·s^{-1}. Rate was found to be a critical parameter. For slow loading rates, shear plasticity predominated. For rates of $\sim$50 mN·s^{-1} and above, pronounced and repeatable phase transformations to metastable crystalline and amorphous phases were observed, for both Berkovich and spherical indenters. These differences are related to the underlying rate sensitivities of the mechanisms involved.

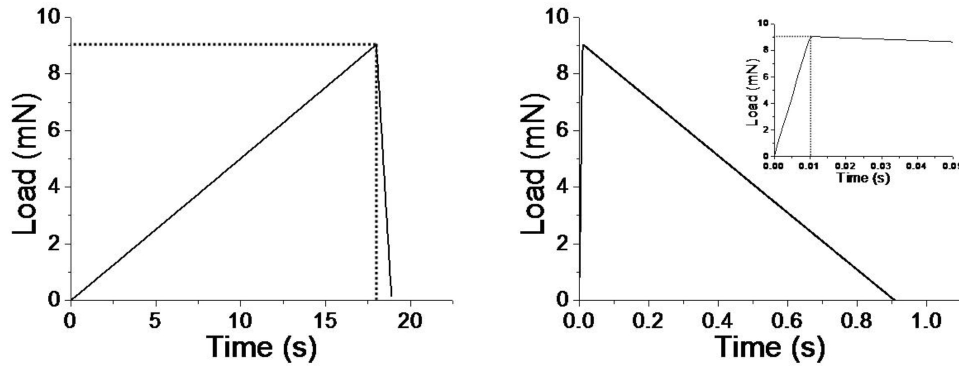

Figure 3.1: Load vs time functions for the Hysitron with (a) a slow loading rate (dP/dh = 0.5 mN·s^{-1} on loading, dP/dh = 10 mN·s^{-1} on unloading), and (b) a fast loading rate (dP/dh = 900 mN·s^{-1} on loading, dP/dh = 10 mN·s^{-1} on unloading).

3.2 Experimental details

Tests were performed with the Hysitron Triboindenter, over a range of loading rates from 0.5 mN·s^{-1} to 900 mN·s^{-1}, roughly the maximum loading rate attainable with that instrument. Typical load functions used are shown in Fig. 3.1. Indents were made to maximum loads of 9 mN, using a Berkovich tip. Tests were conducted in open loop mode.

Performing high loading rate tests with the UMIS indenter was more difficult, since this instrument is normally capable of maximum loading rates of only ~10-20 mN·s^{-1}. In order to obtain higher loading rates, tests were conducted with the UMIS in which the tip was rapidly brought in contact with the sample by manually lowering the indenter carriage. This is equivalent to the 'tip crash' procedure usually used to bring the tip within range of the surface prior to a test. The applied force during the test can still be accurately determined by monitoring the load signal output. Maximum loads and loading rates were determined from the resulting load vs. time trace. In addition, unloading curves were obtained for some of these manual indents, by stepping down from the maximum load in small increments and recording the load and displacement at each step. High loading rate tests were performed with both spherical (R $\approx$ 4.3 μm) and Berkovich tips. Maximum loads were $50 - 100$ mN.

Fig. 3.2 shows typical load vs time plots for high loading rate UMIS indents. Loading rates varied but generally lay in the range $\sim 100 - 200$ mN·s^{-1}. Unloading rates were either 'fast' [Fig. 3.2(a)], when the indenter was unloaded in a single increment, or 'slow' [Fig. 3.2(b)], when the indenter was unloaded in multiple increments.

Tests were also carried out using the normal operating mode of the UMIS up to maximum loading rates of ~15 mN·s^{-1}.

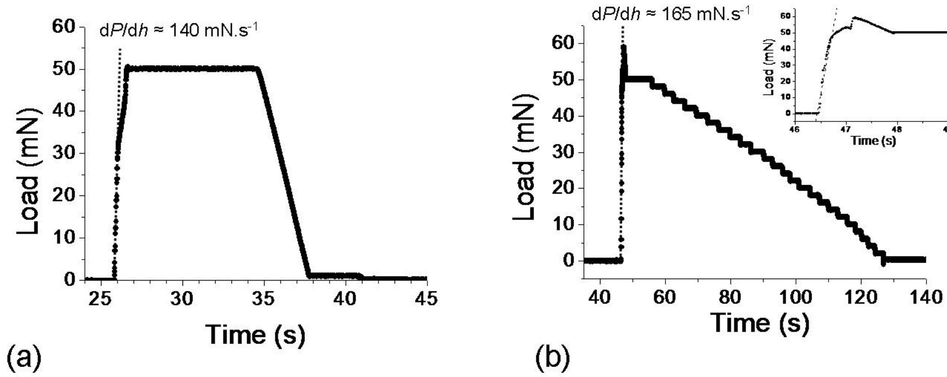

Figure 3.2: Load vs time plots for UMIS high loading rate indents. (a) Test with a rapid unloading rate (dP/dh $\approx$ 140 mN·s^{-1} on loading, dP/dh $\approx$ 15 mN·s^{-1} on unloading), and (b) a slow unloading rate (dP/dh $\approx$ 165 mN·s^{-1} on loading, dP/dh $\approx$ 0.7 mN ·s^{-1} on unloading).

Raman spectra were obtained from indents using the 632.8 nm line of a HeNe laser. Laser powers were kept low to avoid annealing metastable phases (see Chapter 2).

Cross-sections of high loading rate UMIS indents were made using the dual-beam FIB for TEM examination. Indents were gold-coated prior to insertion in the FIB to avoid any damage from the ion beam.

3.3 Results

P-h curves for Hysitron indents made at slow loading rates < 50 mN·s^{-1} in Ge usually showed a classical elastic-plastic unloading response (Fig. 3.3(a)). [42] Indents at faster loading rates showed deviations from this behaviour, notably some creep at maximum load (although no hold period was applied) and elbowing on unloading, as shown in Fig. 3.3(b). Increasing loading rate led to increased creep. Some indents as in Fig. 3.3(c) featured a pop-out event on unloading, a feature that, when observed in Si, is attributed to phase transformation. [22,23] We note that pop-outs were occasionally observed at slower loading rates as well. Pop-out occurrence seemed to be dependent on unloading rate, with pop-outs observed at unloading rates of 10 mN·s^{-1} but not at slower rates. Calculated hardness values, plotted in Fig. 3.3(d), were found to increase with increasing loading rate.

For high loading rate Hysitron indents, the shape of the unloading curve was dependent on the unloading rate. For tests with a slow unloading rate of 1 mN·s^{-1}, elbowing was much less pronounced than for an unloading rate of 10 mN·s^{-1}. Elbowing could also be suppressed for high loading rate indents (dP/dh = 200 mN·s^{-1}) by a hold period of 5

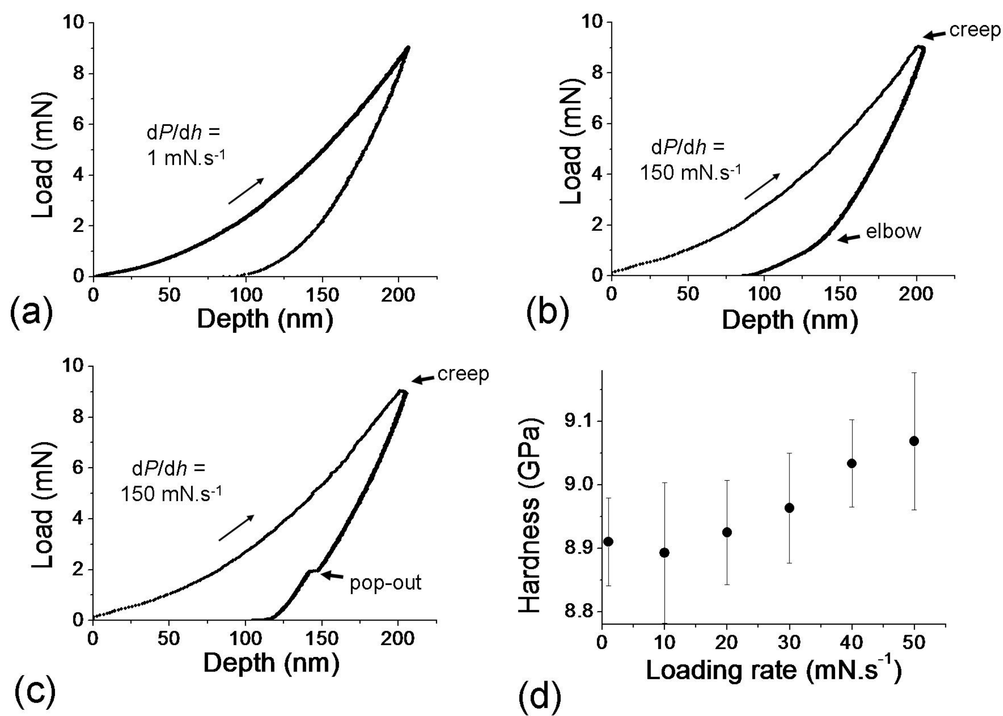

Figure 3.3: P-h curves for Hysitron Berkovich indents to 9 mN at different loading rates: (a) loading rate of 1 mN·s^{-1}, (b) loading rate of 150 mN·s^{-1}, with elbow, (c) loading rate of 150 mN·s^{-1}, with pop-out. For all curves the unloading rate is 10 m·s^{-1}. (d) Dependence of measured hardness on loading rate.

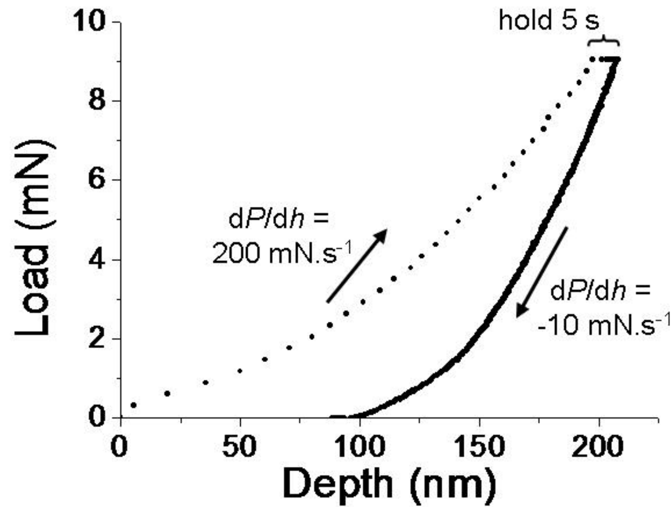

Figure 3.4: P-h curves from a high loading rate indent with the Hysitron with a hold period of 5 s at maximum load.

s at maximum load, shown in Fig. 3.4. Appreciable creep was observed during the hold period, increasing the maximum depth by $\sim$10 nm, compared to that observed for low loading rates.

Indents made using the UMIS with loading rates ranging from 1 mN·s^{-1} to 15 mN·s^{-1} had featureless unloading P-h curves. The Raman spectra taken from these indents showed no additional bands, only the Ge-I band broadened and shifted to higher wavenumbers by compressive stress, as shown in Fig. 3.5(a).

Raman spectra from high loading rate indents featured, in addition to the Ge-I band, a broad spectral component at wavenumbers between $200-300$ cm^{-1}. This spectral component indicates the presence of amorphous Ge. This amorphous component was observed for both fast unloading rates [Fig. 3.6(a)] and slow unloading rates [Fig. 3.5(b)], and for Berkovich indents [Fig. 3.6(b)] as well as spherical indents. Some indents in addition to the amorphous signal featured small multiple sharp bands, indicating the presence of crystalline structural phases in addition to Ge-I. These sharp bands are marked by arrows in Figs. 3.6(a) and 3.5(b). In a couple of cases these additional bands were large enough to be measured [Fig. 3.6(b)]: the positions of the bands indicated that the additional phase is Ge-III.

Indents made with the Hysitron were too small for individual Raman spectra to be collected. Raman spectra were taken with the laser spot focussed on 3$\times$3 arrays of Hysitron indents. These spectra showed slight up-shifting and broadening of the Ge-I peak, but

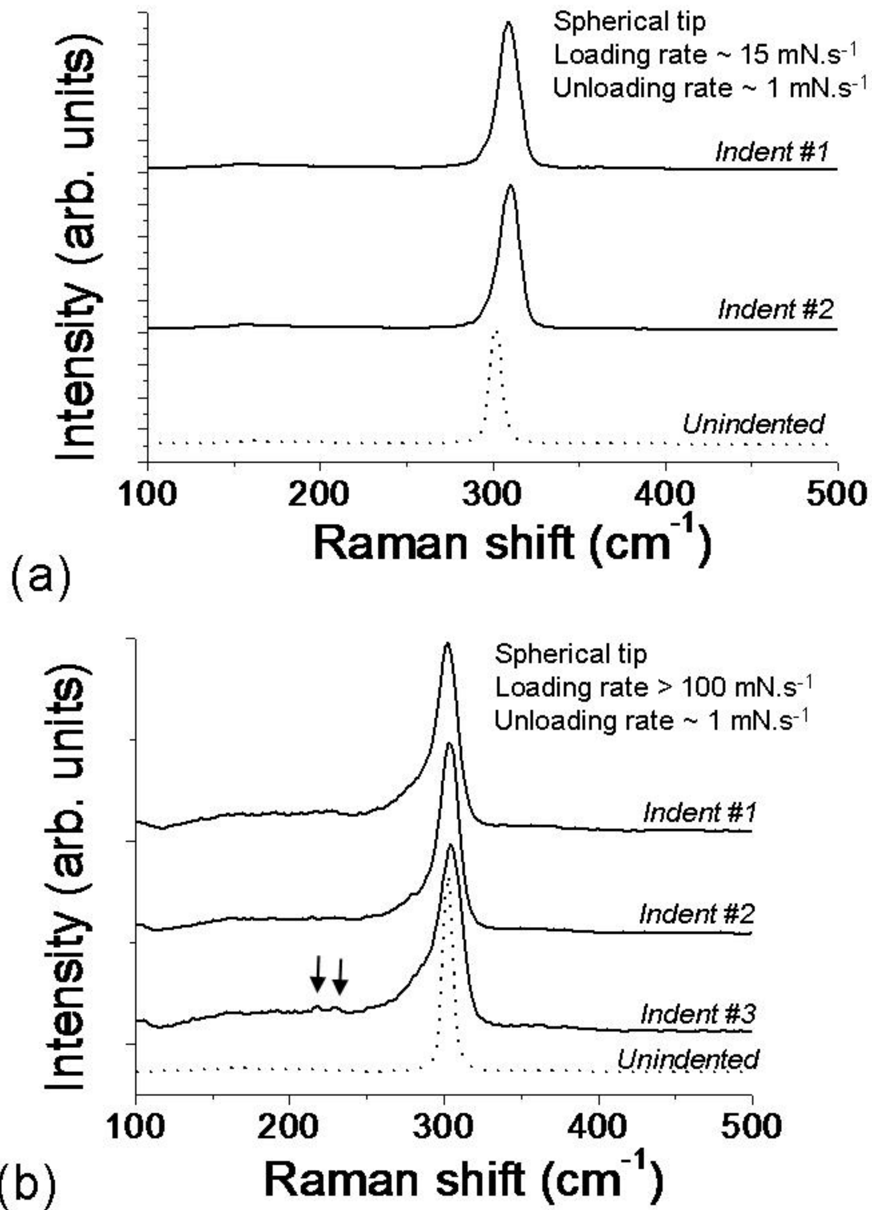

Figure 3.5: Raman spectra from indents made with the UMIS. (a) Spherical tip, $\mathrm{d}P/\mathrm{d}h \approx$ 15 mN·s^{-1} on loading, $\mathrm{d}P/\mathrm{d}h \approx 1$ mN·s^{-1} on unloading. (b) Spherical tip, $\mathrm{d}P/\mathrm{d}h$ 100 mN·s^{-1} on loading, $\mathrm{d}P/\mathrm{d}h \approx 1$ mN·s^{-1} on unloading. For all plots, solid lines are Raman spectra taken from indents (made under the same conditions in each plot), dotted line is the spectrum of pristine Ge.

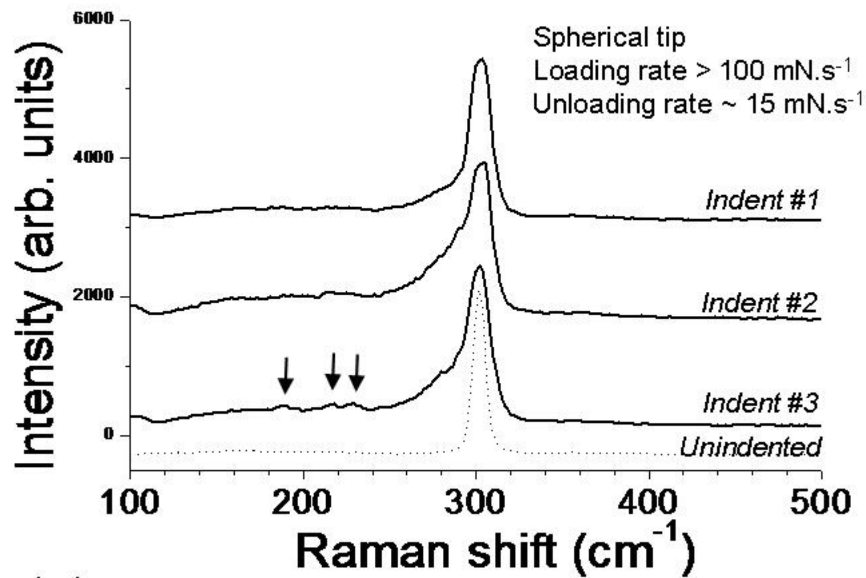

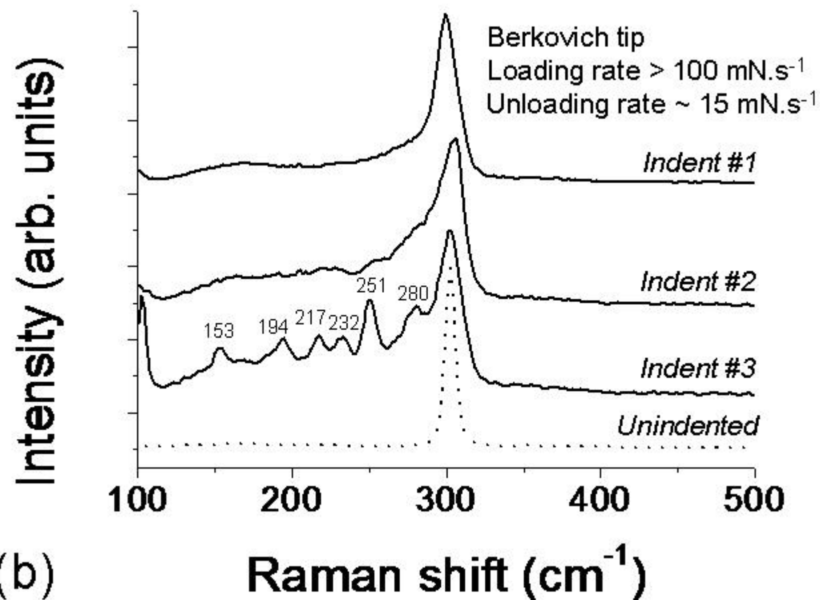

Figure 3.6: Raman spectra from indents made with the UMIS. (a) Spherical tip, dP/dh 100 mN·s^{-1} on loading, dP/d$h \approx$ 15 mN·s^{-1} on unloading. (b) Berkovich tip, dP/dh 100 mN·s^{-1} on loading, dP/d$h \approx$ 15 mN·s^{-1} on unloading. For all plots, solid lines are Raman spectra taken from indents (made under the same conditions in each plot), dotted line is the spectrum of pristine Ge.

were otherwise similar to undamaged Ge. If transformed phases are present within the Hysitron indents, the total volume of them may be too small to produce a detectable Raman signal. XTEM would help to confirm whether transformed material is present, but has not yet been carried out.

Fig. 3.7(a) is a BF XTEM micrograph showing the deformation region of a high loading rate Berkovich indent made using the UMIS. Across the top of the deformation region, just below the surface, there is a phase-transformed zone 200-300 nm deep, distinguished by darker grey contrast compared to the surrounding material. The DP pattern from the transformed zone in Fig. 3.7(b) shows that it contains a-Ge, polycrystalline Ge-I, and another phase marked by additional reflections. The reflection indicated by an arrow has a spacing of 0.45 nm, corresponding to the $\{101\}$ lattice plane of the Ge-III structure. [12] Several SADP were taken at different areas within the transformed zone: the relative intensity of the reflections from different phases varied. This indicates some inhomogeneity within the transformed region, consistent with the non-uniform contrast. Twin bands on $\{111\}$ planes and tangles of dislocations are visible in the damaged region below the phase-transformed zone.

Another high loading rate Berkovich indent is shown in Fig. 3.8. Again a phase-transformed zone is present, $\sim$400-500 nm deep. In this case, SADP from several areas confirmed that the transformed zone contained only a-Ge and polycrystalline Ge-I. Again, twin bands and dislocations are present in the damage region.

TEM of a rapid loading rate indent with the spherical tip is shown in Fig. 3.9. Again, a phase-transformed zone is present beneath the surface. The transformed zone contains a-Ge and a small amount of Ge-III. Extensive lateral and median cracking is also present.

3.4 Discussion

All indents made to high loading rates with the UMIS and examined by Raman showed the presence of a-Ge and/or Ge-III. XTEM confirmed this, showing an inhomogeneous phase-transformed zone, just below the deformed surface, a few hundred nm deep and extending about the width of the damage region. It is highly likely that this transformed zone is the product of a high-pressure phase transition to the Ge-II phase under load, given the presence of Ge-III. This is also consistent with the fact that the zone is found just below the surface, where the hydrostatic stress is highest during an indentation test. Interestingly, the unloading rate had no discernable effect on the final phase in the indent: a-Ge and Ge-III were observed with roughly equal probability for both slow (< 1 mN$\cdot$s^{-1}) and rapid ($\sim$ 15 mN$\cdot$s^{-1}) unloads. This is quite different from the behaviour of the indentation-induced phase transformation in Si, where the final phase is sensitively dependent on the

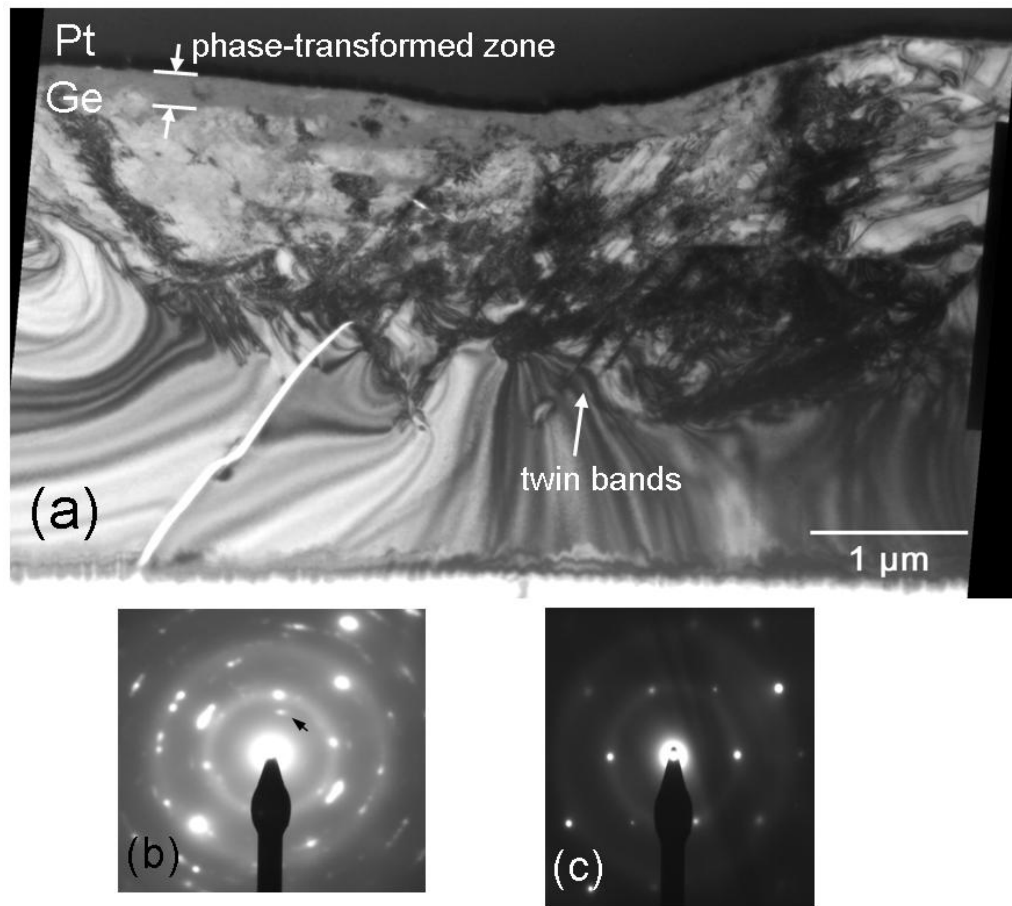

Figure 3.7: XTEM from a high loading rate UMIS Berkovich indent (dP/d$h \approx 60$ mN·s^{-1} on loading, dP/d$h \approx 15$ mN·s^{-1} on unloading). (a) BF micrograph of the whole indent, showing phase transformation and shear damage. (b) SADP from the phase-transformed zone. (c) SADP from pristine material for comparison.

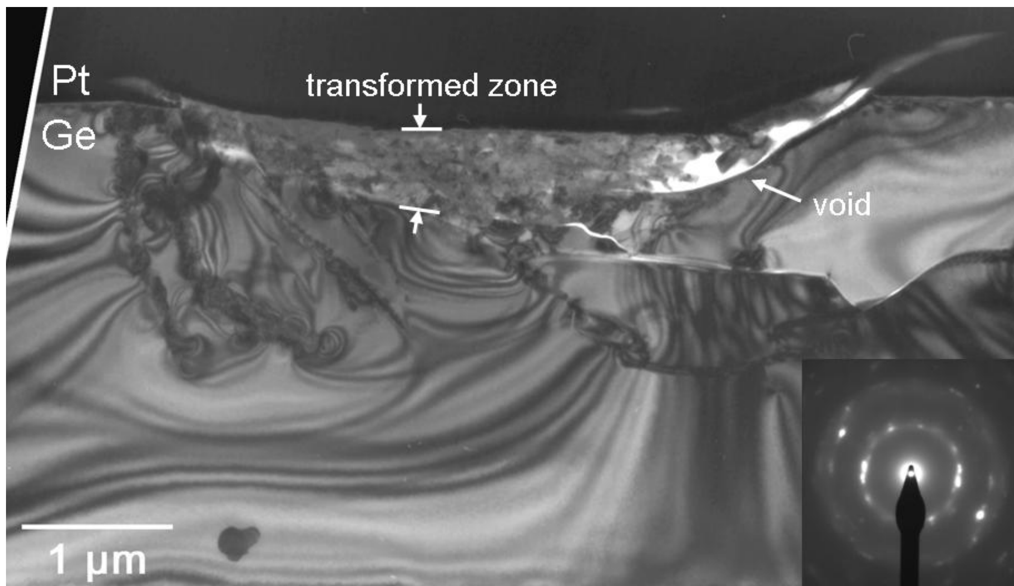

Figure 3.8: BF micrograph of a different rapid loading rate UMIS Berkovich indent ($\mathrm{d}P/\mathrm{d}h \approx 140$ mN·s^{-1} on loading, $\mathrm{d}P/\mathrm{d}h \approx 15$ mN·s^{-1} on unloading). Inset: SADP from the phase-transformed zone.

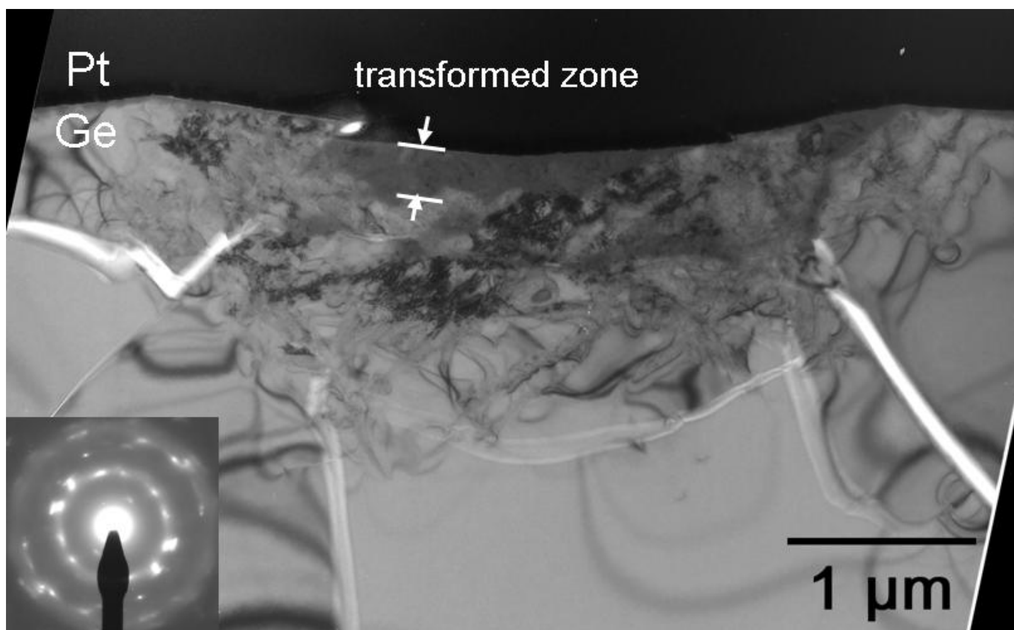

Figure 3.9: BF image of a high loading rate UMIS spherical indent ($\mathrm{d}P/\mathrm{d}h \approx 165$ mN·s^{-1} on loading, $\mathrm{d}P/\mathrm{d}h \approx 1$ mN·s^{-1} on unloading). Inset: SADP from the phase-transformed zone.

unloading rate. [22] One possible explanation is that the phase under load in this case is a highly disordered form of Ge-II that preferentially transforms to (low-density) a-Ge on unloading, regardless of the unloading rate. Rapid loading rate experiments performed on Si could give further evidence for this.

The observations reported here clearly show phase transformations can be induced in Ge using both a Berkovich and spherical indenter. Indeed, unlike previous studies, Ge-III or a-Ge was consistently observed in rapid loading rate indents. The presence of Ge-III strongly indicates that the transformed material derives from a pressure-induced phase transition to metallic Ge-II (β-tin) under load, which transforms to Ge-III or a-Ge upon load release. Thus it appears that loading rate plays a critical role in the mode of deformation. A model to explain this result will now be outlined.

The strain rate sensitivity of the shear yield stress in Ge has been investigated by several groups. [72, 73] The brittle-to-ductile transition in Ge shows a strong positive strain rate dependence, yielding an activation energy for dislocation glide of $\sim$1.54 eV. [74] Plasticity under nanoindentation at room temperature clearly falls into the 'low temperature, high stress' regime, [75] in which twinning is the dominant shear mechanism. According to the model for twinning proposed by Pirouz, [76] stress-induced twinning in diamond-cubic and zincblende semiconductors arises from the differing mobilities of partial dislocations [77] and depends upon thermally-activated cross-slip for twin growth. Twinning can thus be expected to also show a strong dependence on the strain rate: in other words, the critical stress for twinning will increase as loading rate increases. This is consistent with the observed increase in hardness with loading rate [Fig. 3.3(d)], indicating an increasing resistance to shear.

The β-tin phase transformation exhibits quite different rate sensitivity. Shock loading experiments have been carried out on silicon with pressure increase rates greater than 10^7 GPa$\cdot$s^{-1}. [78] The β-tin transition was observed in that experiment at $\sim$11 GPa, not significantly different from the transition pressure of 12.5 GPa observed in diamond-anvil cell (DAC) experiments. [10] In DAC experiments, typical loading rates [79] are <1 GPa$\cdot$min^{-1}. Thus over this enormous rate range, the diamond-cubic $\rightarrow$ β-tin transition appears to be relatively rate-insensitive. On theoretical grounds as well, the diamond-cubic $\rightarrow$ β-tin structural transition can be expected to be relatively rate-insensitive. It has been noted that it has a 'hybrid' character with features of both reconstructive-type and displacive-type phase transformations, [79, 80] and hence bears some similarity to rapid martensitic transitions. For the current study, the stress required to induce the β-tin phase transformation can be expected to be effectively insensitive to loading rate.

If the critical stress for shear plasticity is sensitive to strain rate and the stress for phase transition is rate-insensitive, this suggests that a critical indentation loading rate

exists, at which phase transition will become energetically favourable relative to shear. This is entirely consistent with our experimental observations. Based on those it appears that the critical loading rate is somewhere between 50 and 150 mN·s^{-1} for Berkovich and spherical tip geometries. This can be converted to an absolute strain rate for the spherical tip using the formula $\mathrm{d}\epsilon/\mathrm{d}t = (10R\sqrt{H\pi})^{-1}P^{-1/2}\mathrm{d}P/\mathrm{d}t$, derived from Tabor's definition [39, 81] of 'indentation strain' $\epsilon = 0.2a/R$ and the definition of hardness (Eq. 2.12), and using $H \cong 10.6$ GPa for Ge (see Chapter 4). R is the tip radius, a the contact radius, and P the applied load. Inserting the load rates and maximum loads at which phase transformation was observed into this formula gives a critical strain rate of $0.05 - 0.1$ s^{-1}.

With these results, the discrepancy between studies conducted with high-load conventional microindentation, which have found a phase transformation to occur in Ge, [19,26] and studies conducted with instrumented nanoindentation, which have tended to observe little or no evidence of phase transformation, [27, 30, 31] can be explained. The loading rate in a Vickers microindentation test is variable depending on the instrument, but is generally higher than 10 mN·s^{-1} and may be as high as 10 N·s^{-1}. [71] On the basis of these observations, most Vickers tests would be in a loading rate regime where shear plasticity is rate-limited, and phase transformation is hence favourable.

3.5 Concluding remarks

It has been shown that indents made with loading rates in excess of 50-100 mN·s^{-1}, with both spherical and Berkovich tips, contain a-Ge and metastable Ge-III on unloading. These phases are evidence of a high-pressure metallic phase transformation on unloading. This occurs because shear-induced twinning, the normal mode of deformation in room temperature-indented Ge, is limited by strain rate. The phase transformation itself is rate-insensitive over the range investigated. These observations explain why previous studies on Ge employing conventional microindentation, and hence very rapid loading rates, have found a phase transformation to occur, whilst studies employing nanoindentation, and hence slow loading rates, have not. The ability to induce phase transformation in Ge by indentation opens up similar technological possibilities as have been proposed for Si, [26] given that indentation is a relatively low-cost technique and the transformed phases have novel electrical, [82] mechanical [83] and chemical [84] properties.

Similar indentation rate sensitivity might be expected in other open-structured covalent materials, such as III-V and II-VI semiconductors. Shear-induced twinning and slip are observed under indentation for GaAs and other compound semiconductors, [29,33,34] and shear mechanisms in these materials are rate-limited as in Ge. Above some critical indentation loading rate they should also exhibit high-pressure phase transformation.

CHAPTER 4

Nanoindentation of implanted crystalline Ge

4.1 Introduction

Most nanoindentation studies on crystalline Ge, [27,28,30,31,85] and even on Si and compound semiconductors, [22,23,27,28,33,34] have been carried out on pristine, defect-free single crystals. This raises the question of how the presence of defects in the crystalline structure affects the mechanical response of a covalent material. One means to address this question is to introduce defects into Ge by the technique of ion implantation, whereby a beam of monoenergetic ions is directed at a target specimen. The nature and extent of damage introduced in the specimen by the ion beam is dependent on the ion species, ion energy, fluence of ions, and the temperature at which implantation is carried out, all parameters that can be controlled to a high degree. Ion implantation is an important technique in the semiconductor industry because it is commonly used to introduce electronic dopant impurities. [58] Extensive work has been done on the fundamental processes of ion interactions in solids. [59–61, 69, 86]

It is difficult to predict what effect implantation-induced defects will have on the nanoindentation response of a covalent semiconductor. In most materials the presence of defects impedes slip, raising the mechanical hardness, so called ‘work hardening.’ [87,88] In covalent crystals, hardness has been regarded as an intrinsic material property, [89–91] dependent on bond strength and independent of extrinsic factors such as the defect state. This chapter examines implantation conditions that generate disorder but not complete amorphisation. It is shown that high-fluence implantation-induced defects actually lower the hardness of c-Ge, reflected in both measured properties and a quasi-ductile indent morphology after nanoindentation. A thermal annealing treatment reverses the effect, increasing the hardness of the implanted layer and promoting extensive cracking during indentation. This implies that simple defects (point defects or clusters) formed directly after ion implantation facilitate plasticity in Ge, whereas extended defects formed after thermal annealing hinder plasticity.

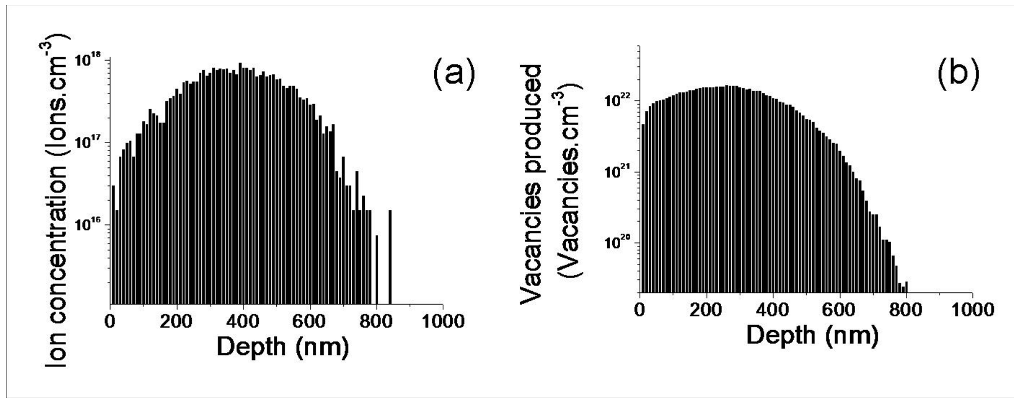

Figure 4.1: TRIM simulation results for 800 keV Ge ions implanted in Ge to 3×10^{13} ions·cm^{-2}. (a) Distribution of implanted ions. (b) Distribution of vacancies generated during implantation.

4.2 Experimental details

Undoped Ge(100) specimens were implanted with Ge ions at an energy of 800 keV. Implants were carried out at room temperature. Specimens were implanted to fluences of 3×10^{12} ions·cm^{-2}, 1×10^{13} ions·cm^{-2}, and 3×10^{13} ions·cm^{-2}. Ion beam fluxes were $\sim$1.5$\times10^{11}$-6$\times10^{11}$ ions·cm^{-2}·s^{-2}. Samples implanted at this energy to doses of 1×10^{14} ions·cm^{-2} and higher were found to have an amorphous layer.

Ion distributions and damage profiles were simulated using SRIM, described in Chapter 2. Results for the range of implanted ions and distribution of generated vacancies are shown in Fig. 4.1. The SRIM simulation yielded a damage production of $\sim$22 000 vacancies/ion.

After implantation, some samples were annealed under flowing argon in a tube furnace for 30 min at a constant temperature of 150 °C, 200 °C, or 300 °C.

Positron annihilation spectroscopy (PAS) was carried out to obtain information on open volume defects generated by implantation. Doppler broadening measurements of the 511-keV annihilation line were taken using a variable-energy positron beam (University of Western Ontario). The line shape 'S' parameter was used to characterise broadening. [69]

Indentation was carried out using the UMIS-2000 indenter with a spherical tip of nominal radius 4.3 μm. Maximum loads of up to 100 mN were used, and loading and unloading rates of dP/dh $\approx$ 1 mN·s^{-1}. Values of hardness and elastic modulus were obtained from tests to 50 mN with the spherical tip analysed by the Oliver and Pharr method. [42]

In some cases, arrays of indents were made in pristine samples. The samples were subsequently ion-implanted according to the method described above. This was done

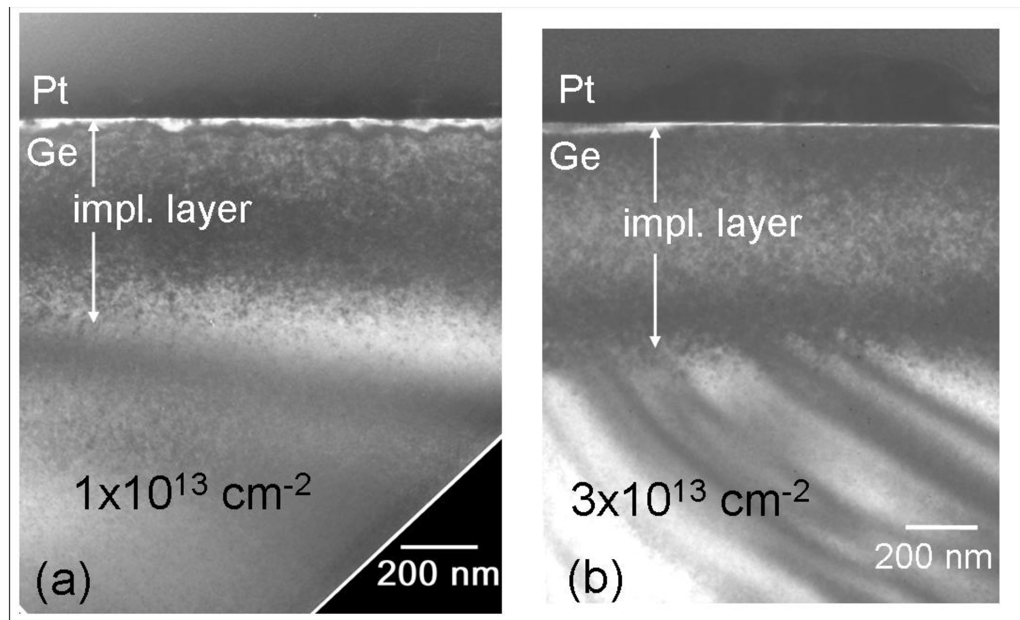

Figure 4.2: XTEM of implanted layers. (a) BF image of 1×10^{13} ions·cm^{-2} dose implanted layer. (b) BF image of 3×10^{13} ions·cm^{-2} dose implanted layer.

to investigate whether the order of sequence affected the type of damage produced by combined indentation and ion implantation.

Atomic force microscopy was carried out using a Quesant AFM in contact mode to examine the morphology of indents in the implanted specimens. Additional AFM was done with a Digital Instruments Nanoscope III SPM, also in contact mode.

Raman spectra were obtained from indents with a Renishaw 2000 Raman microscope, using the 632.8 nm line of a HeNe laser. The laser power was kept low to avoid annealing any metastable phases.

Cross-sections of indents for TEM were prepared using the xT Nova NanoLab 200 dual-beam FIB. TEM specimens were imaged with the Philips CM 300, operating at 300 keV.

4.3 Results

Cross-sectional TEM confirmed the presence of a heavily defective but crystalline surface layer after implantation. Fig. 4.2 shows TEM micrographs of implanted layers. The layer width is ~600 nm, in agreement with the TRIM simulations. For the highest dose 3×10^{13} ions·cm^{-2} sample, there is a lighter-contrast speckled band in the centre of the implanted layer where generated damage is highest. SADPs showed no amorphous rings in any of the implanted layers, apart from the faint amorphous traces caused by FIB preparation.

Fig. 4.3 shows results of PAS from implanted samples, before and after annealing. The Doppler broadening S parameter, which is sensitive to vacancy-type defects, is plotted for each sample against positron energy. Estimated average positron penetration depth $\bar{z}$ is marked on the upper axis, calculated using the empirical formula: $\bar{z} = \frac{4.0\mu\text{g}\cdot\text{cm}^{-3}}{\rho_{\text{Ge}}} E^{1.6}$, where E is positron energy in keV and $\rho_{\text{Ge}} = 5.324$ g·cm^{-3}. [92] The as-implanted samples show the same dose-independent profile in Fig. 4.3(a), indicating saturated positron trapping due to the high concentration of implantation-induced defects. The S parameter peaks at about 0.50 ($S/S_{bulk} \approx 1.033$) for the as-implanted samples. After 200 °C annealing, the S parameter is increased, peaking at 0.51-0.515 ($S/S_{bulk} \approx 1.054$-1.064).

Fig. 4.3(b) shows PAS results for different annealing temperatures at a single implantation dose, 3×10^{13} ions·cm^{-2}. As annealing temperature increases, the S parameter is also increased, to a maximum of ~0.525 ($S/S_{bulk} \approx 1.085$) for the 300 °C anneal. The peak position also shifts with increased annealing temperature to lower positron energies, corresponding to shallower depth.

Turning to indentation response, AFM micrographs indicate a sharp change in the deformation characteristics of samples implanted to 1×10^{13} ions·cm^{-2} and 3×10^{13} ions·cm^{-2} and unannealed, compared to unimplanted Ge. Fig. 4.4(a) shows the response for unimplanted Ge indented to 100 mN. Radial/median cracks emanate from the top and bottom of the impression. There is minimal uplift around the impression, indicating an ideal elastic-plastic deformation without pile-up of material. This is a typical response for a brittle material. By contrast, the indent in the implanted sample [Fig. 4.4(b)] features no cracking. The impression is surrounded by a ring of piled-up material, indicating extrusion under load. Optical microscopy on large arrays of indents confirmed that these features were common to all indents made in these samples.

Suppression of radial/median cracking and extrusion of material was also observed around indents in the as-implanted 1×10^{13} ions·cm^{-2} dose sample. The indent morphology of 3×10^{12} ions·cm^{-2} dose sample was indistinguishable from unimplanted Ge. Samples implanted to 1×10^{13} ions·cm^{-2} and 3×10^{13} ions·cm^{-2} and subsequently annealed at 200 °C featured radial/median cracking and minimal extrusion when indented to 100 mN. Some lateral cracking was observed around indents to 100 mN in the 1×10^{13} ions·cm^{-2} dose sample, both as-implanted and annealed. These observations are summarised in Table 4.1.

Raman microspectroscopy confirmed the crystalline composition of the implanted samples. Raman spectra from 3×10^{12} ions·cm^{-2} and 1×10^{13} ions·cm^{-2} dose samples were identical to the spectrum of unimplanted Ge. The spectrum from the 3×10^{13} ions·cm^{-2} dose as-implanted sample was similar, but featured a slight asymmetric shoulder on the low-energy side of the Ge-I peak (Fig. 4.5). This feature disappeared after annealing at

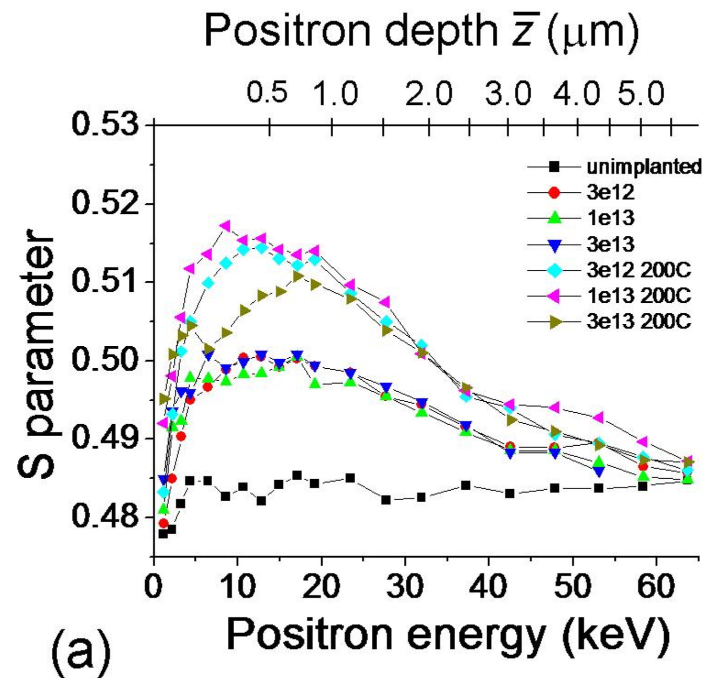

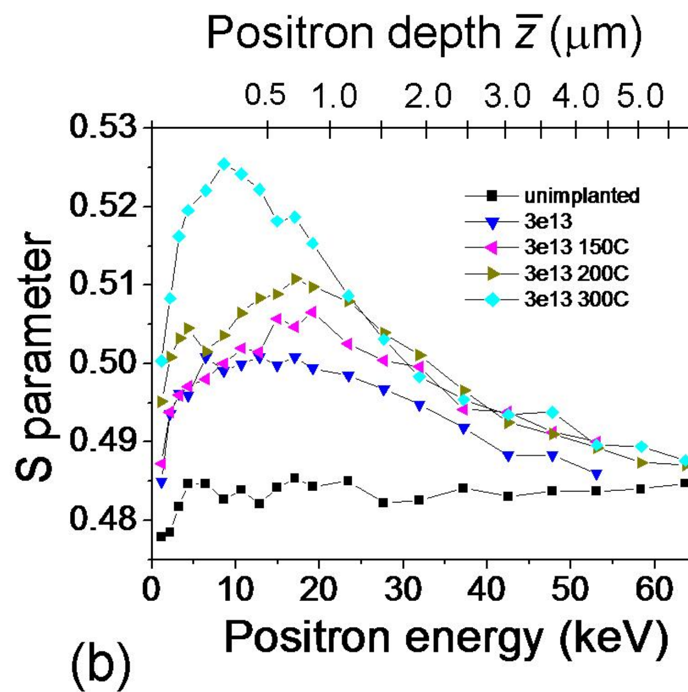

Figure 4.3: Results of positron analysis on as-implanted and annealed samples. (a) S parameter vs. positron energy for all doses, as-implanted and annealed at 200 °C. (b) S parameter vs. positron energy for 3×10^{13} ions·cm^{-2} dose, annealed at 3 different temperatures.

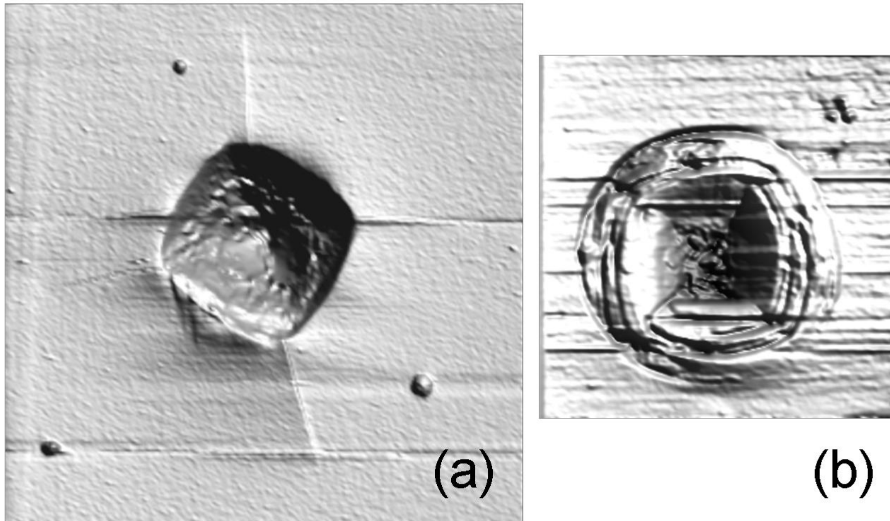

Figure 4.4: AFM micrographs of indents to 100 mN. (a) Indent in unimplanted Ge (10×10 μm image). (b) Indent in sample implanted to 3×10^{13} ions$\cdot$cm^{-2} and unannealed (7×7 μm image).

Table 4.1: Morphological features of indents to 100 mN in implanted c-Ge for as-implanted and annealed samples.

		3×10^{12}		1×10^{13}		3×10^{13}	
Feature	pristine	as-imp.	ann.	as-imp.	ann.	as-imp.	ann.
extrusion	×	×	×	✓	×	✓	×
radial cracking	✓	✓	✓	×	✓	×	✓
lateral cracking	×	×	×	✓	✓	×	×

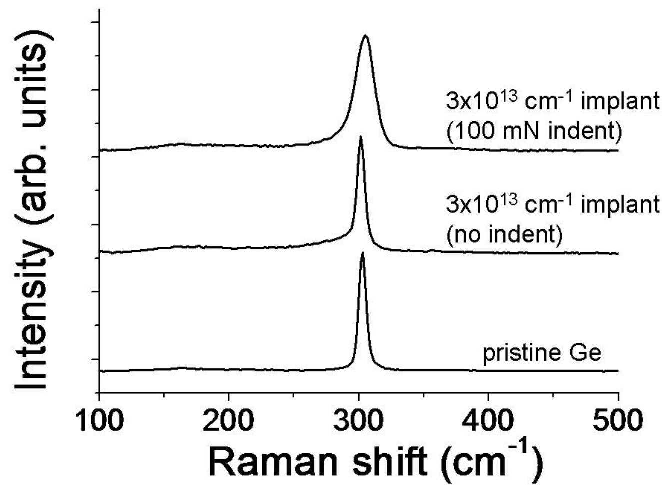

Figure 4.5: Raman spectra from pristine Ge and from the 3×10^{13} ions·cm^{-2} dose as-implanted sample.

200 °C. Indents made in both as-implanted and annealed samples for all doses featured only a broadened and up-shifted Ge-I peak, as seen in Fig. 4.5, with no signs of additional phases.

Fig. 4.6 shows cross-sectional TEM of an indent to 100 mN in the as-implanted 3×10^{13} ions·cm^{-2} dose sample. There is a well-defined indent damage region in both the implanted layer and the underlying material. In the underlying Ge, the damage consists of twin bands on $\{111\}$ planes and punched-out dislocations, very similar to what is observed for pristine Ge. The damage in the implanted layer is much more disordered. Dislocations appear to be present, but there are no clearly defined twin bands or slip traces. Extrusion and uplift is apparent at the edges of the impression. SADP from the damage zone with the implanted layer shows no signs of additional phases, but does show that the Ge-I has become partially polycrystalline [Fig. 4.6(b)]. Outside the damaged region of the implanted layer, only single-crystal Ge-I is observed [Figs. 4.6(c) and 4.6(d)].

Fig. 4.7 is a TEM micrograph of an indent to 100 mN made in the 200 °C-annealed 3×10^{13} ions·cm^{-2} dose sample. After annealing there is no longer visible evidence of the implanted layer. The plastic damage throughout the indented region is similar to that in unimplanted Ge, consisting of twinning, slip, and tangles of dislocations. However, cracking is much more extensive than for unimplanted Ge. Usually, an indent to this load in unimplanted Ge would feature a single median crack. In this case, in addition to deep median cracking, there are several branching lateral cracks parallel to the surface. Moreover, there are voids and microcracks within the plastic region, as highlighted in Fig.

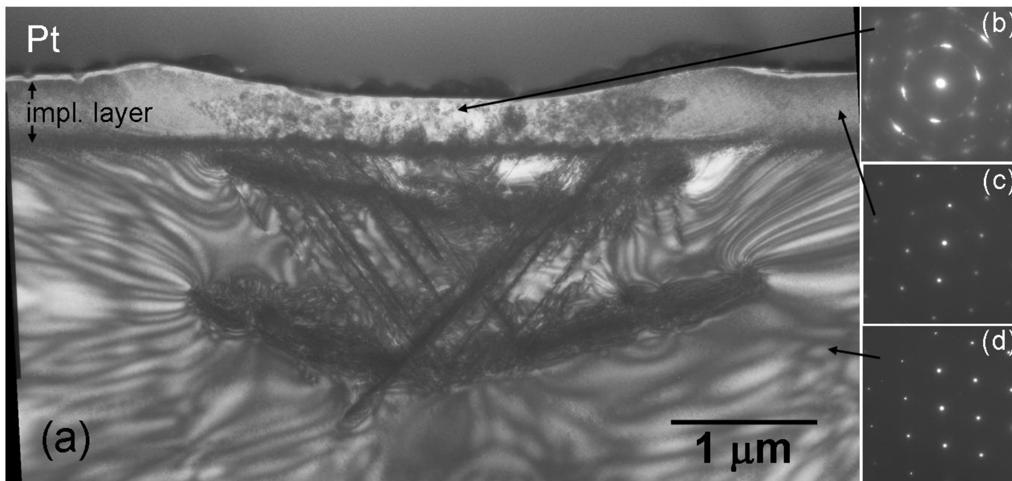

Figure 4.6: XTEM of indent to 100 mN in 3×10^{13} ions·cm^{-2} as-implanted sample. (a) BF image of indent. (b) SADP from indent damage region within implanted layer. (c) SADP from implanted layer outside indented region. (d) SADP from underlying pristine Ge.

4.7(b). Fig. 4.7(c) shows another indent in the annealed implanted sample. This indent also features extensive sub-surface cracking.

Hardness values were calculated from nanoindentation P-h curves for both as-implanted and 200 °C annealed samples. The results are plotted in Fig. 4.8. The measured hardness of the lowest dose as-implanted sample is equal to that of unimplanted Ge, at $\sim$10.7 GPa; the hardness drops for the 1×10^{13} ions·cm^{-2} dose as-implanted sample, and drops further still for the 3×10^{13} ions·cm^{-2} dose as-implanted sample. After annealing, hardness increases to a measured value of $\sim$11.1 GPa for all three implanted samples, slightly above the hardness of unimplanted Ge.

Fig. 4.9 shows values of elastic modulus as a function of implanted dose for both as-implanted and annealed samples. The trend is similar to that for the hardness. For the as-implanted samples, elastic modulus is unchanged for the lowest dose sample, and subsequently decreases with increasing dose. For the annealed samples the elastic modulus is independent of dose and approximately equal to that for pristine Ge.

A P-h curve for the 3×10^{13} ions·cm^{-2} as-implanted sample is shown in Fig. 4.10, with a P-h curve from unimplanted Ge for comparison. In both cases the unloading curve is essentially featureless. The loading curve for the unimplanted sample features several small pop-ins. The loading curve for the implanted sample features a single pop-in at $\sim$23 mN. The pop-in may be a signature of the cracking seen in Fig. 4.7. Whereas for the unimplanted sample the location of the pop-ins varied somewhat from test to test, for the implanted sample the single pop-in consistently occurred at the same load.

As described in the Method section, in some cases indents were made in samples prior

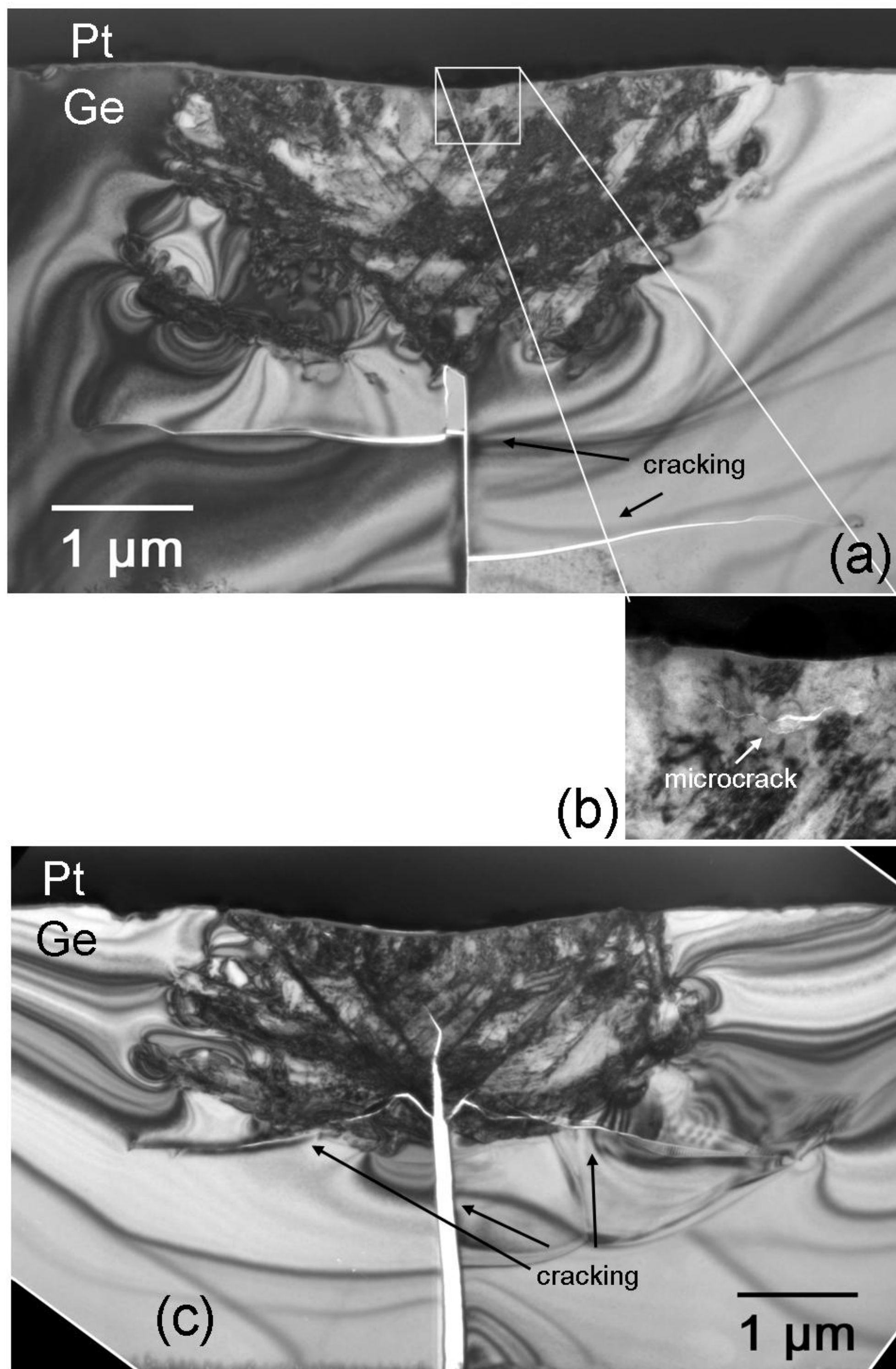

Figure 4.7: (a) BF TEM image of indent to 100 mN in 3×10^{13} ions·cm^{-2} implanted 200 °C annealed sample. (b) Enlargement of damage region, showing microcrack. (c) BF TEM image of a different 100 mN indent in the same sample.

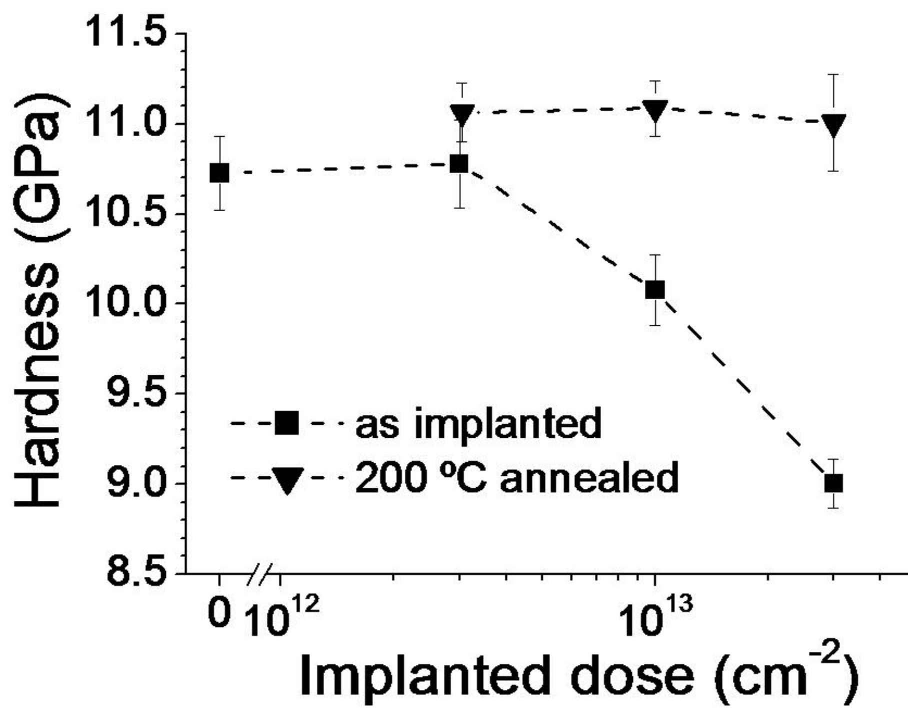

Figure 4.8: Nanoindentation hardness vs implanted ion dose for as-implanted and annealed Ge samples.

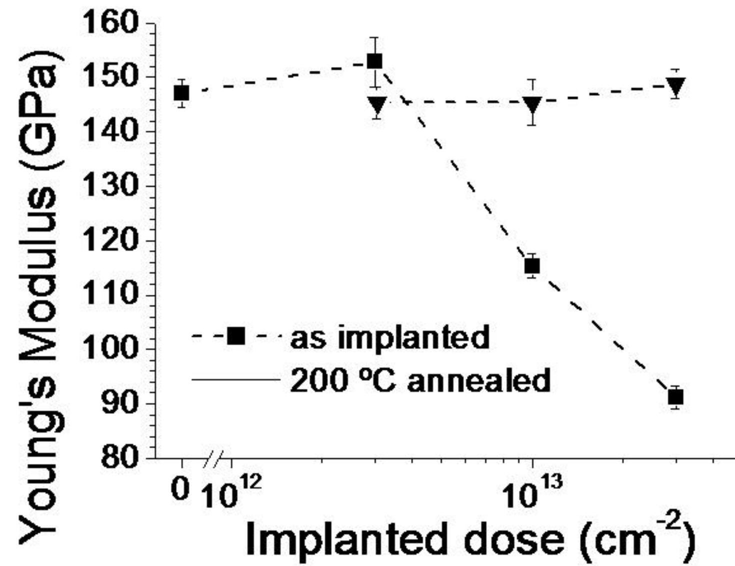

Figure 4.9: Elastic modulus E vs implanted ion dose for as-implanted and annealed Ge samples.

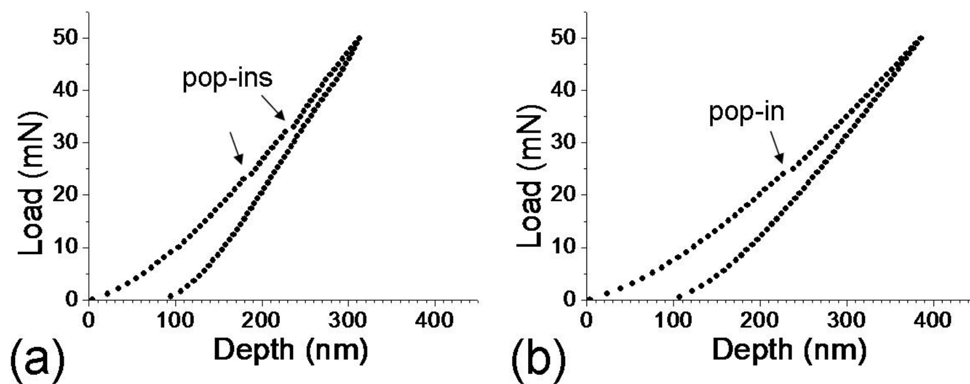

Figure 4.10: (a)P-h curve to 50 mN in unimplanted Ge. (b) P-h curve to 50 mN in $3{\times}10^{13}$ ions$\cdot$cm^{-2} as-implanted Ge.

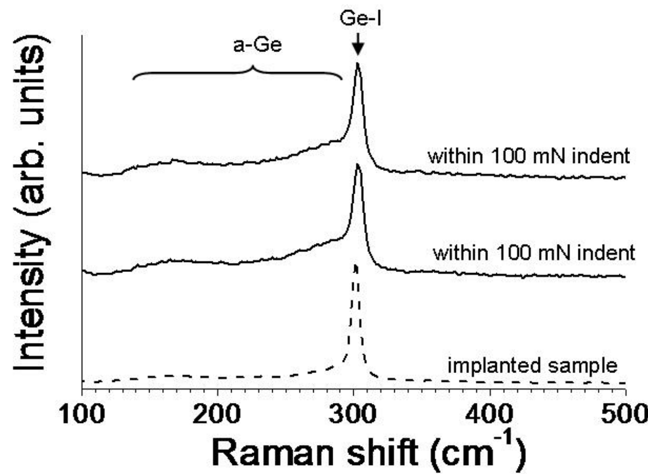

Figure 4.11: Raman spectra from sample regions that were indented to 100 mN and subsequently implanted.

to ion implantation. These indents were inspected by Raman microspectroscopy after implantation. Results are shown in Fig. 4.11. In addition to the Ge-I peak, distinct a-Ge bands were observed in Raman spectra from these indents. The overall morphological appearance of these indents was the same as that of indents in pristine material.

4.4 Discussion

Both positron annihilation measurements (Fig. 4.3) and TEM (Fig. 4.2) show that a very high density of defects is present after implantation in the samples investigated. The similarity of the as-implanted PAS spectra is due to saturated trapping due to high open volume-defect concentrations. No Doppler broadening positron studies on irradiated Ge were found in the literature, although positron lifetime studies have been reported. [93,94] However, considerable work has been done on irradiation defects in Si, including a theoretical calculation of the S parameter for different-sized vacancy clusters. [70] By analogy, the same trend as for Si can be expected for Ge. One would expect an increase in the S parameter with increasing vacancy-cluster size. However, below the saturation limit ($\sim 10^{15}$ cm^{-3}), the S parameter is also dependent on the number of defects, as well as the defect type, making interpretation of the data somewhat ambiguous. [95] The S parameter value for the as-implanted samples is $S/S_{bulk} \approx 1.033$. This probably corresponds to a simple vacancy-type defect, perhaps the divacancy or a vacancy-impurity complex. [96] After the 200 °C anneal, for all samples the peak S parameter increases to $S/S_{bulk} \approx 1.06$. Since the total defect concentration is not likely to increase by anneal-

ing, this must be due to the presence of larger vacancy clusters after annealing. That is, smaller open volume defects coalesce under annealing to form larger ones. [94] At 300 °C, the S parameter increases further to $S/S_{bulk} \approx 1.085$, which must be due to the formation of even larger defect clusters. Another feature of increased annealing temperature is a shift of the S parameter peak to lower positron energies. This indicates a shift in the peak defect concentration (or the location of the largest open volume defects) to shallower sample depths.

Deep level transient spectroscopy (DLTS) has been used to investigate the annealing dependence of point defects in electron-irradiated Ge. [96, 97] Most point defects were found to anneal out completely at or below 200 ° C. By contrast, more complex defects generated by 1 MeV ion implantation were found to be persistent to 500 ° C. Generally, after annealing, simple defects generated by ion implantation either annihilate or coalesce to form clusters, rod-like defects, stacking-fault platelets, and dislocation loops. [59, 98]

Mechanically, the as-implanted layers for the higher doses of 1×10^{13} ions·cm^{-2} and 3×10^{13} ions·cm^{-2} show a lower resistance to plastic flow than unimplanted Ge. Reduced hardness is measured for those samples (Fig. 4.8). This softening manifests in pronounced extrusion around indents [Fig. 4.4(b)]. The soft implanted layer is constrained by the harder undamaged Ge beneath, and is pushed to the edges of the contact periphery during indentation. Cracking is suppressed because plastic flow is a more favourable means of relieving stress.

Mechanical softening at a high defect concentration is contrary to experience with many materials, particularly metals, in which crystal defects are generally associated with strengthening. [87, 88] In metals, the chief barrier to slip is the presence of existing defects, and hardness may vary over orders of magnitude for high and low defect densities. In covalent semiconductors, however, hardness is a more intrinsic property governed by the energy of breaking and reforming chemical bonds, [89,99] and the main barrier to slip is the high Peierls stress in these materials. [73, 100, 101]

One possible cause of the softening is that implantation generates a large number of point defects and small defect clusters, and a correspondingly high density of dangling bonds. These dangling bonds may aid the motion of dislocations. Dislocation mobility in Ge has been found to be controlled by the formation and motion of kinks along the dislocation line, [99, 102–104] which can only take place by atomic bond breaking. A high dangling bond density may lower the barrier to this process of dislocation motion. After annealing, simple defects coalesce to form line defects (dislocations) and other extended defects, repairing many dangling bonds. These extended defects may act as a barrier to dislocation motion. Indeed, the hardness of annealed implanted samples is slightly higher than that of pristine Ge (Fig. 4.8).

An alternative explanation for the softening is that there are nanosized pockets of amorphous material within the implanted layer. Since a-Ge is softer than c-Ge (see Chapter 5), the total hardness would be reduced. Although ion-implanted amorphous layers in Ge recrystallise by solid-phase epitaxy at temperatures of 300-400 ° C, [105, 106] isolated small amorphous zones may recrystallise at much lower temperatures, [107] so this scenario is not necessarily inconsistent with the hardness recovery after annealing. The fraction of amorphous material required to produce the observed softening can be estimated. A simple composite model for an evenly distributed two-phase material predicts a hardness of: [108, 109]

$$H_{av} = f_{cGe} H_{cGe} + f_{aGe} H_{aGe} \tag{4.1}$$

H_{av} is the composite hardness, and f_x and H_x are the volume fraction and hardness respectively of each phase. Using the measured hardnesses in Fig. 4.8, and taking a hardness for a-Ge of $H_{aGe} = 7.6$ GPa (see Chapter 5), Eq. 4.1 predicts an amorphous volume fraction of $f_{aGe} = 0.2$ for the 1×10^{13} ions·cm^{-2} dose sample, and $f_{aGe} = 0.55$ for the 3×10^{13} ions·cm^{-2} dose sample. Volume fractions of 20% and 55% a-Ge are improbable, since these concentrations would almost certainly be detected by TEM and Raman spectroscopy. This indicates that the hardness reduction is not due to the presence of softer a-Ge pockets, but rather it is attributable to the general disorder generated by ion implantation, and in particular the high density of dangling bonds.

In contrast to Ge, Si exhibits a much smaller change in mechanical properties after non-amorphising ion implantation. Williams *et al.* looked at the indentation response of Si implanted at 250 ° C and observed only a small decrease in hardness. [110] An explanation for this is that the hardness of Si is mainly controlled by the pressure-induced phase transformation, [19, 22, 23] and the threshold for the phase transformation would not be expected to be significantly affected by the presence of disorder.

Finally, it is interesting that TEM shows considerable sub-surface cracking for indents in the highest-dose annealed sample. Microcracks [Fig. 4.7(b)] and voids are observed even within the central plastic zone, where cracking is usually suppressed due to the highly compressive stresses. [111] The unusually extensive cracking may be due to the larger voids formed after annealing. These voids may act as preferential nucleation sites for cracks, and also aid crack growth.

4.5 Concluding remarks

After high-energy, high-fluence self-ion implantation, crystalline Ge contains a high density of defects, including small-size open volume defects. Upon thermal annealing, these evolve into larger vacancy clusters. As-implanted specimens exhibit a dose-dependent mechanical softening relative to unimplanted Ge. This is likely to be due to the presence of large numbers of point defects and dangling bonds, which could facilitate dislocation formation and kink motion and consequently increase dislocation mobility. Specimens annealed at 200 °C show the opposite effect, a slightly increased hardness relative to unimplanted Ge. These indicates that the defect structures formed after annealing act as an impediment to dislocation motion. Indents in annealed samples also exhibit extensive cracking, both within and outside of the plastic zone, which may be a consequence of the presence of the vacancy clusters.

Implantation damage is highly dependent on the mass of the incoming ion. Light ions, which generate relatively few displacements per incoming ion, tend to produce more diffuse and homogeneous damage consisting mainly of point defects, whereas heavy ions produce localised, heavily disordered or completely amorphous regions. In this case Ge was used, which has an intermediate mass. Further studies would be interesting to investigate the effect of implantation of lighter and heavier ions on the mechanical properties. This would help to clarify the mechanisms responsible for the observed softening. It would also be interesting to perform a similar study on compound semiconductors such as GaAs and InP. Like Ge these materials deform by shear plasticity under indentation and might display a similar change in mechanical properties after ion implantation.

CHAPTER 5

Nanoindentation of amorphous Ge

5.1 Introduction

Amorphous solids have been the subject of intensive research for over 70 years. [112] These materials are distinguished from crystalline solids by the absence of long-range order. However, the short-range bonding in covalent amorphous solids such as Ge and Si is similar to that in the stable crystalline structure. Of interest is the proposal of Gao *et al.* that the mechanical hardness of covalent semiconductors is an intrinsic property controlled by bond strength. [89] According to this theory, the hardness values of amorphous Ge (a-Ge) and amorphous Si (a-Si) should be close to the hardnesses of the respective crystalline forms.

Crystalline Ge can be amorphised by high-fluence ion implantation. When this as-implanted amorphous phase is annealed at temperatures below the crystallisation threshold, structural relaxation is observed, resulting in a drop in free energy [106] and reduced disorder (bond length and bond angle distortion). [113–116] Although the structure of these two states (*i.e.* as-implanted and 'relaxed' a-Ge) is not fully understood, one point of view is that the 'relaxed' state approaches the condition of a continuous random network (CRN) with fourfold coordination throughout, whereas the 'unrelaxed' state contains a higher concentration of dangling bonds and under-coordinated atoms. [117] DAC experiments have shown that a-Ge and a-Si, like their crystalline counterparts, undergo a transition at elevated hydrostatic pressures to a higher-coordination metallic phase. [118]

Under hydrostatic compression in a diamond-anvil cell (DAC), a-Ge undergoes a transformation to a metallic phase at $\sim$6-7 GPa, [118–122] marked by a large drop in resistivity, [118] volume decrease and changes in optical properties, [119, 120] and change in the atomic structure. [120, 121] There is some disagreement as to the phase formed at 6-7 GPa: some authors find it to be β-tin structure Ge, [120, 121] but others describe it as a high-density amorphous phase (hda-Ge). [118, 122, 123] Intriguingly, upon unloading, Ge-I is obtained. [118–121] An *in situ* XRD study [121] by Imai *et al.* found that the metallic phase first transformed to bc-8 Ge, then to Ge-I. This sequence of transformations

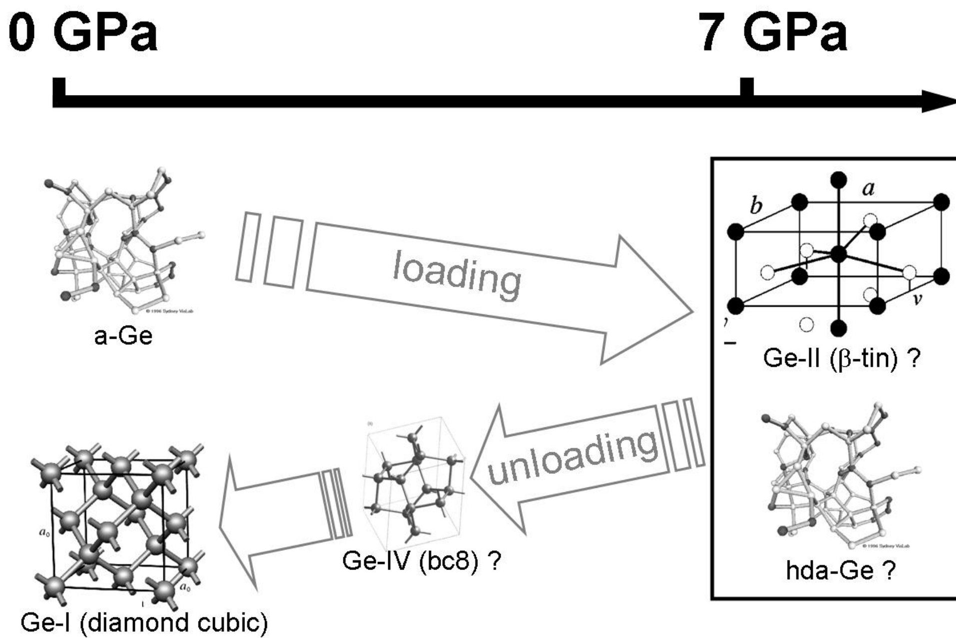

Figure 5.1: Schematic of high-pressure phase transformations of a-Ge observed in diamond-anvil cell (DAC) experiments.

is illustrated in Fig. 5.1.

The nanoindentation response of amorphous Si (a-Si) to has been studied in some detail. [110, 124, 125] The preferred deformation mechanism is found to depend on the method of preparation. Relaxed a-Si deforms via a pressure-induced phase transformation similar to crystalline Si (c-Si). In contrast, unrelaxed a-Si shows a tendency to deform via shear flow, except under confinement. Both forms are significantly softer than c-Si. To date, however, there has only been one nanoindentation study on amorphous Ge (a-Ge). [126] This study was performed on a-Ge films prepared by low-temperature electron-beam evaporation onto a GaAs substrate. Ge-I was observed in residual impressions after indenting, and the structural state of the a-Ge film was not examined. Furthermore, deposited amorphous films can contain significant porosity and impurities [127] that may influence their deformation behaviour.

In this investigation, high-purity a-Ge is prepared by self-ion implantation. The nanoindentation response of both relaxed and unrelaxed a-Ge is examined. Evidence is found in both cases of a pressure-induced transformation to a high-density metallic phase, distinct from the normal β-tin phase formed by c-Ge at high pressures. Both forms of a-Ge are significantly softer than crystalline Ge-I.

5.2 Experimental details

Undoped Ge(100) was implanted with 800 keV energy Ge ions at room temperature. Implants were carried out to a high fluence to produce a continuous amorphous layer. Samples were implanted to fluences of 1×10^{14} ions·cm^{-2}, 3×10^{14} ions·cm^{-2}, and 3×10^{15} ions·cm^{-2}, with ion fluxes 1.5×10^{11} to 6×10^{11} ions·cm^{-2}·s^{-2}. Raman spectroscopy confirmed that the two highest-dose samples were fully amorphous up to the surface. The spectrum of the 1×10^{14} ions·cm^{-2} dose sample featured a small c-Ge peak in addition to the a-Ge band, indicating that at this lower dose a thin region near the surface may have remained crystalline.

Ion distributions and damage profiles were simulated using TRIM. Results are plotted in Fig. 4.1 in Chapter 4. From TRIM simulations an amorphous layer thickness of 600-700 nm might be expected.

After implantation, some specimens were annealed under argon flow in a tube furnace for 30 min at 250 °C. Annealing at this temperature relaxes the a-Ge structure [106, 115, 116] without significant recrystallisation. [105, 106] In this chapter, the annealed specimens will be referred to as 'relaxed', while as-implanted specimens will be referred to as 'unrelaxed.'

Specimens were indented with the UMIS-2000, using a spherical tip with radius ∼4.3 μm. Maximum loads of up to 100 mN were used, with loading and unloading rates of dP/dh $\approx$ 1 mN·s^{-1}, in a single load cycle with no hold period except where otherwise specified. Hardness values were calculated from tests to 50 mN with the spherical tip, using the Oliver and Pharr analysis. [42]

Raman spectra were obtained from indents with a Renishaw 2000 Raman microscope, using the 632.8 nm line of a HeNe laser. The laser power was kept low to avoid annealing any metastable phases.

The state of disorder in relaxed and unrelaxed amorphous specimens was gauged by measuring the linewidth of the TO-like Raman band of a-Ge centred at ∼270 cm^{-1}. Broadening of this band is proportional to the bond angle distribution in the amorphous network, [114] giving a measure of disorder. The linewidth was found from Raman spectra by measuring the half-width on the high-frequency side of the band at half-maximum.

Cross-sections of indents for TEM were prepared using the xT Nova NanoLab 200 dual-beam FIB. Indents were protectively coated with Au before being placed in the FIB. TEM specimens were imaged with the Philips CM 300, operating at 300 keV.

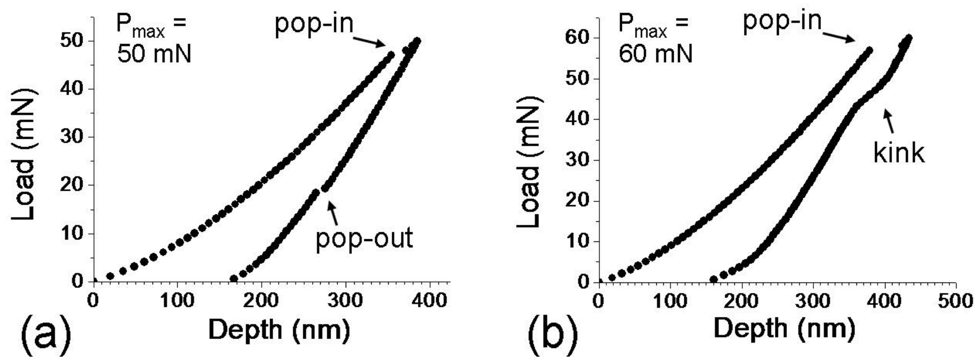

Figure 5.2: P-h curves for indents in a-Ge samples, (a) unrelaxed and (b) relaxed.

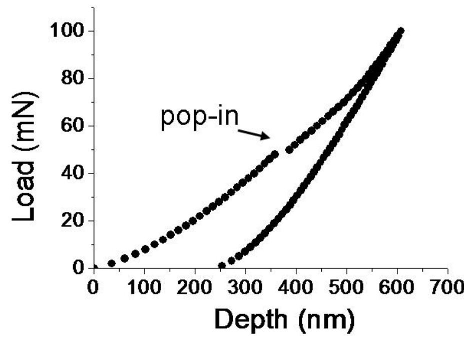

Figure 5.3: P-h curve to 100 mN in unrelaxed a-Ge sample.

5.3 Results

Fig. 5.2 illustrates load-displacement features of indents in the amorphous layers. Except where otherwise indicated, results presented are for the 3×10^{15} ions·cm^{-2} dose sample. P-h curves from tests consistently featured a single pop-in on loading at a well-defined load. For the unrelaxed sample, this pop-in was found at 48-50 mN [Fig. 5.2(a)]. For the relaxed sample, the pop-in occurred at 52-60 mN [Fig. 5.2(b)]. Tests performed to a maximum load just above the pop-in load usually featured a small pop-out on unloading as in Fig. 5.2(a), or a 'kink' as in Fig. 5.2(b). However, tests to a maximum load below the pop-in load typically had a featureless unloading curve, and likewise for tests to a maximum load well above the pop-in load, as shown for the 100 mN load indent in Fig. 5.3. Additionally, tests made to a load just above the pop-in threshold, but with a hold period applied at maximum load, tended not to feature a pop-out or kink on unloading, as shown in Fig. 5.4.

The measured hardness of the specimens is shown in Fig. 5.5. Each plotted hardness

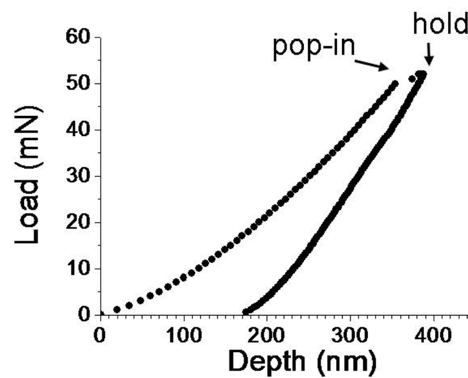

Figure 5.4: P-h curve to 50 mN, with a 30 s hold at maximum load, in unrelaxed a-Ge sample.

value represents an average from a number of tests, with error bars representing scatter within the averaged values (one standard deviation). The hardness is ~7.5 GPa for the 3×10^{14} ions·cm^{-2} and 3×10^{15} ions·cm^{-2} dose specimens, compared to the hardness for c-Ge of ~10.7 GPa (Chapter 4). The hardness is ~8.5 GPa for the 1×10^{14} ions·cm^{-2} dose specimens, a slight increase which is consistent with the observation of remnant crystallinity. For all doses, the hardness values of relaxed and unrelaxed specimens are the same within error.

The Raman spectrum for the lowest dose specimen (1×10^{14} ions·cm^{-2}) with no indent present featured broad amorphous bands and a small Ge-I peak. The spectrum from the higher dose specimens (with no indent) featured only the broad amorphous bands.

For indents in the 3×10^{14} ions·cm^{-2} and 3×10^{15} ions·cm^{-2} dose specimens at lower loads of 50-60 mN, the Raman spectrum varied: some indents contained only a-Ge, whilst other indents contained crystalline Ge-I in addition to a-Ge. Indents to loads of 100 mN more consistently featured the Ge-I peak, sometimes with little or no a-Ge. Indents to loads of 100 mN in the 1×10^{14} ions·cm^{-2} dose sample similarly featured a large Ge-I peak and little or no a-Ge. Some representative spectra are shown in Fig. 5.6. The observed phases in indents were similar for both relaxed and unrelaxed samples.

Fig. 5.7 shows the linewidth of the TO-like Raman band for unrelaxed and relaxed specimens. The linewidth varies slightly with implantation dose, being narrowest for the 3×10^{14} dose. For all doses, the linewidth decreases after annealing, indicating a reduction of disorder.

TEM of an indent in an unrelaxed specimen is shown in Fig. 5.8. Outside the indent, the implanted layer shows the uniform contrast characteristic of pure amorphous material, which is confirmed by the DP [Fig. 5.8(b)]. Directly beneath the indent, however, there is

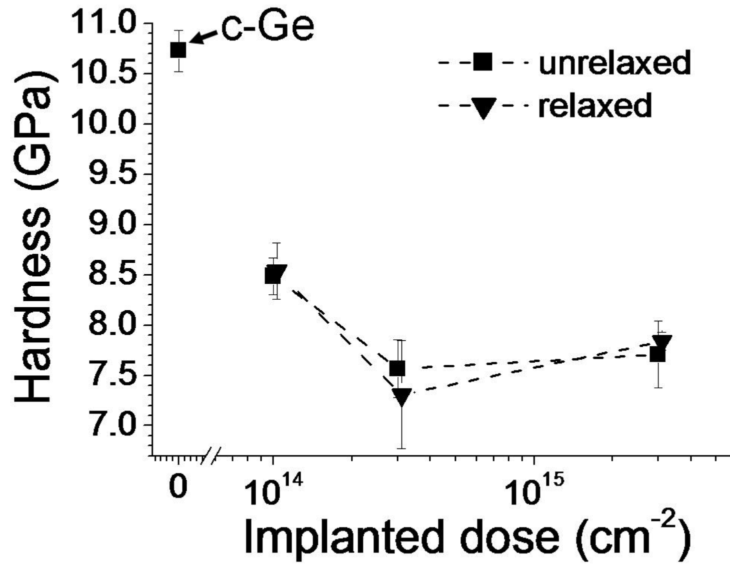

Figure 5.5: Hardness vs implanted dose for unrelaxed and relaxed a-Ge samples.

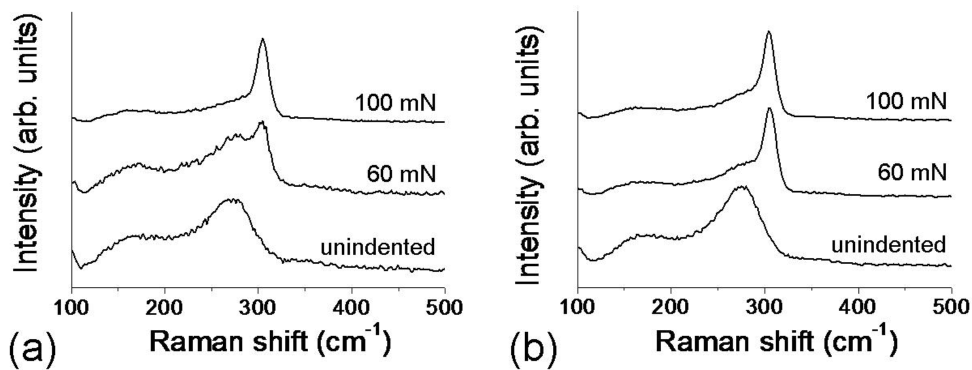

Figure 5.6: Raman spectra taken from indents in a-Ge, (a) unrelaxed and (b) relaxed. Undeformed a-Ge spectra shown for comparison.

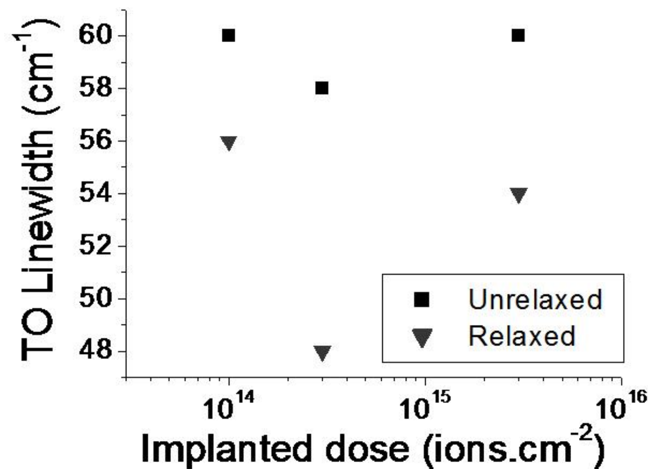

Figure 5.7: TO linewidth measured from Raman spectra for unindented specimens plotted vs implantation dose, for both unrelaxed (as-implanted) and relaxed (250 °C annealed) specimens.

a large recrystallised region. SADP from this region shows that it contains polycrystalline Ge-I [Fig. 5.8(c)]. No additional spots are present in the DP, indicating that there are no other crystalline phases. The shape of the recrystallised zone is roughly hemispherical, and does not extend into the underlying crystalline material.

Fig. 5.9 shows TEM of an indent in a relaxed specimen. The deformation pattern is similar to that of the unrelaxed specimen, consisting of a hemispherical crystallised zone containing polycrystalline Ge-I without additional phases. In this case a few twins can be seen in the underlying c-Ge, directly below the interface.

5.4 Discussion

To help understand the indentation response of a-Ge, it is instructive to consider the sequence of transformations of the material in a DAC. As outlined in the Introduction, a-Ge transforms to a metallic phase at ~6-7 GPa, either to β-tin Ge or to hda-Ge. An *in situ* XRD study [121] found that on unloading the metallic phase first transforms to bc-8 Ge, which is unstable at room temperature and ambient pressure and reverts to Ge-I. This is in contrast to the behaviour of β-tin Ge formed by compression of Ge-I, which normally transforms to st-12 Ge on pressure release (Fig. 1.1). This indicates that the high-pressure phase obtained from compression of a-Ge is different in some way to that obtained with Ge-I. It could be that Ge-I transforms under pressure to β-tin Ge-II whereas a-Ge converts to hda-Ge. [122, 123] This difference may account for the different pressure (hardness) at

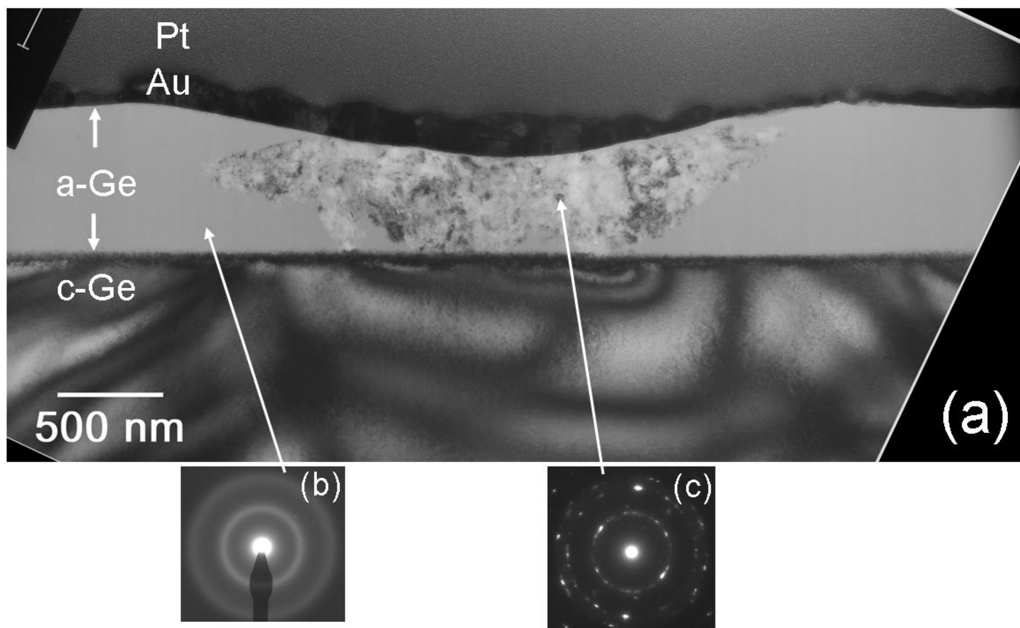

Figure 5.8: (a) BF XTEM micrograph of an indent to 60 mN in unrelaxed a-Ge. (b) SADP from the amorphous layer, away from the indent. (c) SADP from recrystallised region under indent.

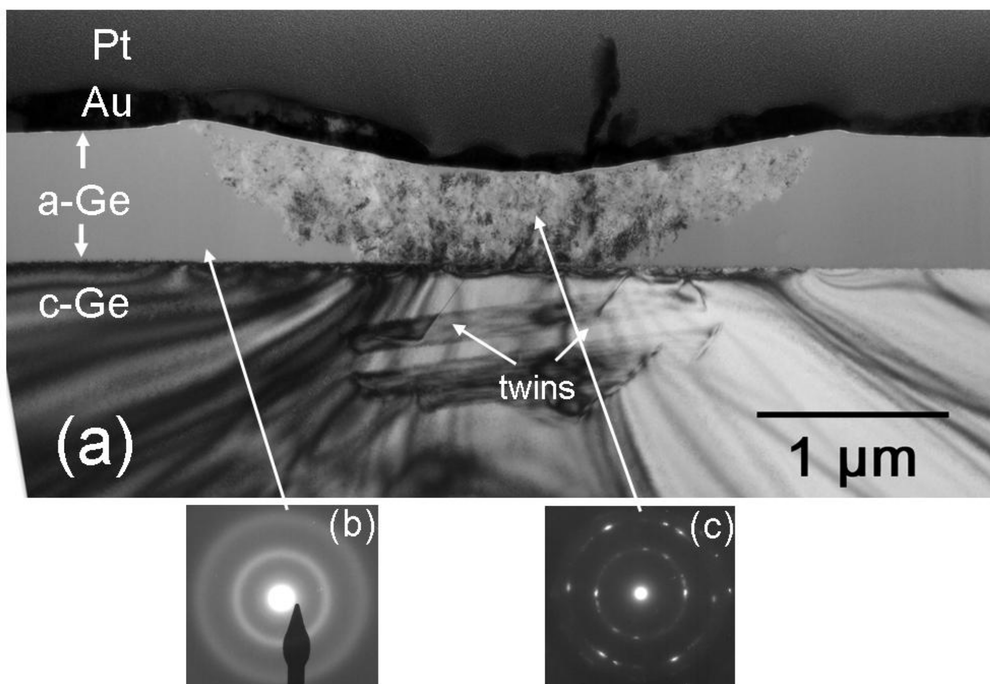

Figure 5.9: (a) BF XTEM micrograph of an indent to 60 mN in relaxed a-Ge. (b) SADP from the amorphous layer away from the indent. (c) SADP from recrystallised region under indent.

which transformation is observed for Ge-I and a-Ge. Indeed, Shimomura *et al.* observed a second metal-to-metal transition in a-Ge at $\sim$10 GPa, which may be a hda-Ge to Ge-II conversion, consistent with their observations of st-12 Ge on pressure release, [118] whereas Ge-I was obtained after pressure release of hda-Ge from $\sim$7 GPa.

Given the DAC observations, the finding in this study that Ge-I is observed within residual indents in a-Ge is consistent with a high-pressure phase transformation during indentation. Further supporting this view, the measured hardnesses of relaxed and unrelaxed a-Ge are around 7 GPa (Fig. 5.5), the pressure that a-Ge phase transforms in DAC observations. [118–122] The similarity of hardness for relaxed and unrelaxed specimens also makes sense if phase transformation is the deformation mechanism in each case, and the critical pressure for phase transformation is the governing factor. By contrast, relaxed and unrelaxed ion-implanted a-Si feature differing hardnesses, because they exhibit different deformation responses to indentation. [124] For a-Ge, however, phase transformation appears to be decisively favoured regardless of the state of relaxation.

The dependence of the P-h unloading curve features on maximum load and hold time may shed further light on the sequence of phase transformations during the indentation cycle. For maximum indentation loads of 50 to 60 mN, a pop-out was observed (Fig. 5.2. Such a feature is indicative of a sudden volume change, in c-Si associated with the transformation of Si-II to lower-density Si-III and Si-XII. [22, 23, 128] For higher maximum loads in a-Ge, however, no pop-out was observed (Fig. 5.3), although Ge-I was still found after indentation (Fig. 5.6). Similarly, when a hold period was employed at a lower peak load, pop-out was less frequently observed (Fig. 5.4). If no pop-out is present, this may suggest that the high-pressure phase is transforming continuously throughout the unloading stage, rather than suddenly at a discrete load. One possible explanation for this is the presence of a small amount of the transformed phase prior to unloading that can form during extended loading through expulsion of hda-Ge from the edges of the indenter contact, or during the hold period. Although the formation of a lower-density phase under load seems counterintuitive, it is consistent with the DAC observation of Shimomura *et al.* that some of the metallic phase reverted to a semiconducting phase over time whilst holding at constant pressure. A small amount of bc-8 Ge or Ge-I would then act as a nucleus on unloading and prevent a sudden transformation.

Finally, these findings may be relevant to the intriguing phenomenon known as "explosive crystallisation." This is the phenomenon whereby the recrystallisation of a small volume of a-Ge can trigger a runaway reaction that recrystallises a large region of amorphous material. [129] This occurs because the a-Ge to Ge-I transformation is an exothermic reaction. Under appropriate conditions the transformation of a region of amorphous film releases sufficient heat to recrystallise adjoining material, which in turn releases more

heat, and so on. The original paper to report explosive crystallisation in a-Ge found that it could be triggered by, amongst various methods, "pricking with a sharp point," [130] that is to say, an indentation process. It seems plausible that, in this process, initial crystallisation occurred via a high-pressure phase transformation. Explosive crystallisation beyond the indenter contact area was not observed in the present study. This may have been as a result of the confining (compressive) effect of the indenter or the fact that heat loss to the underlying c-Ge bulk sample was too high. Heat dissipation could be suppressed by using thick amorphous films and elevated temperatures. [130,131] A study of indentation-induced explosive crystallisation of a-Ge would complement the extensive research done into laser-induced explosive crystallisation. [129–132]

5.5 Concluding remarks

The nanoindentation response of ion-implanted amorphous Ge has been investigated. Unlike c-Ge, a-Ge exhibits a high-pressure phase transformation during indentation. This occurs for both relaxed and unrelaxed amorphous samples. The sequence of phase transformations, resulting in the formation of crystalline Ge-I, is similar to that observed in DAC studies on a-Ge. The metallic transition pressure of a-Ge under DAC conditions is significantly lower than that of c-Ge, which may explain why a-Ge deforms preferentially by phase transformation, whereas c-Ge deforms under the same indentation conditions by shear plasticity.

CHAPTER 6

Nanoindentation of germanium thin films on silicon

6.1 Introduction

Ge is receiving renewed attention as an electronic material for numerous applications, [2, 3, 5, 6] and high-speed transistors, in part because it is highly compatible with existing Si processing technologies and should be relatively easy to integrate into Si devices. [3] Because of its high cost relative to Si, Ge is likely to be used in these applications as an epitaxial thin film on a Si substrate. As detailed in Chapter 1, Ge has been found to deform by mechanical twinning and conventional dislocation slip, [30] whereas Si in contrast has been shown by a number of studies to deform under indentation primarily by transformation to the Si-II phase. [19, 22, 23] Ge may therefore show different behavior to Si during handling and machining in device manufacture and during operation.

This chapter examines the nanoindentation response of thin Ge films epitaxially grown on a Si(100) substrate, with thicknesses ranging from 50 nm to 600 nm. The inelastic deformation response is found to vary dramatically depending on the film thickness and applied load: in thin films, phase transformation is observed; in thicker films, shear plasticity is observed. Simulations of the stress induced beneath the indenter tip shows that the preferred deformation mode depends on the relative spatial distributions of shear and hydrostatic stresses beneath the tip: if the shear stress in the film is high, it will deform by shear plasticity, whereas if the shear stress is low, it will deform by pressure-induced phase transformation. This is dependent on film thickness and tip geometry, offering the prospect of engineering the desired response using tips of different radii.

6.2 Experimental and Modelling Procedures

The samples investigated were thin films of pure Ge, epitaxially grown on Si (100) substrates by molecular-beam epitaxy (MBE). Samples with various film thicknesses were

investigated: 50 nm, 100 nm, 200 nm, 400 nm and 600 nm. All films were thicker than the critical thickness for strain relaxation, [133] that is they all contain misfit dislocations.

Films were indented with the UMIS-2000 indenter using a spherical tip of radius 4.3 μm, with maximum loads up to 100 mN. Indents were made in a single cycle with no hold period, with loading rates of 0.4-0.7 mN·s^{-1} and unloading rates of 0.5-0.8 mN·s^{-1}. Additionally, tests were performed in which the the load was partially released after each loading increment (load-partial unload), in order to determine the point of plastic yield.

After indentation, the samples were examined by Raman microspectroscopy. A Dilor Super LabRam was used, operating with a He-Ne laser ($\lambda = 632.8$ nm) with a spot radius of ~ 1 μm. The laser power was kept below 100 μW to avoid annealing metastable phases of Ge. Indent morphology was examined using a Hitachi S4500 FESEM operating at 3 kV in secondary-electron mode. In some cases, the sample was tilted at $45°$ to increase feature contrast.

Cross-sections for TEM were prepared either with the dual-beam (FEI xT Nova Nanolab 200) or single-beam (FEI xP 200) focussed-ion beam (FIB) system. In both cases, the FIB was used to deposit a protective platinum layer over the indent prior to cross-sectioning. The thinnest films (50 nm and 100 nm) were additionally coated with a protective layer of gold by evaporative deposition before insertion into the FIB.

To simulate elastic deformation under the indenter, the Elastica software package was used (ASMEC, Germany), which allows contact-induced elastic stresses in thin film-substrate systems to be calculated. Stress distributions were obtained for Ge films on Si indented by a 4.3 μm radius spherical diamond indenter, with Ge layer thicknesses ranging from 10 nm to 600 nm. Young's moduli of 132 GPa and 163 GPa and Poisson's ratios of 0.21 and 0.22 were used for Ge and Si, respectively. [134] (Anisotropy of the mechanical properties was not considered.)

Elastica allows the applied load required for 'failure' (transition from elastic to elastic-plastic deformation) to be calculated, both for failure by shear yield (ie twinning and dislocation slip) and failure by hydrostatic yield (i.e. high-pressure phase transformation). Yield, or permanent deformation, occurs when the stress exceeds some critical yield value. The pressure for the β-tin phase transformation from DAC experiments was used for the hydrostatic yield stress: this pressure is ~ 10.6 GPa for Ge and ~ 12.5 GPa for Si. [9,10] (The effect of shear stress, which lowers the transition point, [9] was not included.) For the shear yield stress, a value of 6.8 GPa was used for Ge. This was calculated as the stress required for significant plastic flow during indentation of bulk Ge, corresponding to the point of departure from elastic behaviour in a load-50% partial unload test. The load P_c and depth h_c were measured from P-h data, as shown in Fig. 6.1. The stress for full flow was then calculated according to Field and Swain's analysis as $3 \times Y_c = \frac{P_c}{\pi h_c R}$,

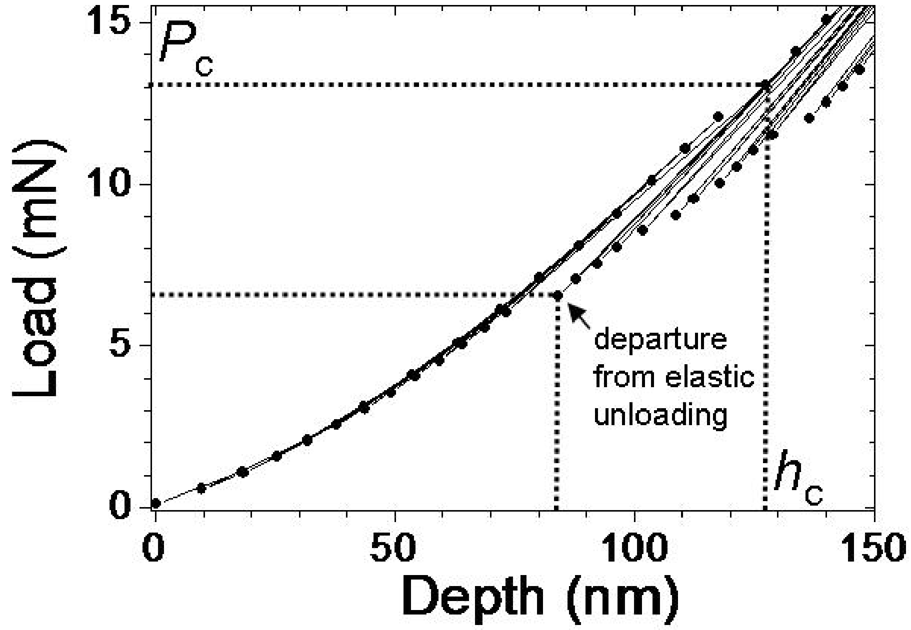

Figure 6.1: Load-50% partial unload P-h curve for bulk Ge, showing departure from elastic response at yield load P_c.

where R is the tip radius. It was assumed that yield by shear in the Si substrate would not occur, because Si is experimentally observed to deform by phase transformation under these loading conditions. [22, 23]

6.3 Results

Raman spectra illustrate the trend of phase transformation in the Ge film with film thickness and applied maximum load. Results for indents in the 50 nm, 100 nm, and 200 nm film samples are shown in Fig. 6.2. Spectra from unindented regions of the films feature a single peak at 301 cm^{-1} characteristic of Ge-I (diamond-cubic). For the two thinner films an additional peak is visible at 521 cm^{-1} corresponding to the Si-I substrate.

The penetration depth of the Raman laser, d_p, defined as the depth at which 90% of the signal is attenuated, is given by the expression $d_p \simeq 1.15/\alpha$, where α is the photoabsorption coefficient. [64] For Ge at $\lambda = 632.8$ nm, $d_p \simeq 80$ nm. [135] Accordingly, the Si-I peak is just visible through the 100 nm film [Fig. 6.2(b)].

Several indents were examined for each load and film thickness. For the indents in the 50 nm film sample [Fig. 6.2(a)], a broad band is visible between 200 and 300 cm^{-1},

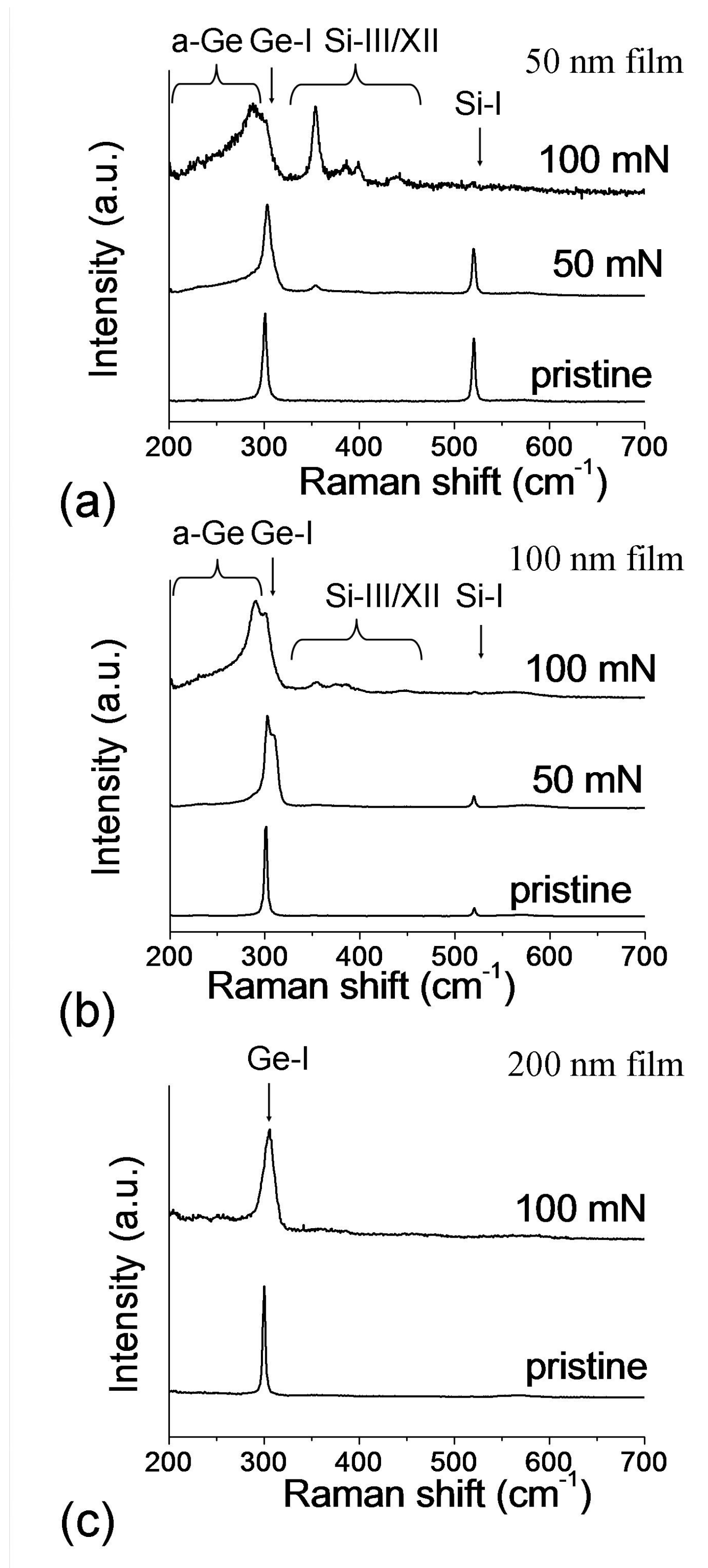

Figure 6.2: Raman spectra for indents in thin film samples: (a) 50 nm film, (b) 100 nm film, and (c) 200 nm film.

corresponding to amorphous Ge (a-Ge). [136] Additional peaks at 354, 387, 399 and 437 cm^{-1} correspond to the Si-III (bc-8) and Si-XII (r-8) metastable phases. [21] These phases form from the Si-II phase on pressure release. [137] These features are much more pronounced for the 100 mN load than for the 50 mN case, indicating more extensive transformation. For the 100 nm film sample [Fig. 6.2(b)], the spectrum corresponding to the 100 mN load shows the phases a-Ge, Si-III and Si-XII, although to a lesser extent than for the 50 nm film; the spectrum corresponding to a 50 mN maximum load shows no signs of phase transformation. Finally, for the 200 nm sample and for thicker films, no indication of phase transformation was found in Raman spectra for any maximum load, only broadening and shifting of the Ge-I peak, attributable to residual compressive stresses. [27]

XTEM micrographs show the extent of phase transformation in more detail. Figs. 6.3, 6.4 and 6.5 show micrographs of indents in the 50 nm, 100 nm, and 200 nm films. Phase-transformed material can be observed in the Si and the Ge, as well as slip bands and possibly dislocation tangles beneath the transformed zone in the Si, as indicated in each figure. In the Si substrate there is a hemispherical transformed zone of Si-III/Si-XII (confirmed by selected area diffraction); the volume of transformed Si decreases with increasing film thickness, attributable to the reduced hydrostatic stress in the Si film. The indented Ge films contain a-Ge with small grains of polycrystalline Ge-I. In the enlarged images, it can be seen that the transformed regions of the Ge, distinguishable by lighter contrast, stop short of the edge of the deformed impression. Each of the films is ruptured at the edges of the transformed regions. The 50 nm film is slightly uplifted on one side of the indent. For the 100 nm film and especially the 200 nm film, delamination has occurred, and the transformed Si has the appearance of having flowed to the surface.

Fig. 6.6 shows XTEM of an indent in the 400 nm film. A misfit dislocation caused by the lattice mismatch between Ge and Si is visible in the film on the left side of the image, indicative of the relaxed state of the film. No phase transformation, either in the Ge film or the Si substrate, is observed. Instead slip, twinning, and a high density of dislocations are present. The SADP from the central deformed region inside the Ge layer [Fig. 6.6(b) inset] features streaks and extra reflections indicative of twinning. The dark-field (DF) image [Fig. 6.6(b)] taken using the boxed twin reflection shows that the twin bands are concentrated in the Ge layer; most of the twins halt at the Ge-Si interface, but some cross the interface and extend into the Si.

Plan view SEM micrographs of indents show the trend of fracture with film thickness. Fig. 6.7 shows SEM micrographs corresponding to 100 mN loads in 50 nm, 100 nm, and 200 nm films. There is no visible cracking around the indent in the 50 nm film; there is slight cracking and uplift on one side of the indent in the 100 nm film; and for the 200

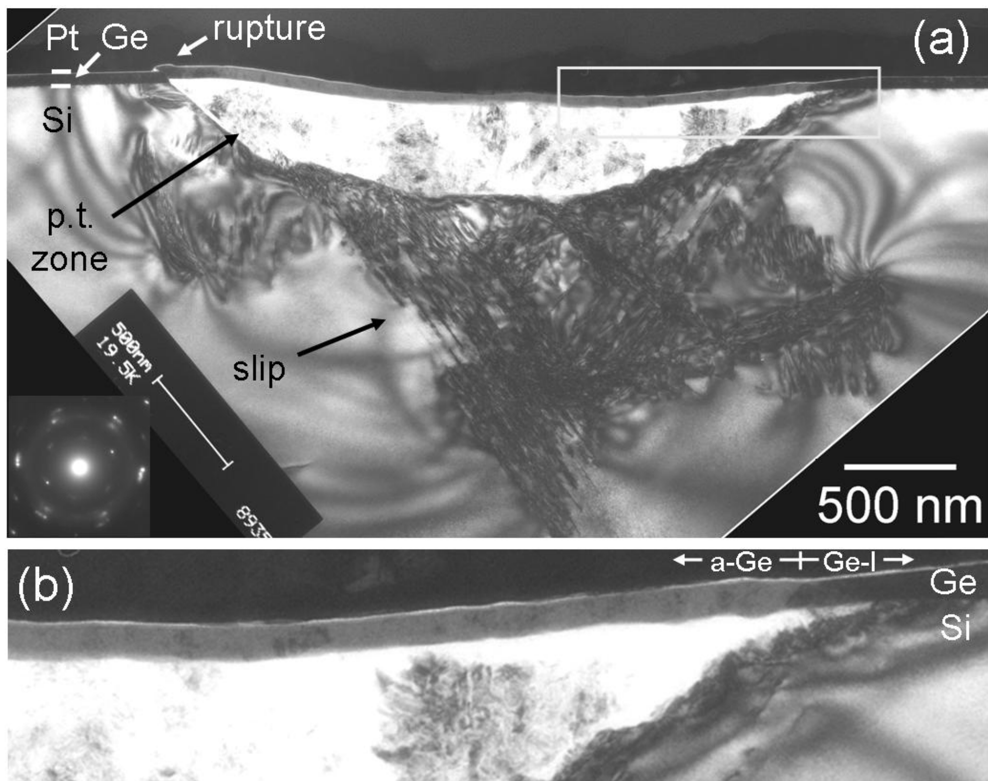

Figure 6.3: XTEM micrograph of 100 mN indent in 50 nm thin film Ge on Si sample, (a) whole indent and (b) close-up of film. Inset: selected area diffraction pattern (SADP) from transformed region (Si and Ge).

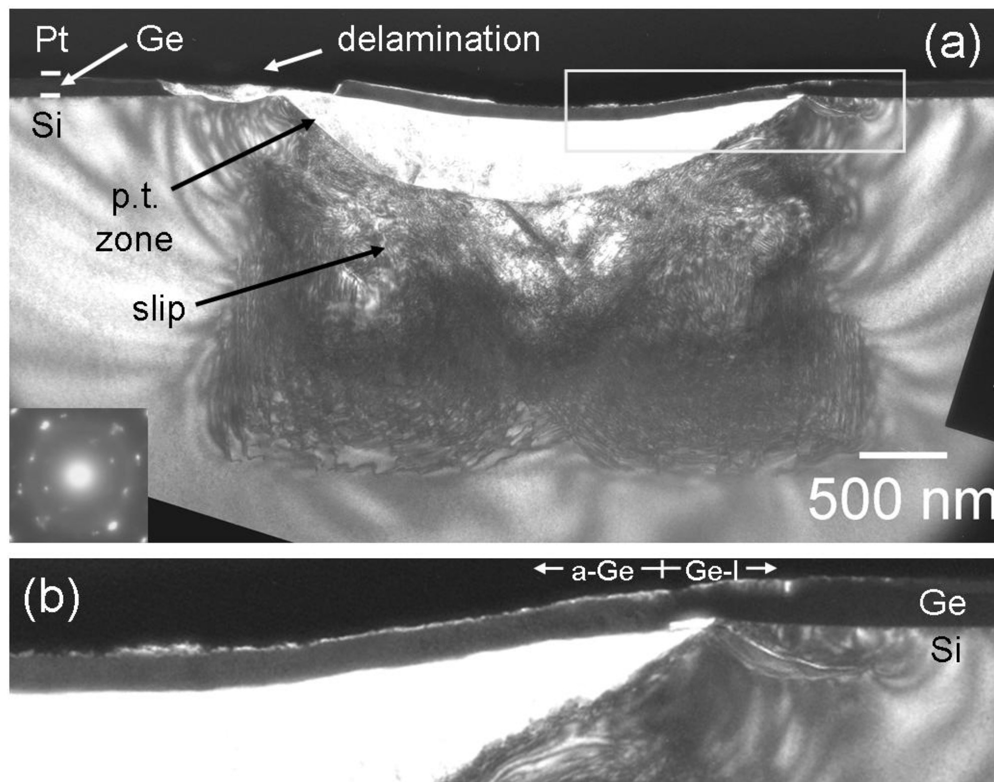

Figure 6.4: XTEM micrograph of 100 mN indent in 100 nm thin film Ge on Si sample, (a) whole indent and (b) close-up of film, with SADP inset.

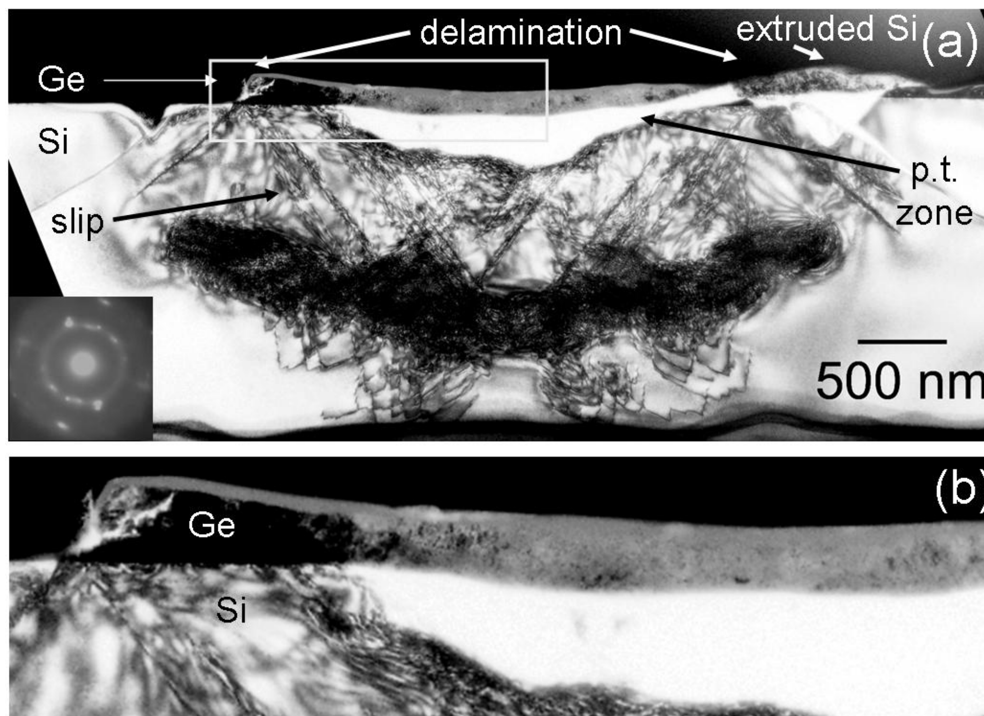

Figure 6.5: XTEM micrograph of 100 mN indent in 200 nm thin film Ge on Si sample, (a) whole indent and (b) close-up of film, with SADP inset.

nm film, there is a pronounced lateral spall adjacent to the indent. Interestingly, the spall itself is fractured. Indents to a load of 100 mN in 400 nm and 600 nm films (not shown) primarily featured radial cracking, characteristic of bulk Ge. [138] The internal structure of the indents in Fig. 6.7 is also notable. A mottled, rough region can be seen within each indent; the region is largest for the 50 nm film and smallest for the 200 nm film. The mottled appearance is suggestive of a phase transformation. [139]

P-h results for all Ge-Si samples showed similar maximum penetration and elastic recovery, but differed significantly in terms of qualitative features of the curve, most notably the tendency for pop-out to occur. Fig. 6.8 shows P-h curves from indents to both 50 mN and 100 mN loads for the 50 nm, 100 nm, 200 nm, and 400 nm films. For the 50 nm film, a pop-out was observed for both maximum loads. Likewise, tests in the 100 nm film tended to feature a pop-out at both maximum loads, although tests to 50 mN in this film occasionally featured an elbow instead (about 14% of tests). For the thicker films, pop-out becomes harder to induce: the 200 nm film sample only showed a pop-out when loaded to 100 mN, and the 400 nm and 600 nm samples showed no pop-out for any maximum load. The position of the pop-out event was determined by taking the derivative of the P-h curve, as illustrated in Fig. 6.9. For 100 mN tests, the pop-out occurred at an average load of 37 ± 4 mN and 34 ± 5 mN for the 50 nm and 100 nm films respectively.

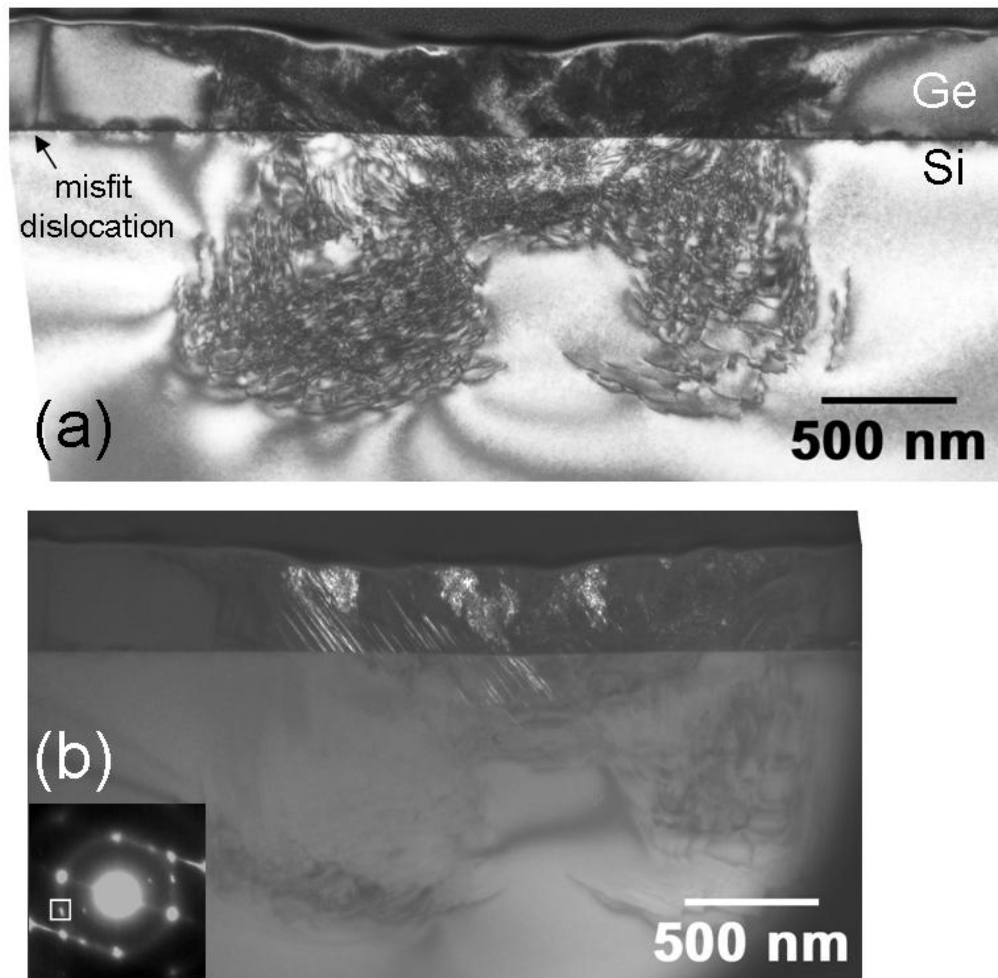

Figure 6.6: XTEM of 100 mN indent in 400 nm Ge film on Si. (a) Bright-field (BF) image, showing twinning and punched-out dislocations. (b) Dark-field (DF) image taken using the boxed reflection in the inset diffraction pattern, showing twins.

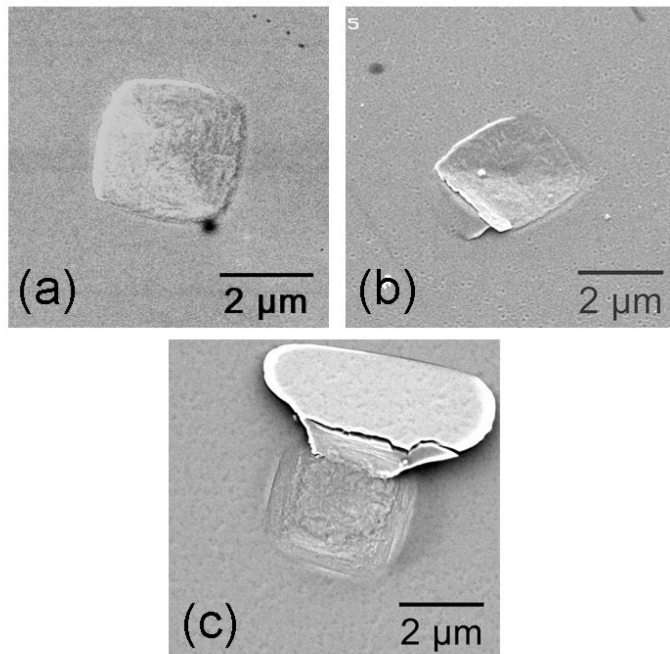

Figure 6.7: SEM micrographs of 100 mN indents in thin film Ge on Si samples. (a) 50 nm film. (b) 100 nm film. (c) 200 nm film.

For the 200 nm film, pop-out occurred at an average load of 24 ± 8 mN. Additionally, for the thicker films, pop-ins occurred on loading. Multiple pop-ins occurred above 60 mN for the 200 nm and 400 nm samples, and at 15 mN and above for the 600 nm sample (not shown).

To understand the dependence of the preferred deformation mechanism on film thickness, hydrostatic stress and von Mises (shear) stress distributions were calculated with Elastica. Figs. 6.10(a-d) show stresses for the 4.3 μm tip at a load of 12 mN (the approximate yield point as determined from load partial-unload experiments). Figs. 6.10(a) and 6.10(b) show stresses in the 50 nm film, and Figs. 6.10(c) and 6.10(d) show stresses in the 400 nm film. It is apparent that, for both films, the maximum hydrostatic stress is located at the surface in the Ge layer and directly beneath the indenter. By contrast, the maxima for the von Mises stress are located below the surface at a depth of ~ 300 nm: roughly half the contact radius, as would be expected for a non-layered bulk material. [39] For the 50 nm film, this places the shear stress maximum in the Si substrate; for the 400 nm film, the shear stress maximum lies within the Ge film itself.

In Fig. 6.10(g), load at plastic yield is plotted as a function of Ge film thickness for each of the two possible failure modes, shear and hydrostatic, as calculated with Elastica for the 4.3 μm tip. The load for hydrostatic failure (i.e., phase transformation) is roughly independent of film thickness. The load for shear yield, by contrast, drops as

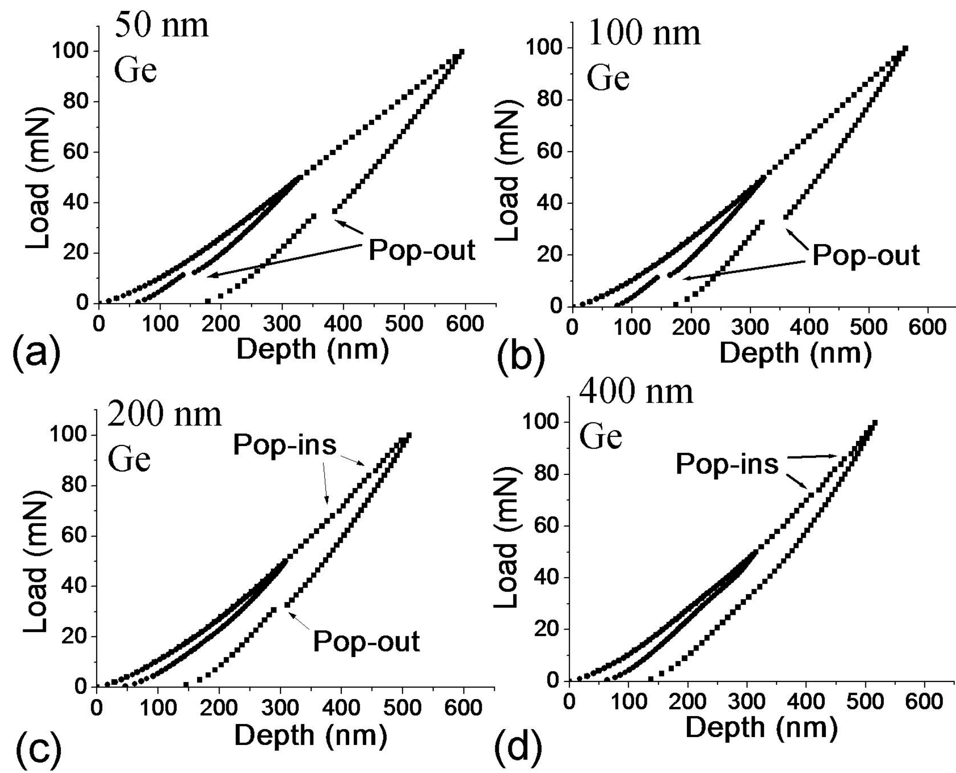

Figure 6.8: P-h curves to 50 mN and 100 mN in thin Ge films on Si. (a) 50 nm film, (b) 100 nm film, (c) 200 nm film, and (d) 400 nm film.

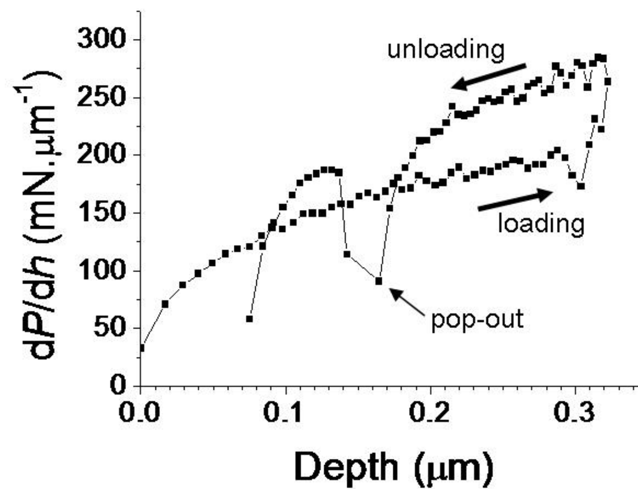

Figure 6.9: Derivative of 100 mN P-h curve in Fig. 6.8(b), plotted versus depth.

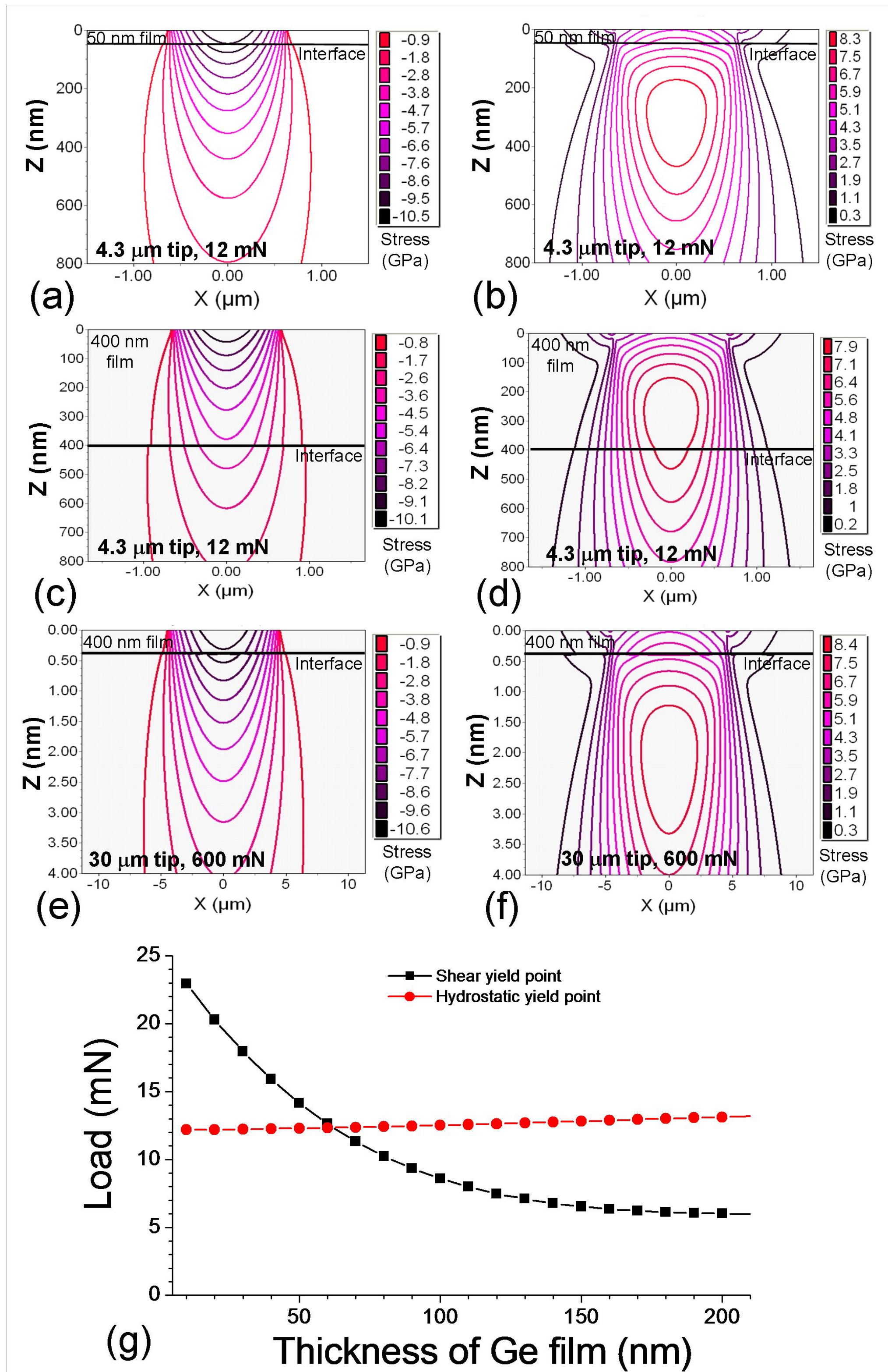

Figure 6.10: Isobaric plots of (a), (c), (e) hydrostatic stress and (b), (d), (f) von Mises stress (shear stress) beneath a spherical indenter, for different combinations of tip radius, film thickness, and applied load. (g) Shear yield point and hydrostatic yield point plotted as a function of Ge film thickness, for the 4.3 μm tip.

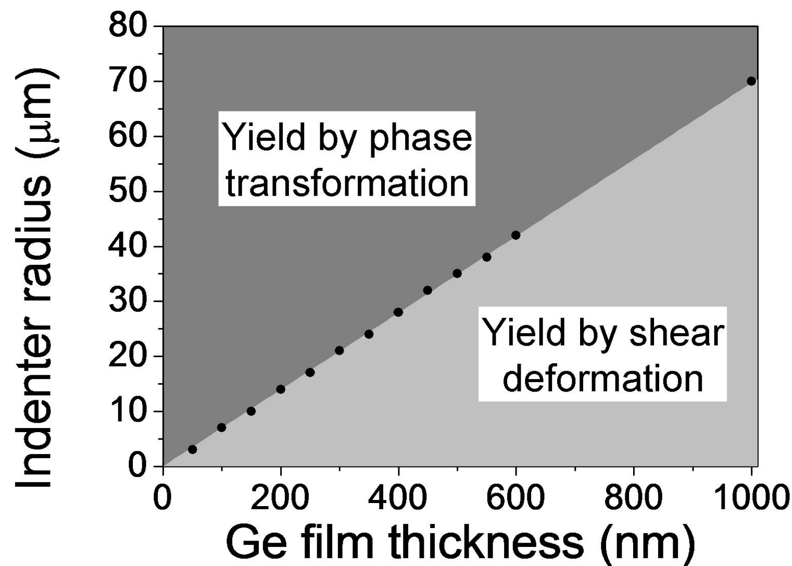

Figure 6.11: Deformation mechanism diagram, showing dominant initial deformation mechanism in Ge films on Si as a function of indenter tip radius and Ge film radius. Circles show critical transition points obtained from Elastica simulations. The boundary between the two regions is given by the relationship $R_c \approx 70h_f$.

film thickness increases. This analysis predicts that initial failure in Ge on Si films will take place by high-pressure phase transformation for films thinner than ~ 60 nm, and by shear-induced plasticity for thicker films. Note that this analysis only looks at elastic stresses and thus only applies to initial yielding, not to later stages of deformation.

Simulations with Elastica were conducted to find the critical indenter tip radius, above which phase transformation becomes dominant at a given film thickness, for various film thicknesses. Interestingly this relationship appeared to be linear: the critical tip radius is given by $R_c \approx 70h_f$, where R_c is tip radius and h_f is film thickness. A generalized plot of the dominant initial deformation mechanism as a function of indenter radius and Ge film thickness is shown in Fig. 6.11. For a 30 μm radius indenter on a 400 nm Ge film, a combination which lies in the 'yield by phase transformation' region, the stress states are shown in Figs. 6.10(e) and 6.10(f). As expected, the shear stress maximum is located in the underlying Si.

6.4 Discussion

Before turning to the behavior of the Ge films, the shear damage observed in the Si layer will be discussed. In the TEM micrograph of Fig. 6.6(b), several of the twins in the 400 nm film cross the interface into the underlying Si. Mechanical twinning has previously been observed in Si after high-temperature indentation, [140] but not in Si indented at room temperature. Increased shear-induced damage is observed at a greater depth below the contact surface in the Si substrate, especially in samples with the thicker Ge films. The bright-field (BF) image in Fig. 6.6(b) shows a high density of extended defects, presumably dislocation tangles, in the Si below the Ge film, whilst Fig. 6.5(a) shows a buried band of defects (dislocations) in the Si beneath a 200 nm Ge film. This band below the 200 nm Ge film appears to have formed at the intersection of slip/twin bands on opposing $\{111\}$ planes. This band is strikingly similar to sub-indent dislocation bands observed in bulk crystalline Ge. [30]

Pressure-induced phase transformation is observed as the predominant deformation mechanism in bulk Si whereas twinning is not observed at all. [23, 141, 142] The critical shear stress that would be required for twin- and dislocation-mediated deformation must therefore be high, relative to the critical hydrostatic stress for phase transformation, and shear deformation is consequently energetically unfavorable in bulk Si. In the layered structures observed here, however, twin bands and extensive dislocation formation are observed in the Si layer. That is, shear deformation is an energetically favorable indentation response under some conditions. The only difference from the bulk Si case is the presence of the Ge layer: twin bands can nucleate in the Ge layer, cross the epitaxial interface, and propagate in Si. It is proposed, then, that the nucleation step is the relevant limitation to shear plasticity in Si under indentation, and the reason that phase transformation dominates in bulk crystalline Si. Indeed, Ogata *et al.* have noted that in general there is a very high energy barrier to the nucleation of a stable twin band, compared to the energy required for its subsequent growth. [143] Calculating the energetics of the relevant processes through detailed modelling would help to address this issue further.

The Raman spectra, TEM, and P-h curves above present a broad trend of increasing favorability of phase transformation as an indentation response, in both Ge and Si layers, with decreasing Ge film thickness. Phase transformation occurs within the Ge layer for the 50 nm film and at higher loads for the 100 nm film. Phase transformation occurs in the Si substrate beneath the 50 nm, 100 nm, and 200 nm films. Twinning and dislocation activity become more pronounced with increasing Ge film thickness; for the 400 nm film sample, deformation occurs entirely by shear processes.

In the Si substrate, Raman and TEM show that the transformed phases in the Si are

Si-III and Si-XII, both products of the metallic Si-II phase on unloading. [12,16] It can be concluded therefore that the phase transformation in the Si is a pressure-induced transition to the high-density Si-II phase under load, resulting in the formation of the observed metastable phases on load release. The Ge phase transformation does not allow such unambiguous attribution, because in both Raman and TEM only the a-Ge phase is observed, which has multiple formation pathways (see Chapters 7 and 8). The a-Ge could be the final result of a high-pressure phase transformation, but alternately it could be a 'collapse' of the crystal structure due to a high density of defects, as is observed for ion implantation. [60] That is, the Ge could be transforming to metallic Ge-II under load, and then to a-Ge on unloading, or else it could be transforming directly from Ge-I to a-Ge at some point in the load cycle. The possibility of such a structural collapse during indentation has been explored previously. [138]

The simulated stress distributions in Fig. 6.10 shed some light on this question by showing the expected initial deformation mechanism as a function of Ge film thickness. During initial elastic deformation, the maximum hydrostatic stress occurs at the surface; the maximum shear (von Mises) stress occurs beneath the surface, at a depth of approximately half the contact radius. [39] This situation is not significantly modified by the layered structure and consequent change in stiffness at the interface. Thus, for films with a thickness much less than the contact radius at the onset of inelastic deformation, the shear stress within the film itself is low. Deformation in Ge will occur by the hydrostatic stress-induced metallic phase transformation. From the diagram in Fig. 6.11, the 50 nm film lies within this regime.

For thicker films, the shear stress maximum at onset lies within the film. Inelastic deformation occurs by shear-induced slip and twinning, the favored mechanisms in bulk crystalline Ge. [30, 138] The experimental results indicate that loading conditions also affect the deformation behavior: for the 100 nm film, phase transformation is favored (or forced) at higher loads. This may be due to pile-up of shear defects at the Ge-Si interface. Either this pile-up causes work hardening, increasing the hydrostatic stress such that phase transformation becomes favorable; or else the increased density of defects triggers the above-mentioned 'collapse' to the amorphous phase.

The final phase in the Ge films differs from that in the Si substrate. Whereas the metastable crystalline Si-III and Si-XII phases are observed in the substrate, in the films only a-Ge is observed. This differs from the DAC case, where Ge-II transforms into crystalline Ge-III on pressure release. A possible explanation is that the small volume of transformed material prevents the nucleation of the crystalline phase upon load release.

The trend in fracture behavior with film thickness is now considered. For the 50 nm film, negligible cracking is observed for indents up to a load of 100 mN. This may be the

effect of the phase transformation and accompanying densification, which diminishes the crack-driving residual plastic stress field. [49] For the 100 nm and 200 nm films, lateral cracking and delamination occurs, well below the minimum load for lateral cracking in bulk Ge for this tip geometry. [138] The SEM (Fig. 6.7) and TEM (Figs. 6.3, 6.4 and 6.5) results show that for indents in these films, there is a region at the outer edge of the impression where the Si has phase-transformed, but the overlying Ge has not. This would create a tensile stress in the Ge film on loading that may have generated a crack through the Ge layer and contribute to lateral cracking upon unloading. (Xie *et al.* have observed such cracks through TiN films on various substrates.) [144] Additionally, the downward force of the indenter promotes flow in the metallic-like transformed Si-II, and it appears [in Figs. 6.7(b) and 6.7(c)] that the transformed Si has been forced to the surface, rupturing the still-brittle Ge. For the 400 nm and 600 nm films radial cracking is observed, characteristic of monolithic Ge at these loads, [138] indicating that the substrate has a minimal effect on the fracture behavior.

6.5 Concluding remarks

The deformation response of thin films of crystalline Ge on Si subjected to nanoindentation is determined by film thickness, maximum indentation load, and indenter shape. Films that are significantly thinner than the depth of the shear stress maximum as determined by the tip geometry will deform by high-pressure phase transformation. The evidence suggests that this transformation occurs in both the Ge film and the underlying Si. Thicker films will deform via shear-induced twinning and dislocation slip, similar to bulk Ge. This has implications for machining and handling: thin films that phase transform will behave in a more ductile manner, with less tendency to fracture. At the inelastic yield point, the depth of the shear stress maximum is proportional to the radius of the circle of contact. The contact radius is determined by the indenter radius, implying that indenter shape can be used as a means of tailoring the response of a given film.

Not only does the Si substrate affect the deformation response of the overlying Ge, but for thicker films, shear defects from the Ge film propagate into the Si. These shear defects include twins, which are not normally observed in Si indented at room temperature, and a greater density of extended defect clusters, presumably dislocations, than is normally observed. This suggests that shear defects such as twins and dislocations may readily propagate in Si if nucleated in Ge, although they are difficult to nucleate in Si itself.

Finally, it is noted that a densifying phase transformation under high hydrostatic pressure is observed in a wide class of materials, not only in Ge and Si. [79, 145] On this basis it is possible that other materials that in bulk form deform under indentation by shear plas-

ticity would instead deform by phase transformation in thin film form, when the substrate is sufficiently hard and the film sufficiently thin relative to the radius of the indenting tip. This may be a novel means of inducing high-pressure phase transformations at room temperature in a wide range of materials, particularly in compound semiconductors.

CHAPTER 7

Giant pop-ins in Ge and Si

7.1 Introduction

At higher applied loads, fracture becomes a significant deformation response during indentation. Fracture is an important consideration in brittle materials such as Ge. Contact-induced fracture may create flaw sites to initiate larger cracks. More severe contacts tend to generate particulate debris around the indent site. Such particulate debris has the potential, for example, to have highly adverse effects on MEMS device operation. [146–148]

Different crack geometries are observed during indentation. The radial/median crack geometry has been studied in the most detail, forming the basis for the indentation method of determining fracture toughness. [55] The lateral crack geometry has been studied in less detail, being regarded as a secondary crack system and less theoretically accessible. [56] However, lateral cracks are important as they are considered to play a key role in material removal during wear and erosion processes. [149]

This chapter explores a new type of fracture event during indentation, observed in Ge and related materials, dubbed a 'giant pop-in' because it is marked by a discontinuous depth extension or pop-in of very large magnitude (1 μm) and above in the indentation P-h curve. The occurrence of this event during the loading cycle of a test is accompanied by an 'elbowing' response in the unloading cycle, a pronounced decrease of the slope $\mathrm{d}P/\mathrm{d}h$. Both these P-h curve signatures will be shown to be intimately connected to lateral cracking. The giant pop-in is caused by expelled material, released by the spallation of a lateral crack or cracks during loading. The elbowing behaviour is an elastic bending response during unloading of plates of material adjacent to the indent detached from the bulk by lateral cracking, analogous to the deflection of a cantilever. Results will be shown and the micromechanics of these two processes will be explored in more detail.

7.2 Experimental details

Indents were made with the UMIS-2000 using a nominally spherical tip (R $\approx$ 4.3 μm) and using a Berkovich indenter. Highly polished wafers of single-crystal Ge (Wafer World, Florida, USA) and Si (Unisil Corp., California, USA) with (100) surfaces were indented. Additional indents were made in a fused silica sample. High maximum loads of up to 1 N were used. Most tests were conducted with load applied and released in a single continuous cycle with no hold period, at loading and unloading rates dP/d$h \approx$ 1.5 mN·s^{-1}. Some multiple-cycle tests were also conducted in which load was applied, released to zero, and re-applied to the maximum load without moving the tip, for a total of 5 cycles. Partial-unload tests were also performed in which load was released to 50% after each loading increment, in order to calculate contact pressure as a function of penetration depth. [45]

SEM was conducted to investigate the surface crack morphology around indents. Cross-sections of indents were prepared using the FIB for both SEM and TEM examination, to study sub-surface cracking and sub-surface phase transformation and plastic deformation.

Raman spectra were collected from the centres of indents. Raman spectra were generally taken at least several days after indentation, except where otherwise noted.

Because the particulate debris surrounding the indents was of interest, optical microscopy was performed to quantify the amount of debris around indents. Digital micrographs were captured with a Leica DM4000 M microscope and attached CCD camera, and analysed with ImageJ (NIH, USA). Debris particles showed up against the smooth surface in strong dark contrast. The procedure was as follows: an annular region 40 to 90 μm from the indent centre was selected, the outer radius limited by the size of the image and the inner radius chosen to exclude the indent itself. The rest of the image was discarded. After thresholding the image, the total area taken up by debris was measured using the particle analysis function. Indents used for debris analysis were created in an array with a 500 μm spacing on a clean sample.

7.3 Results and interpretation

7.3.1 Giant pop-ins in Ge

The evolution of qualitative features in the P-h curve for Ge with increasing maximum load was examined. As found in the previous studies (described in more detail in Chapter 1), [27, 28, 30, 139] indents in Ge with maximum loads of 50 and 100 mN featured multiple pop-ins on loading, each of 10-20 nm extension, and a featureless unloading curve,

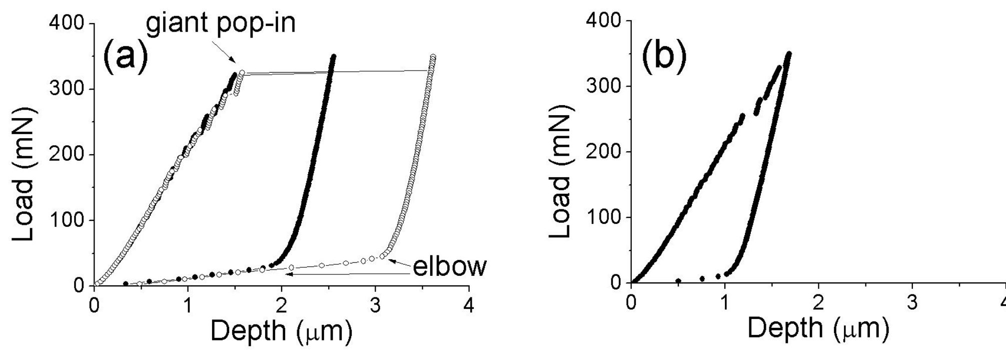

Figure 7.1: (a,b) Force-displacement curves for 350 mN indents in Ge, created using identical test parameters. Curves in (a) feature a giant pop-in event. Curve in (b) features only small pop-ins.

similar to Fig. 7.1(b). With increasing load, more pop-ins were found to occur, increasing somewhat in size (up to ∼50 nm) at higher loads.

When Ge was loaded beyond 200 mN with the spherical tip, a pop-in of very large magnitude (>1 μm) was sometimes found to occur. The load at which it occurred varied. Typical examples of the giant pop-in event are shown for 350 mN indents in Fig. 7.1(a). Indents that featured a giant pop-in consistently also featured a pronounced elbow on unloading, as indicated in Fig. 7.1(a). The larger the pop-in, the higher the load at which elbowing initiated. A force-displacement curve for an indent made under identical test conditions, that did not feature a giant pop-in, is shown for comparison in Fig. 7.1(b).

Several P-h curves to maximum loads of 500 mN in Ge are shown in Fig. 7.2. At these loads the curves all feature giant pop-ins, indicated by the near-horizontal traces in the plots. The magnitudes of the displacement increments range up to $\sim$ 5 μm under the loading conditions shown. The loads at which pop-in first occurs, and the resulting displacements, vary considerably from test to test, indicating some stochastics in the pop-in micromechanics. The slope of the elbow region in the unload curve is consistent for all tests, despite the variation in the size of the giant pop-in.

A statistical analysis of the giant pop-in event was conducted using 400 P-h curves from 500 mN load spherical indents made with 125 loading increments and 10 unloading increments. Of the indents examined, 95% featured a giant pop-in, defined as an extension greater than 600 nm. (Approximately 29% of the indents featured 2 or 3 giant pop-ins: in that event, only the first was used in the analysis.) Histograms of the load at which the giant pop-in was observed and its magnitude are shown in Fig. 7.3. The average load at which the giant pop-in occurred was ∼340 mN; the average magnitude of the pop-in was ∼2.0 μm.

To compare indents with, and without, a giant pop-in, statistical analysis was also

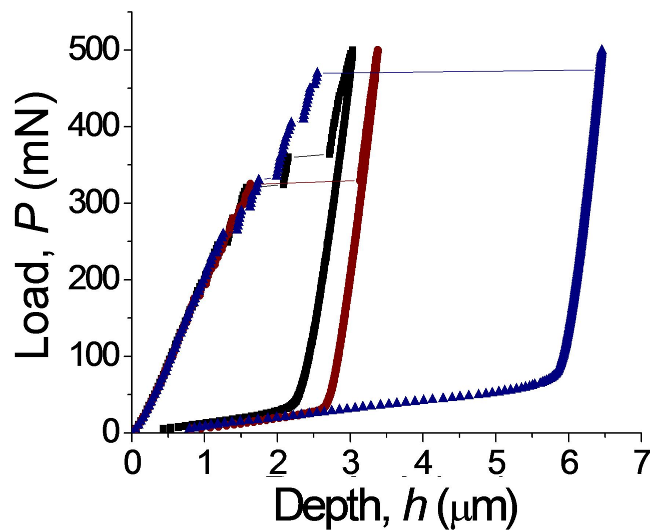

Figure 7.2: P-h curves for Ge to 500 mN.

performed on 350 mN load spherical indents made with 100 loading and 100 unloading increments. Because only $\sim 50\%$ of the indents featured a giant pop-in, there was considerable variation in the maximum depth at full load. The maximum depth correlated closely with the giant pop-in size ($R^2 = 0.96$). Because of elbowing, however, the final depth on complete unloading showed markedly less variation than the maximum depth. Moreover, there was minimal correlation between the final depth and the maximum depth ($R^2 = 0.08$).

Typical contact pressure results by the partial unload method [45] are shown in Fig. 7.4. The contact pressure prior to the giant pop-in is not constant; rather, it tends to

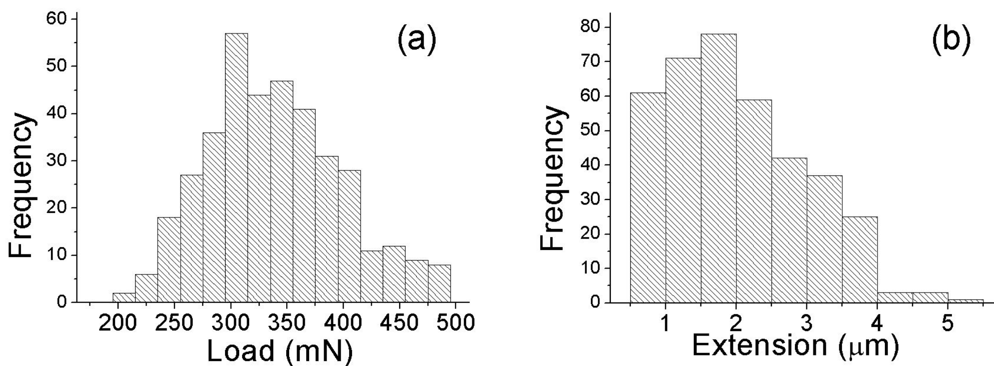

Figure 7.3: Histograms of (a) the load at which the giant pop-in occurs, and (b) the magnitude of the giant pop-in for 400 indents made with a spherical tip of radius 4.3 μm loaded to 500 mN.

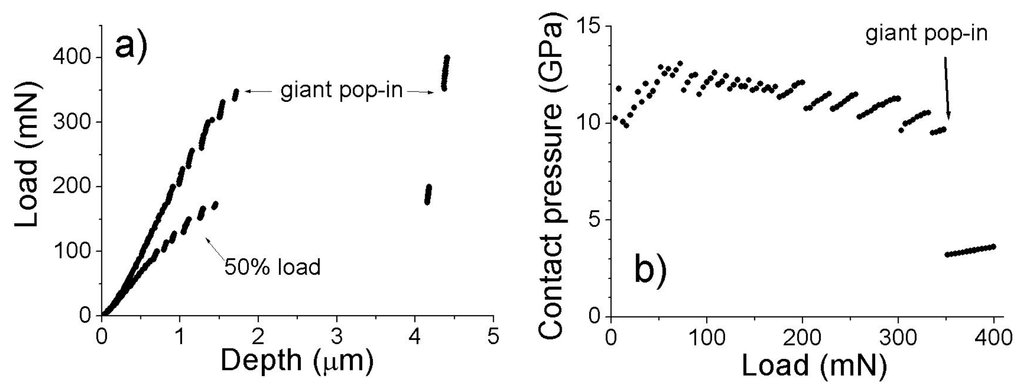

Figure 7.4: Partial unload results for Ge. (a) Force-displacement data. (b) Contact pressure as a function of load, calculated by Field and Swain method. [45]

increase steadily until a small pop-in occurs, at which point it drops to a lower value. The giant pop-in occurs, in this case, at a contact pressure of $\sim$ 9.7 GPa; after the giant pop-in, the pressure decreases dramatically. It should be noted that the indenter used in the study is only spherical to a contact depth of $\sim$ 1.5 μm; beyond this depth, the Field and Swain analysis will no longer be quantitatively accurate, but does give a comparative idea of the contact pressure.

Indents made with the Berkovich tip showed multiple small pop-ins. Berkovich indents made to loads of 300-500 mN did not feature a giant pop-in, but one was sometimes observed at loads upwards of 800 mN. When a giant pop-in occurred it was always accompanied by elbowing on unloading. Berkovich tests without a giant pop-in showed a featureless unloading curve.

The development of surface cracking for spherical indents was investigated by examining residual indents of a range of maximum loads using optical microscopy and SEM. Indents to 50 mN showed no surface indications of cracking. Indents of maximum load 100 mN and above featured surface traces of radial/median cracking. At loads of 150 and 200 mN, some indents showed wing-like features indicative of lateral cracking; at maximum loads of 250 mN and above, lateral cracking was observed around all indents (with or without a giant pop-in).

For loads sufficient for a giant pop-in to occur, indents featured pronounced radial and lateral cracking, as can be seen for the 350 mN indents in Fig. 7.5. The indent in Fig. 7.5(a) underwent a giant pop-in; the indent in Fig. 7.5(b) did not, under identical loading conditions. A number of 350 mN indents were examined by SEM. Whilst there was considerable variation in the surface morphology, no obvious marks distinguished indents with a giant pop-in from those without. Lateral cracking generally caused a thin sliver of material around the indent to be partially detached from the bulk, as indicated in Fig.

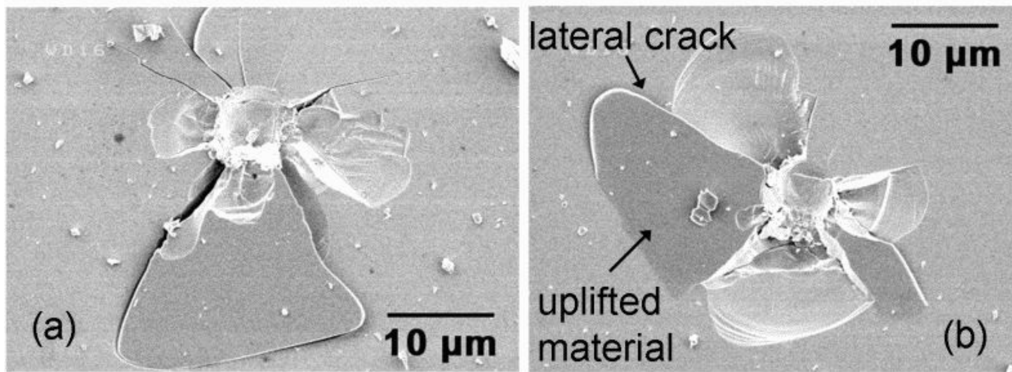

Figure 7.5: SEM images of 350 mN load indents: (a) one of the indents in Fig. 7.1(a) (giant pop-in) and (b) indent in Fig. 7.1(b) (no giant pop-in).

7.5(b).

7.3.2 Observational details and mechanisms of giant pop-in

A number of 350 mN indents, both with and without giant pop-in, were cross-sectioned and imaged with the dual-beam FIB microscope. Two examples are shown in Fig. 7.6. Directly beneath indents, extensive crack networks are visible. All indent cross-sections revealed large lateral cracks extending outwards from the central deformed region. The slivers of detached material above the lateral cracks are uplifted above the bulk surface (dotted line).

The cross-sections revealed that indents that had undergone a giant pop-in were significantly deeper than indents which had not. The indent in Figs. 7.6(c) is ∼3.2 μm deep, whereas the indent in 7.6(f) is only ∼0.6 μm deep. The cross-sectional profile is delineated by the boundary between the layer of deposited Pt (lighter) and the underlying Ge substrate (darker). The original level of the surface prior to indentation was extrapolated from the level of the undeformed material at the edges of the cross-section. The cross-sectional depth was measured from the original level of the surface to the base of the indent. Notably, the residual depth given by the force-displacement curve [Fig. 7.6(a)] of 0.46 μm is considerably less than the actual measured residual depth. In contrast, for the indent that did not undergo a giant pop-in, the measured depth in cross-section agrees with the residual depth from the force-displacement curve of 0.65 μm [Fig. 7.6(d)]. For the other indents examined, those that had undergone a giant pop-in featured a cross-sectional depth between 1 and 3 μm, markedly greater than that indicated by the force-displacement curve of ∼0.5 μm. For those with no giant pop-in, the cross-sectional depth was <1 μm,

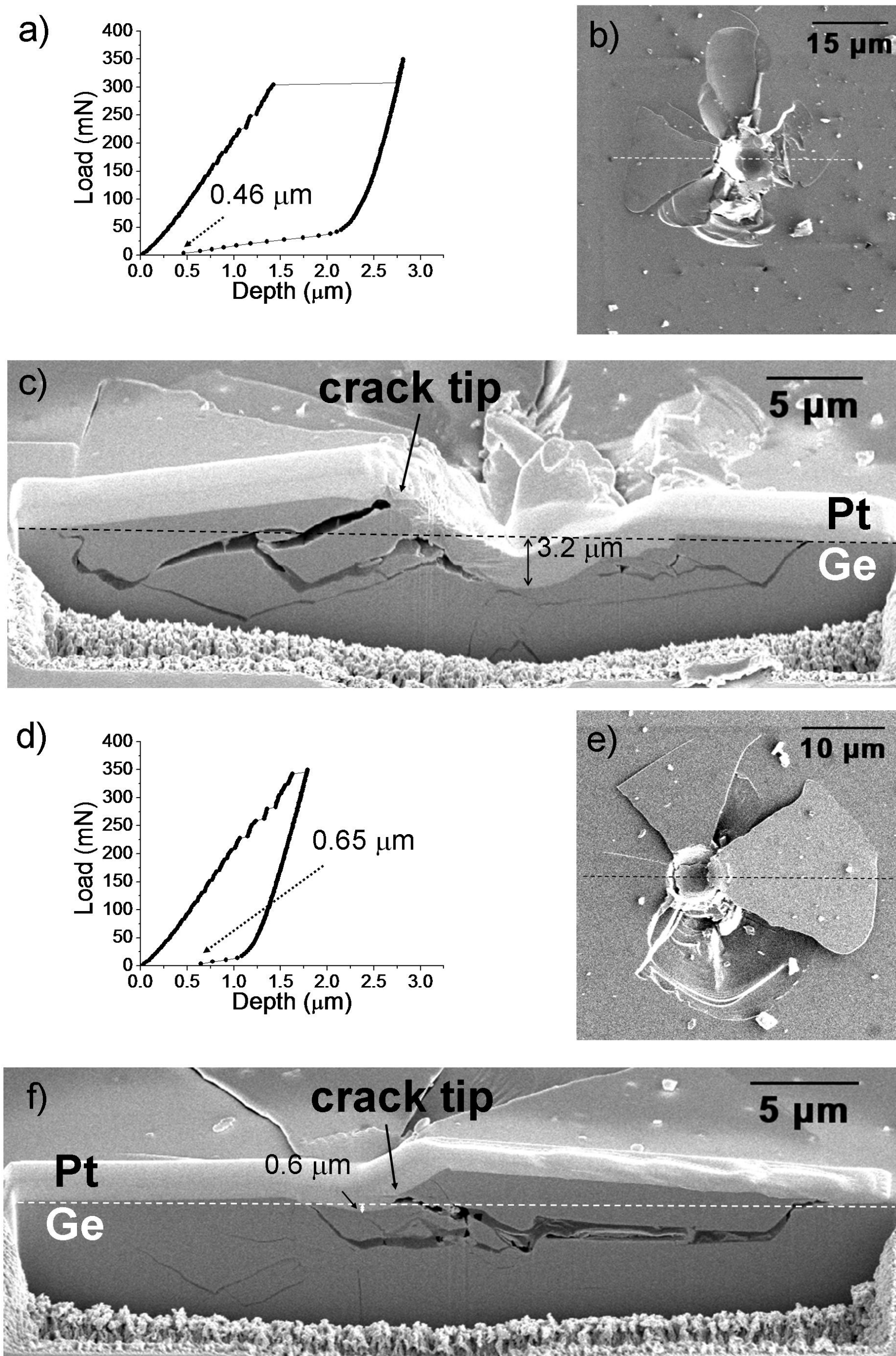

Figure 7.6: (a) Force-displacement curve for 350 mN Ge indent featuring giant pop-in. (b) FIB ion-beam image (prior to Pt deposition) of the indent. (c) FIB electron-beam cross-sectional image of indent (a). (d) Force-displacement curve for a 350 mN indent with no giant pop-in. (e) FIB ion-beam image of the indent. (f) FIB electron-beam cross-sectional image of indent (d).

and was in approximate agreement with the force-displacement curve depth at final unload.

Notably, indents with, and without, a giant pop-in differed in the location of the point where the near tip of the lateral crack meets the contact impression (labelled "crack tip"). In Fig. 7.6(c), for the lateral crack on the left, this point lies close to the edge of the contact impression. By contrast, in Fig. 7.6(f) the lateral crack meets the contact impression close to the base, well below the edge of the contact impression. Other indents examined in cross-section were similar: those with a giant pop-in featured a shallow-initiated lateral crack, while those without a giant pop-in featured only deep-initiated lateral cracks.

Giant pop-ins in Si

Further investigations found giant pop-ins to occur in Si, a closely related material to Ge. P-h curves are shown in Fig. 7.7(a) for maximum loads of 900 mN in Si. All of the curves feature giant displacement pop-ins. As with Ge, the loads at which pop-in first occurs, and the resulting displacements, vary considerably. Well-defined elbowing is again observed in the unloading portion of the curve.

Figs. 7.7(b) and 7.7(c) show top-surface and cross-section images of an indent in Si that has undergone a giant pop-in. Extensive cracking is apparent around the indentation site, with radial and lateral cracking. From the cross-section view, the lateral cracks initiate from the plastic zone, at depths somewhere between the top surface and the zone base. These cracks run approximately parallel to the top surface, in some cases propagating all the way upward to the surface to produce scallop-shaped chip segments confined within preceding radial cracks. [56] All indents in Si with giant pop-ins revealed one or more such segments, suggesting a correlation between spallation and displacement increment. Note debris particles around the indent in Fig. 7.7(b) (see arrows).

Debris analysis

In Ge, high load indents were surrounded by considerable amounts of scattered debris. Indents that had undergone a giant pop-in were surrounded by a greater quantity of debris. Example optical micrographs of 350 mN indents (with and without a giant pop-in) are shown in Fig. 7.8(a) and Fig. 7.8(b). The amount of debris was quantitatively measured, according to the method described in the Experimental Details section. A large number of indents were analysed in this way. For each indent, the total area of debris was compared with the size of the largest pop-in in the force-displacement curve (either a giant pop-in or a smaller pop-in). The results are shown in Fig. 7.9(a). The quantity of debris showed a clear correlation ($R^2 = 0.68$) with pop-in size.

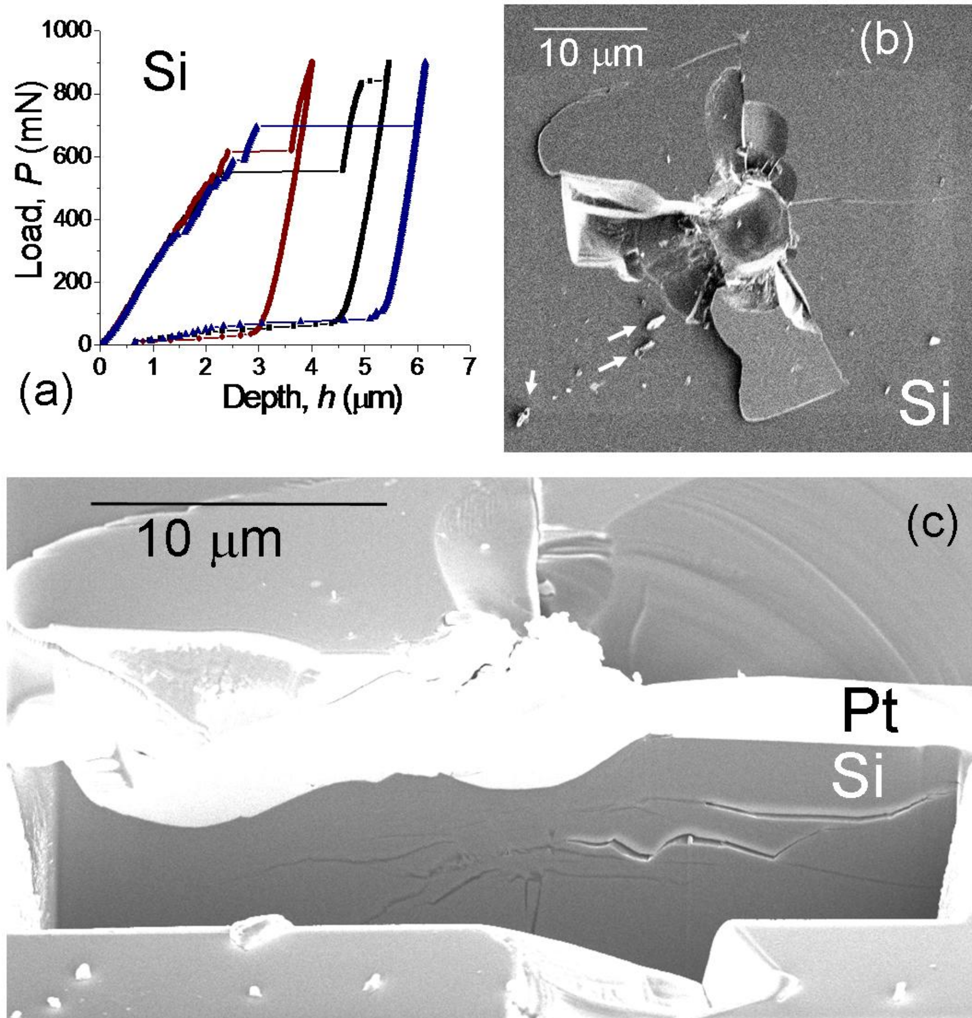

Figure 7.7: (a) P-h curves for Si to 900 mN. (b) Top-down and (c) cross-sectional FIB images of an indent in Si to 550 mN that has undergone a giant pop-in.

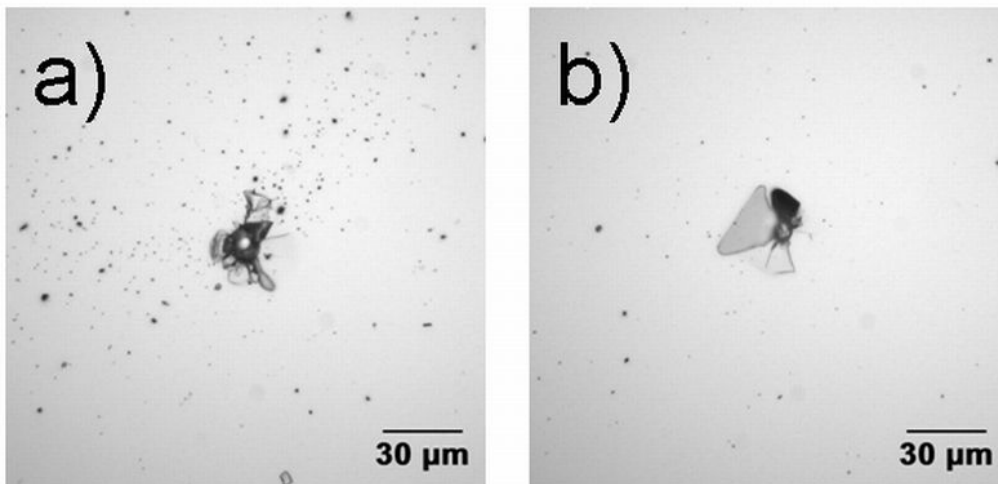

Figure 7.8: Optical micrographs of 350 mN indents: (a) with a large maximum pop-in (1.96 μm), (b) with a small maximum pop-in (0.17 μm).

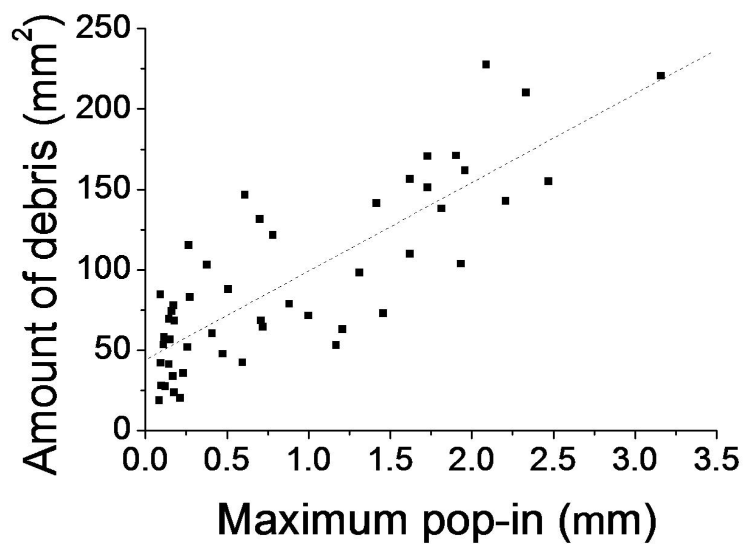

Figure 7.9: The amount of debris around 350 mN indents plotted against the size of the largest pop-in for the indent. The dotted line is a guide for the eye.

Material	H (GPa)	K_c (MPa m$^{1/2}$)	H/K_c (μm$^{-1/2}$)
Si	9	0.7	12.9
Ge	8	0.6	13.3

Table 7.1: Properties of Si and Ge, taken from Ref. [150].

To quantify the variation of the pop-in size with load, Fig. 7.10 plots pop-in displacement h_* as a function of corresponding critical indentation load P_* at which pop-in event takes place (Fig. 7.10 inset) for Si and Ge, obtained from large datasets of 400 indents for each material. Notwithstanding the scatter in data, there appear to be definable threshold loads, $P_C \approx 350 \pm 100$ N for Si and $P_C \approx 250 \pm 80$ N for Ge (vertical dashed lines), above which pop-ins occur. The pop-in displacements h_* show considerable variation, but are more or less bound by upper envelopes (solid lines). These envelopes are derived simplistically from the standard hardness relation $H = P_*/\pi a^2$, with a the contact radius, by equating the maximum displacement with the plastic zone depth to obtain $h_* \approx a_* = (P_*/\pi H)^{1/2}$, using H values from Table 7.1. Since H for Si and Ge are within 10% of each other, the predicted envelopes in Figs. 7.10(a) and 7.10(b) differ only slightly, although the data for Ge appear to fall closer to the envelopes than do those for Si. Mechanisms to explain such differences will be discussed in the following section.

Possible mechanisms for giant pop-in

The giant pop-in is clearly a dramatic damage event, in which the instantaneous indenter penetration frequently exceeds total elastic-plastic penetration. The pinning mechanism described for the smaller pop-ins is insufficient to account for its magnitude. Examining the force-displacement curve alone, in which the pop-in penetration is apparently recovered by elbowing on unloading, one might attribute the giant pop-in to a reversible mechanism. One such mechanism would be the sudden transformation of a large volume of material beneath the indenter tip in the case of Ge to metallic Ge-II, which is ~20 $\%$ more dense than Ge-I. [8] The transformation on unloading of Ge-II to a-Ge, which at ambient pressure is close in density to Ge-I, [151] would then account for the elbowing.

For a pop-in of 1–2 μm to occur by this mechanism, the transformation of a volume at least 5-10 μm deep would be required. Calculations of the Hertzian stress distributions beneath the tip at the loads of interest (300-400 mN) were made using the Elastica software package (ASMEC, Germany). The calculated hydrostatic pressure exceeded the threshold pressure for transformation (7-8 GPa [9]) to a depth of only about 2 μm. The analysis neglects plastic deformation, which would greatly lower the pressure further still. The giant pop-in therefore cannot be solely attributed to a sudden metallic phase change of a large volume of material in Ge.

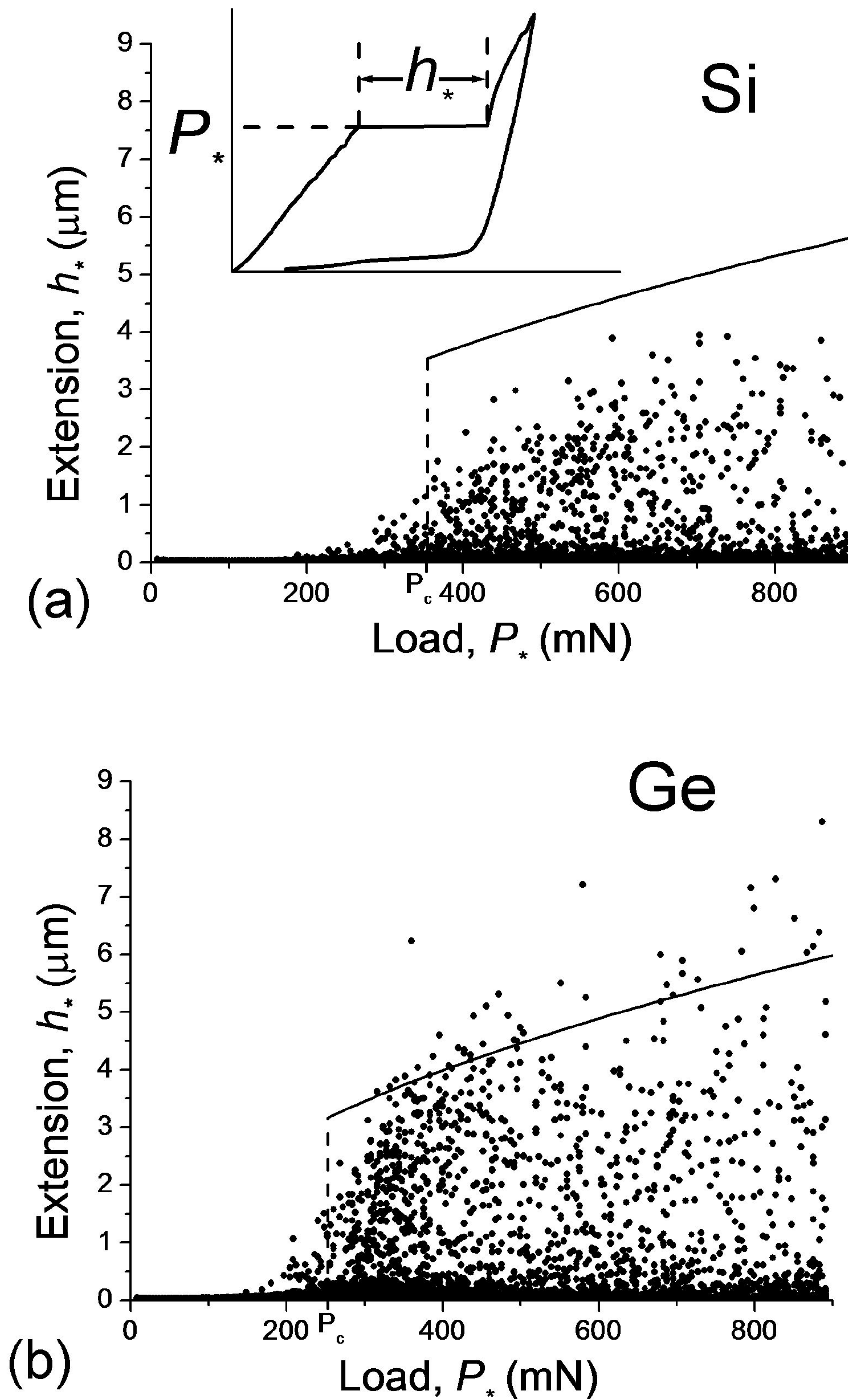

Figure 7.10: Pop-in size as a function of pop-in load for (a) Si and (b) Ge. Points are experimental data. The solid line is the indenter contact radius, calculated from $a_* = (P_*/\pi H)^{1/2}$. Inset: Schematic showing P_* and h_*.

Furthermore, cross-sectioning (Fig. 7.6) reveals that indents in both Ge and Si featuring a giant pop-in are markedly deeper than indents without a giant pop-in. This implies that the giant pop-in involves material removal. Quantities of scattered debris are observed around indents with a giant pop-in, the amount of debris correlating with the size of the pop-in. It is therefore reasonable to suppose that the material missing from the indent is the same material that is observed as debris. Thus it is proposed that the giant pop-in in the force-displacement curve is caused by material being ejected violently from the deformation zone beneath the indenter tip. The tip sinks into the space left by the removed material, causing the observed sudden increase in depth.

It is instructive to elaborate on the micromechanics of the envisioned pop-in process. Entering the plastic region, the indentation generates dislocated shear bands or flaws that act as precursors for lateral (and radial) cracks. The shear events are discrete at the submicron level and so become subject to statistical distributions at low contact loads. At higher loads, the spatial extent of the flaws increases, in proportion to the characteristic contact dimension a, without significantly increasing the stress intensity acting on these flaws (i.e., load-independent hardness). [51, 152] The depth of the ensuing lateral cracks that grow out of the flaws also scales with a, as indicated in the above derivation of the envelope curves in Fig. 7.10. Once a lateral crack intersects the surface it is on the verge of detachment, thus reducing the support on the indenter. In some cases the lateral cracks will initiate close to the base of the plastic zone, in others somewhere between the base and the top surface, depending on the stochastics. Hence the envelopes in Fig. 7.10 represent an upper bound and account for the wide scatter in data within those envelopes.

It remains to account for the small but seemingly significant differences observed in the critical threshold loads for Si and Ge. An earlier fracture mechanics analysis of radial cracks gives a simple relation for threshold load, $P_C \propto K_C^4/H^3$, with hardness H and toughness K_C given in Table 7.1. [51] This relation predicts a 30% higher value of P_C for Si than for Ge, which compares with a $\approx 40\%$ higher value in Fig. 7.10. Thus, allowing for the data scatter and the sensitivity of P_C to small variations in K_C and H in the threshold relation, the results appear to be consistent qualitatively and quantitatively with a lateral crack spallation model.

Much greater loads were required to initiate a giant pop-in when a Berkovich indenter was used, compared with spherical indentation. It is noted that for the Berkovich indenter the induced strain is approximately constant, whereas for the spherical tip the strain increases continuously with penetration depth, acting to promote cracking and thus favour the occurrence of the giant pop-in. Additionally, the sharp corners of the Berkovich indenter act as stress concentrators to induce radial/median cracking, [153] presumably at the expense of the lateral cracking which is responsible for the giant pop-in.

These results show that fractures associated with sharp-contact events can generate particulate debris. In MEMS devices, contact events that do not directly impact the working elements of a device may nevertheless generate debris that interferes with operation. [146–148] Shock [146] or vibration [148] loading during device operation could transport such debris to inter-element locations, causing mechanical jamming or electrical shorting. The single-contact induced fragments observed here are typically larger than the wear particles generated during operation of MEMS devices, [146, 148] where device failure is associated with material removal leading to a loss of element dimensional tolerance. In such cases the wear particles are a symptom, not a cause, of device failure. The observations here suggest that debris generation in brittle materials may be minimized by avoiding contact events above the threshold for giant pop-in and corresponding spallation.

The mechanism for elbowing

If the giant pop-in is due to physical removal of material, an inherently irreversible process, the task remains to explain the apparent depth recovery observed through elbowing. The shape of the force-displacement curve, post-elbowing (Fig. 7.2), indicates a highly linear response, with a much lower compliance than the bulk material. Such a response is expected from plates of material around the indent detached by lateral cracking. The detached plates can be modelled as loaded cantilevers. [56] Using a quarter-plate approximation for the crack configuration and assuming uniform crack length and depth, the stiffness of the plates, k, is given by: [56]

$$k = 4Eh^3/3c^2 \tag{7.1}$$

where E is the Young's modulus, h is the crack depth, and c is the crack length. Inserting a Young's modulus of 132 GPa, [134] and typical crack dimensions, measured from 350 mN indents, of $c = 17\mu$m and $h = 2.5\mu$m into Eq. 7.1, gives a stiffness of $k = 9.5$ mN.μm^{-1}. Given the simplifying geometrical assumptions made, this is in reasonable agreement with the measured stiffness which was $k = \mathrm{d}P/\mathrm{d}h \approx 16.6$mN.$\mu$m^{-1}.

It can be seen that even indents without a giant pop-in show some slight elbowing (e.g., Fig. 7.1(b)). The elbowing after the giant pop-in seems to be the same response, only initiating earlier on unloading (that is, at a higher load) and occurring to a much greater extent. Initially during unloading, depth recovery occurs by elastic relaxation in the bulk. Only when most of the bulk elastic strain is released will the compressive stresses diminish sufficiently for the crack to open. The removal of material during the giant pop-in releases a considerable amount of stored elastic strain energy. Consequently, after the giant pop-in, full bulk recovery is completed at an earlier stage of unloading.

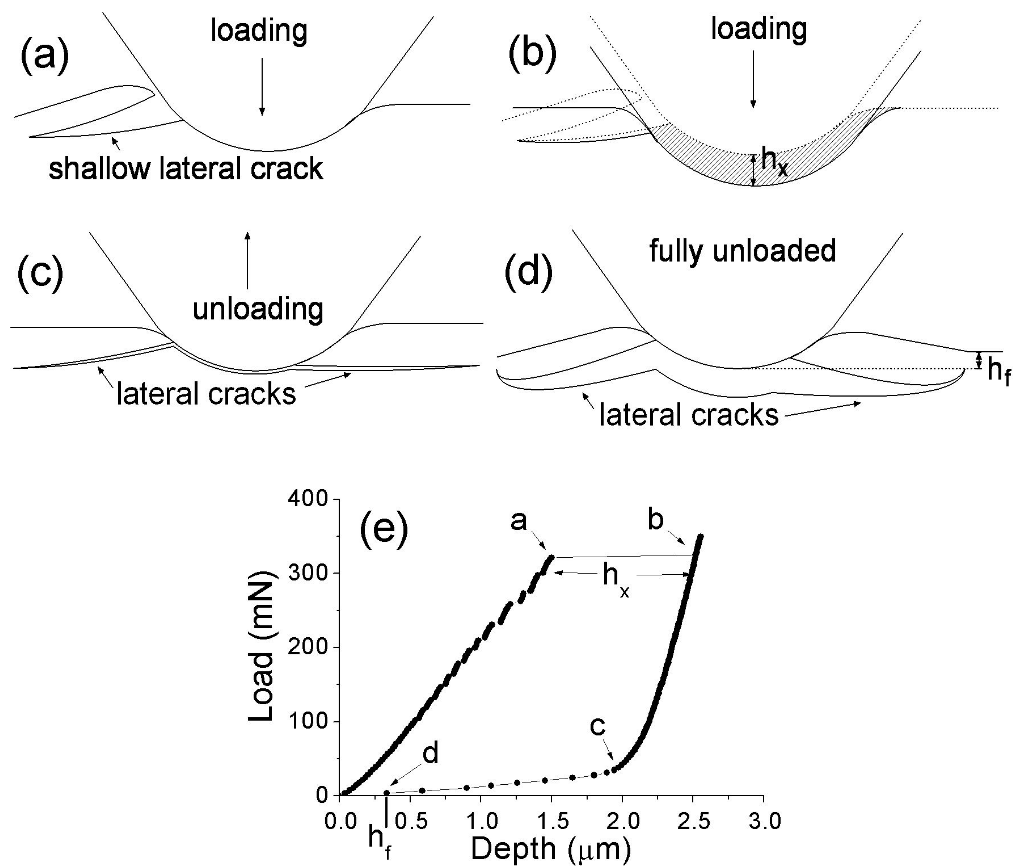

Figure 7.11: Schematic representation of the deformation process. (a) a shallow lateral crack opens, which (b) triggers material removal (shaded area), causing the indenter depth to increase by h_x. Initial unloading occurs by elastic recovery in the bulk. (c) When bulk recovery is complete, the tip loses contact with the base of the indent. Beyond this point, the force on the tip is due to lateral plates of material, until the tip is fully unloaded [diagram (d)]. (e) Force-displacement curve schematic, with points in the loading cycle corresponding to the diagrams marked.

After bulk recovery is completed, elbowing begins. At this point the indenter will actually lose contact with the bulk, only remaining in contact with the plates detached by lateral cracking. The subsequent force-displacement response, as well as the final depth after complete unloading, are then governed by the uplift of these lateral plates. A schematic of this full sequence of events is given in Fig. 7.11.

7.3.3 Phase transformation in Ge after giant pop-in

The Raman spectrum of Ge-I (diamond cubic) has a single first-order peak at 301 cm^{-1}. The peak broadens and shifts to higher wavenumbers (305-310 cm^{-1}) when compressive stresses are present. [27] Indents at loads up to 200 mN featured only the compressively

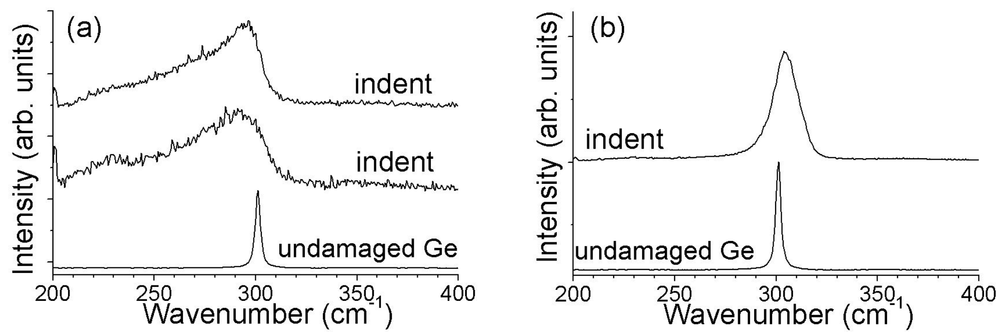

Figure 7.12: (a) Raman spectra from indents in Fig. 7.1(a) (giant pop-in), with spectrum from undamaged Ge for comparison, (b) Raman spectrum from indent in Fig. 7.1(b) (no giant pop-in).

shifted Ge-I peak in the Raman spectrum, as observed in previous studies. [27, 30] Some higher load indents exhibited a distinctly different Raman spectrum, consisting of a broad, asymmetric band peaking at 280-295 cm^{-1}. It resembles the Raman spectrum of a-Ge, which features a Gaussian band at ~270 cm^{-1}. This type of spectrum was only observed if the indent had undergone a giant pop-in. Typical examples from 350 mN spherical indents are shown in Fig. 7.12(a). Indents without a giant pop-in featured only the broadened peak at 305-310 cm^{-1}. Such a spectrum is shown in Fig. 7.12(b).

A number of 350 mN indents were analysed, 24 in total. Of the 10 indents which underwent a giant pop-in, all featured an amorphous Raman spectrum. All but one of the remaining indents without a giant pop-in, showed only the Ge-I peak; the last featured additional peaks (225, 242, and 272 cm^{-1}) corresponding to Ge-III.

Raman analysis on Berkovich indents and partial-unload spherical indents yielded similar results: indents with a giant pop-in featured a broad amorphous-like band in the Raman spectrum; other indents featured only the broadened and upshifted Ge-I peak.

A number of high-load indents, with and without a giant pop-in, were examined by Raman spectroscopy within three hours of indentation. The same correlation of the amorphous phase with the giant pop-in was noted. No extra peaks (corresponding to high-pressure phases) were observed.

To examine the effect of unloading rate, sets of 350 mN indents were made using slow unloading rates of 0.71 mN·s^{-1} and 0.34 mN·s^{-1}. Both sets of indents showed similar elbowing behaviour in the force-displacement curves as observed for faster unloading rates. Raman analysis on these indents again found that those with a giant pop-in featured an amorphous band, with no extra peaks observed; whilst those indents without a giant pop-in featured only the broadened and upshifted Ge-I peak.

Indents to loads of 300 mN and above were difficult to examine by FIB cross-sectioning and TEM. Attempts to prepare a cross-section of >100 nm thickness were frustrated by

high residual stresses and extensive cracking beneath the indents, which usually caused the cross-section to disintegrate during preparation. An intact cross-section obtained from a 400 mN indent, without a giant pop-in, is shown in Fig. 7.13. A high degree of damage is revealed. Thick damage bands on $(11\bar{1})$ and $(1\bar{1}1)$ planes are visible, indicative of twinning or slip. These extend $\sim 4\mu$m below the surface. Many of the damage bands terminate at the point where they meet another band on the opposing $\{111\}$ plane. Numerous cracks (bright features) are visible. Several of the cracks initiate at the intersection of two damage bands on opposing $\{111\}$ planes. One such crack is labelled in Fig. 7.13. Selected-area diffraction on the deformed region below the indent showed streaks and extra reflections indicative of twinning, as previously observed in Ge, [30] but no signs of amorphisation or other phase transformations, consistent with the Raman microspectroscopy results.

Giant pop-ins on multiple-cycle loading

Giant pop-ins were also found to occur at lower loads when Ge was subjected to multiple-cycle loading. Figure 7.14(a) shows a P-h curve of 5 load-unload cycles with a maximum load of 200 mN. The first cycle shows normal elastic-plastic behaviour on loading and elastic behaviour on unloading. The second loading cycle initially follows the first unloading cycle, but deviates from elasticity at $\sim$100 mN, and a giant pop-in occurs at $\sim$130 mN. Elbowing is observed in subsequent unloading and re-loading curves, with some hysteresis between unload curves and re-load curves.

Figure 7.14(b) shows a Raman spectrum taken from the same indent, with a spectrum from undamaged Ge for comparison. Both spectra feature a peak at $\sim$300 cm^{-1} corresponding to the original diamond cubic structure. The spectrum from the indent additionally features a broad shoulder from 200 to 300 cm^{-1}, indicating the presence of amorphous material in the indent.

Figure 7.14(c) shows a cross-sectional TEM micrograph of the indent. The black bands indicate slip or twin bands, as has previously been observed in Ge indents. [30] Additionally, a thin region of transformed material can be observed directly beneath the surface of the indent, darker in contrast than the undamaged Ge but lighter in contrast than the slip traces. SADP (inset) indicates this transformed phase to be amorphous or nanocrystalline. Amorphous material was not observed in TEM or Raman measurements for other multiple-cycle indents that had not undergone a giant pop-in.

Discussion of phase transformation after giant pop-in

Indents featuring a giant pop-in consistently contained a-Ge, whereas other indents contained only the original Ge-I phase. It is noted that if a lateral crack opens during loading,

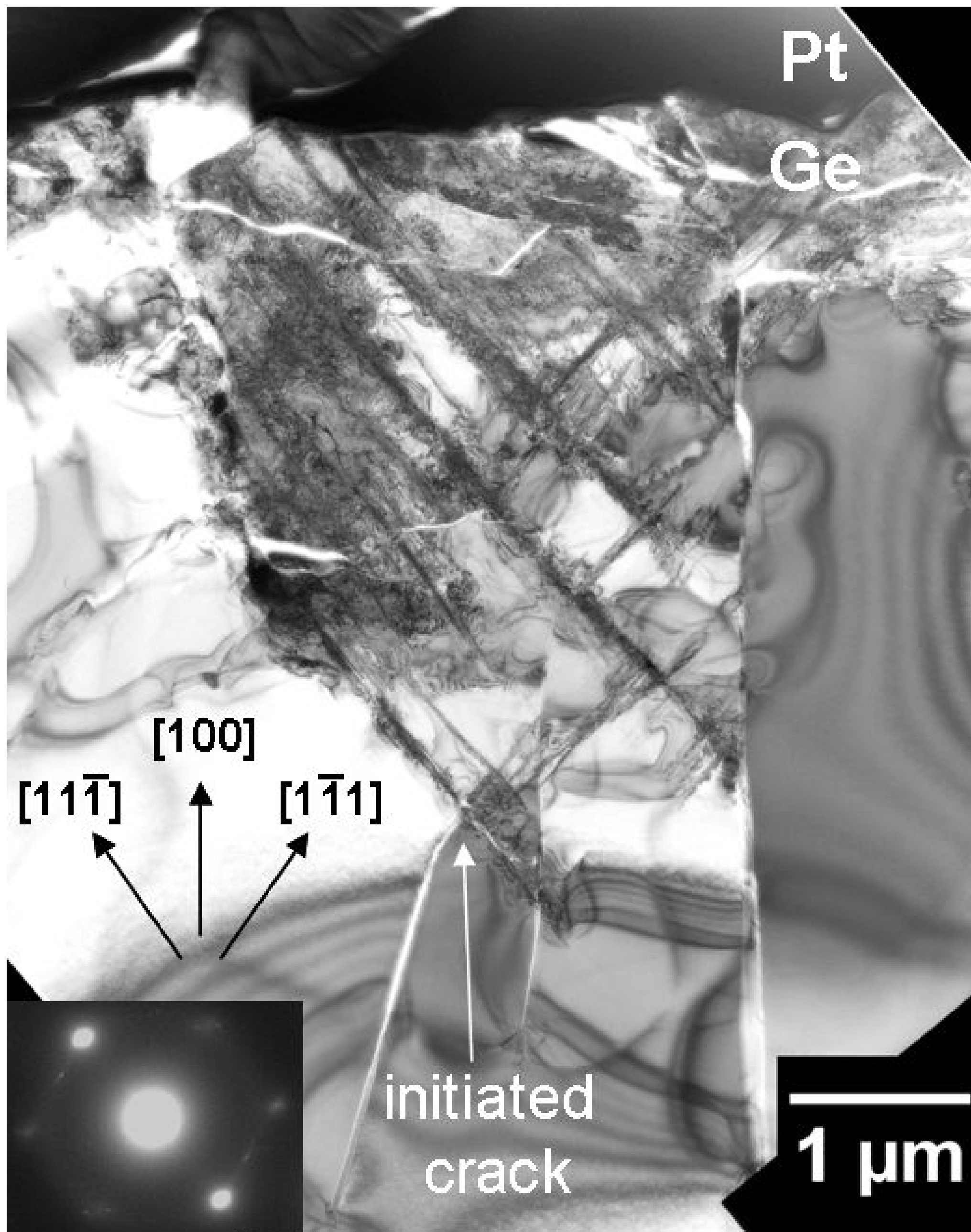

Figure 7.13: Cross-sectional bright-field TEM of a 400 mN indent without a giant pop-in. Inset: diffraction pattern from deformed region.

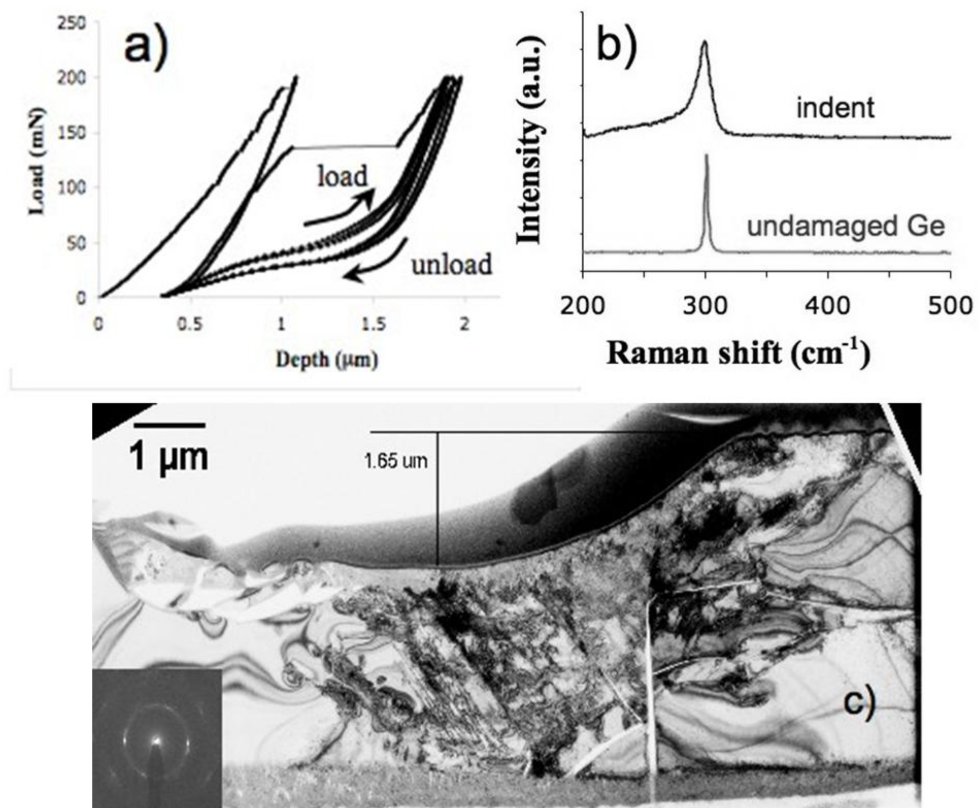

Figure 7.14: a) A multiple-loading (5 x 200 mN) P-h curve for Ge, featuring a giant pop-in. b) Raman spectra from the indent and from undeformed Ge. c) XTEM image of the indent, with inset SADP from region directly below indent showing the presence of a phase-transformed amorphous zone.

the contact area supporting the indenter is likely to decrease. With the contact area decreased, and the load unchanged, the contact pressure must necessarily increase extremely rapidly. Note also that the pressure increase would be transient: the increase in penetration depth after the material removal event would mean a greatly increased contact area, and consequently a diminished pressure. It seems most likely that these rapid pressure changes during the giant pop-in are responsible for creating the observed amorphous material.

One possibility is that a high-pressure metallic phase forms on pressure increase; the subsequent rapid pressure decrease would act to quench the metallic material to an amorphous structure, as occurs in Si when load is rapidly released. [22, 23] The other possibility is a direct transformation from Ge-I to a-Ge. Although there is little evidence for this type of behaviour in previous indentation studies, it is known that a high density of crystalline defects can induce amorphisation, by raising the free energy of the lattice. Such defect-induced amorphisation is observed, for example, under high-fluence ion implantation of semiconductors. [59, 60] However, given the similarity of the giant pop-in event to the rapid loading situation investigated in Chapter 3, a pressure-induced phase transformation is the more likely route. In further support of this view, the shape of the phase-transformed zone observed in Fig. 7.14 is hemispherical, corresponding to the region of greatest hydrostatic pressure. [47] If it was defect-induced then one would expect the transformed zone to be located deeper in the material along slip and twin planes where the defect concentration is highest. [154]

Clearly, phase transformations occur in Ge under high-load indentation that are absent at lower loads. This offers a possible explanation for the discrepancy between previous investigations utilizing high-load Vickers indentation, which observed a phase transformation in Ge, [19,26] and those utilizing low-load nanoindentation, which did not. [27,30] A giant pop-in would not be detected in a Vickers test, in which the only quantities measured during testing are the maximum applied load and the impression area after unloading.

7.4 Concluding remarks

The deformation behaviour of crystalline Ge under indentation has been studied over a wide load range. At low loads, deformation occurs via shear-induced slip and mechanical twinning. As load increases, cracks develop, nucleated at the intersections of shear-damage bands. At a certain critical load, a dramatic material removal event occurs, in which material is forcefully ejected from the central zone of deformation beneath the indenter. This gives rise to a very large pop-in feature in the indentation force-displacement curve. The material removal event appears to be triggered by the development of a shal-

low lateral crack immediately adjacent to the indenter, which releases the compressed material beneath the indenter from confinement.

The material removal event relieves a significant fraction of the elastic strain induced by indentation. Consequently, during unloading, before the load is fully released, bulk elastic recovery reaches completion and lateral crack opening commences. This gives rise to elbowing in the force-displacement curve. The linear and compliant post-elbowing response is in agreement with the predicted behaviour of plates of material detached by lateral cracks.

Interestingly, after the giant pop-in, residual indents contain an amorphous-like structural phase. This phase appears to be the result of the sudden pressure changes associated with the giant pop-in. It is most likely that the amorphous material is the product of a high-pressure metallic phase transformation. Below the critical load for giant pop-in, the material in the residual indent is untransformed from the Ge-I phase. This suggests that the conflicting reports on the indentation behaviour of crystalline Ge may be partially attributable to differences in maximum load between studies. The giant pop-in that is observed under large-scale deformation in Ge triggers a phase transformation to a-Ge that is absent at smaller scales.

It could be argued that the giant pop-in events described here are not specific to Ge or Si, but should apply to any highly brittle material. Highly brittle refers to materials with low threshold loads P_C, specifically materials with large values of H/K_C, the so-called "brittleness index". [53] Si and Ge fall into the upper range of brittleness, due to their highly covalent bonding. Other candidate materials are diamond, silicon carbide, sapphire, silicon nitride, III-V semiconductors, and some glasses. Giant pop-ins have also been observed in thin film systems. [155,156] In these latter systems an additional trigger for spallation is film delamination along a weakly adhering interface, in which case the pop-in displacement may be governed more by film thickness than by plastic zone size.

CHAPTER 8

Synopsis and concluding remarks

8.1 General observations

This dissertation has investigated the nanoindentation response under different loading conditions. In Chapter 3 it was found that loading rate controls the deformation mechanism of indented Ge. At slower rates, typical of normal nanoindentation testing, Ge inelastically deforms by shear-induced twinning and punching-out of dislocations. At very rapid loading rates, pressure-induced phase transformation becomes an important deformation mechanism. Whereas twinning and dislocation slip are strain rate-sensitive deformation mechanisms, limited by the speed of propagation of the defects involved, phase transformation is rate-insensitive under the loading conditions explored. When loading rate is increased, then, the critical stress for shear deformation will increase to the point that phase transformation becomes a more favourable response.

At greater maximum loads, significant fracture occurs during indentation. Lateral cracks develop running outwards from the plastic impression, parallel to the free surface. The material above these lateral cracks can detach entirely from the specimen, leading to spallation and debris generation. It was found in Chapter 7 that the nanoindentation P-h response shows dramatic evidence of this material removal. The removal of material immediately adjacent to the indenter tip reduces support of the tip, causing a sudden incursion of the tip into the sample. This is seen in the P-h curve as a 'giant pop-in' displacement event of magnitude 1 μm or more. In many cases, this fracture-related displacement is comparable to or greater than the displacement due to elastic-plastic deformation. Giant pop-ins were observed for germanium and silicon and it is proposed that they are a general phenomenon that should be observable in all sufficiently brittle materials.

In Ge, the giant pop-in was associated with the formation of amorphous material within the indent. This is probably due to the observed loading rate effect on the likelihood of phase transformation. When material removal occurs during the giant pop-in, the stress in the remaining material supporting the indenter will increase very rapidly. This

is equivalent to carrying out a rapid loading rate test and would be expected to promote phase transformation.

The dependence on loading rate and maximum load observed in this study helps to understand why such varied results have been found for Ge in the literature. Both loading rate and maximum load are higher for microindentation tests, favouring phase transformation. Loading rate deserves further comment. The relevant factor will in fact be the strain rate or rate of stress increase, which will also depend on the indenter shape. For some indenter geometries there may be rapid strain rates at certain parts of the loading curve even at relatively low overall loading rates, thus also favouring phase transformation. Finally it must be remembered that indentation is a statistical process and the stress field after plasticity is complex and inhomegeneous. Pinning and other work-hardening processes lead to increased hydrostatic stress and in rare events this may be sufficient to cause phase transformation even at low loads and loading rates.

As well as loading conditions, sample geometry was found to have a strong effect on the favoured deformation mechanism. For Ge in thin film form, the dominant deformation mechanism was found to depend critically on the thickness of the film, as described in Chapter 6. For very thin films, pressure-induced phase transformation dominates; for thick films, shear deformation dominates. The critical film thickness is directly proportional to the radius of the indenter, and will also be affected by the underlying substrate material.

The nanoindentation response of ion-implanted crystalline Ge was investigated. Although ion implantation introduces a high density of defects into the material, these defects were found not to hinder shear deformation, but to aid it, causing increased ductility and a noticeable drop in hardness. It is proposed that point defects and broken bonds present in high densities after implantation aid plasticity in Ge, by facilitating the nucleation and propagation of kinks on dislocation lines. A low temperature anneal, suitable for removing point defects and repairing dangling bonds, is found to reverse the hardness drop in implanted Ge samples. Positron annihilation spectroscopy showed that annealing caused the formation of larger open-volume defects, which were not found to significantly reduce the hardness relative to pristine material.

Ion implantation at higher doses was used to generate fully amorphous Ge layers for nanoindentation study. Amorphous Ge was studied in both as-implanted ‘unrelaxed’ form and annealed ‘relaxed’ form. Although the relaxed and unrelaxed a-Ge specimens showed significant differences in the degree of structural order, both types were found to deform under indentation by a pressure-induced phase transformation. Correspondingly, both types had approximately equal hardnesses. This contrasts with the behaviour of a-Si, which deforms by shear plasticity in its unrelaxed form and by phase transformation in its

Table 8.1: Indentation conditions investigated in this work and associated deformation mechanisms observed.

Case	Deformation mechanism	End phase(s)
c-Ge at moderate loading rates	Shear-induced slip and twinning	Ge-I
c-Ge at rapid loading rates	Slip, twinning + phase transformation	Ge-I, a-Ge, occasionally Ge-III
c-Ge with defects	Enhanced shear plasticity	Ge-I
a-Ge	Phase transformation	a-Ge, Ge-I
c-Ge at high loads	Cracking, spallation, phase transformation	Ge-I, a-Ge
thin film c-Ge on Si	Phase transformation	a-Ge

relaxed form, and consequently shows a noticeable hardness difference between the two types. This is an intriguing reversal of the situation for the crystalline materials, where phase transformation is significantly more favourable for Si than for Ge.

Interestingly, in the cases where evidence for a pressure-induced phase transformation was observed in indented c-Ge, the metastable crystalline phase Ge-III was rarely observed as an end product. Instead, a-Ge was usually observed. In this study no evidence was found for an effect of the unloading rate on the end phase of Ge. By comparison, c-Si when indented may transform primarily to Si-III and Si-XII or primarily to a-Si, depending the loading conditions and in particular the unloading rate. At this stage, explanations for this discrepancy are necessarily speculative. One possibility is that the conditions needed to induce a high-pressure phase transformation in Ge may also tend to promote the formation of a-Ge rather than Ge-III. For instance, the need for a very thin film in the thin film case means that the volume of transformed Ge is small, reducing the probability of Ge-III nucleating on unloading. Another possibility to consider is that the phase obtained under load is not Ge-II but another phase, such as a high-density amorphous phase. Further work is needed to understand this issue.

This complex set of results is summarised in Table 8.1. The next section will present a unified framework for understanding the dependence of the deformation mechanism on loading conditions and sample preparation.

8.2 Deformation mechanisms in germanium

To understand the diversity of deformation responses that have been demonstrated in Ge, the indentation process must be considered in general terms. Indentation initially generates purely elastic deformation within the material. This is true not only for spherical indenters but for all indenters, including 'sharp' Berkovich and cube-corner indenters,

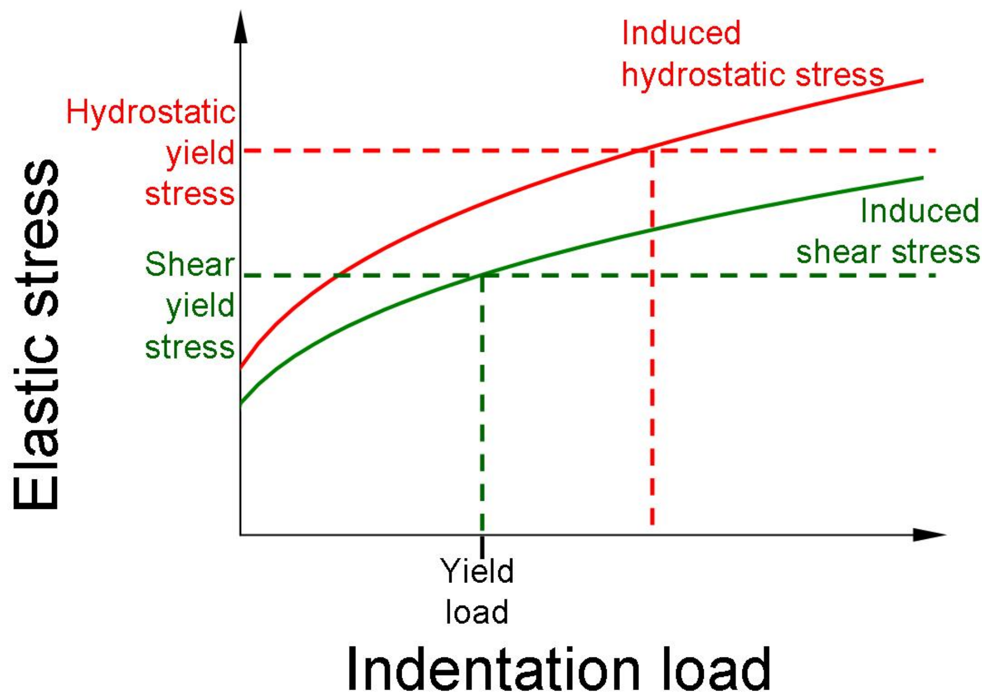

Figure 8.1: Schematic of elastic stresses (shear stress and hydrostatic stress) as a function of indenter load during an indentation test and point of intersection with yield stresses, illustrating the case for c-Ge at moderate loading rates.

because these are invariably bluntened at the very tip. Thus elastic stresses are generated, which intensify as load on the indenter is increased. The density of stored elastic energy consequently increases, until inelastic deformation eventually becomes a favourable response. The inelastic mechanism activated is determined by the magnitudes of different stresses and the stress thresholds for the possible deformation mechanisms.

This situation is schematically illustrated in Fig. 8.1. Hydrostatic stress and shear stress both increase with load, at different rates. Shear deformation (slip, twinning) and hydrostatic deformation (phase transformation) both have associated yield stresses that must be reached for the mechanism to occur. Inelastic deformation occurs at the load where the two lines, yield stress (dotted line) and induced stress (solid line) intersect. In reality, yield will occur at the lower load intersection point. In the case shown in Fig. 8.1 the shear stress threshold is reached at a lower load and thus the shear mechanism represented (e.g. slip or twinning) will be activated. This corresponds to the case of bulk c-Ge indented at moderate loading rates. Beyond the yield load, inelastic deformation will act to relieve elastic strain.

The majority of the results within this thesis can be understood in terms of Fig. 8.1. In Chapter 3 rapid loading increases the shear yield stress, to the point where hydro-

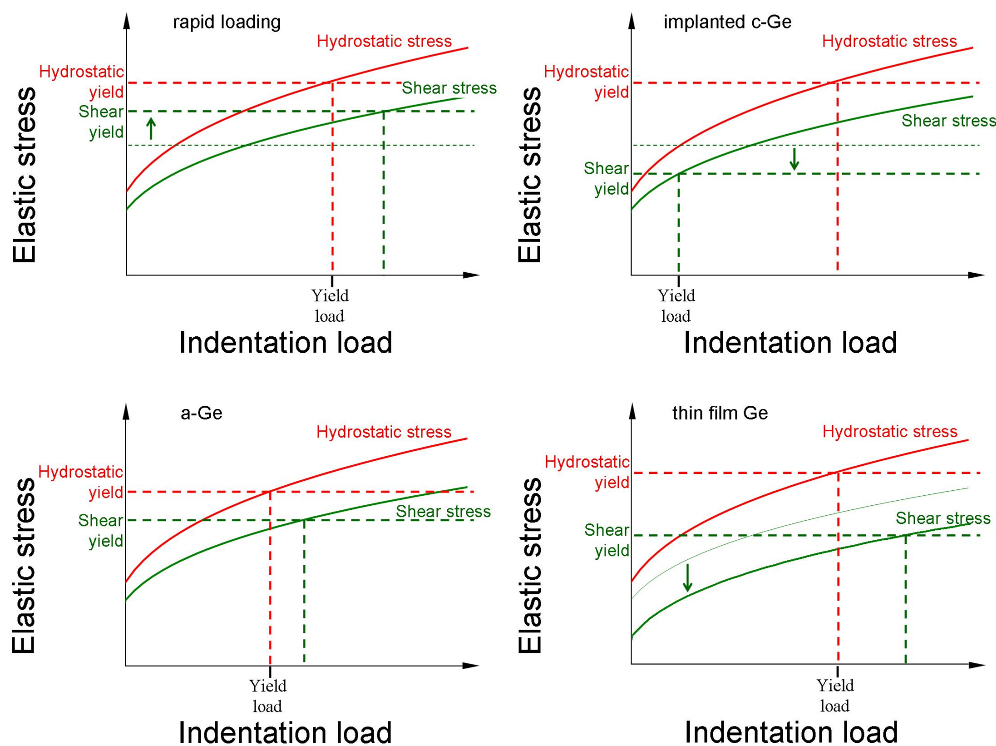

Figure 8.2: Schematic of elastic stresses and yield stresses for various cases: (a) c-Ge indented at rapid loading rates, (b) ion-implanted c-Ge with defects, (c) amorphous Ge, (d) thin film Ge.

static yield (i.e., phase transformation) becomes a competitive option. This is illustrated schematically in Fig. 8.2(a). In Chapter 4, implantation-induced disorder lowers the shear yield stress by favouring defect formation and propagation, leading to enhanced plasticity within the implanted film and associated softening. This is illustrated in Fig. 8.2(b).

For a-Ge (Chapter 5) the hydrostatic yield stress (transformation pressure) is lower than in c-Ge, and consequently high-pressure phase transformation occurs during indentation. Fig. 8.2(c) makes it clear that it is not sufficient for the transformation pressure to be lower in absolute terms: it must be lower relative to the shear yield stress of a-Ge, which may well be different to that of c-Ge.

For the Ge thin films examined in Chapter 6, the yield thresholds are not changed from bulk Ge values but the stress state is modified. Shear stress is reduced in the film because the maximum shear stress lies in the substrate. Hydrostatic stress is unchanged because the maximum lies at the surface within the film. For sufficiently thin films, phase transformation becomes favourable. This case is shown in Fig. 8.2(d).

Finally, the giant pop-ins investigated in Chapter 7 illustrate the importance of a third mode of stress, tensile stress. The tensile stresses that cause lateral cracking, spallation

and thus giant pop-in are part of the complex elastic-plastic stress field that is found after significant inelastic deformation. When tensile stresses become sufficiently high, cracking is activated, eventually resulting in spalling. In turn, the rapid loading experienced immediately after the giant pop-in event promotes phase transformation.

8.3 Future directions

This work has shown that it is possible to achieve nanoindentation-induced phase transformations in Ge under the right conditions: at very fast loading rates, in a thin film geometry, or in amorphous form. This means the phase transformation behaviour could be utilised for many of the technological applications that have been proposed for Si.

As noted, the end phase obtained after indentation of c-Ge is usually a-Ge, and rarely Ge-III. For indentation of a-Ge, the end phase is usually Ge-I. Further work should aim to understand why Ge differs in these respects from Si and why the formation of Ge-III is relatively unfavourable. It would be helpful to identify with certainty the high-pressure phase obtained under load. Applying techniques such as Raman analysis and TEM *in situ* during indentation might resolve this difficulty, but there are significant challenges to be overcome with existing *in situ* methods. Detailed theoretical modelling might also help to understand the sequence of structural changes taking place in Ge.

Many of the behaviours for Ge described in this work are derived from general physical principles, and should be observable in other similar materials, such as III-V covalent semiconductors. The loading rate effect, for example arises from the greater rate sensitivity of shear deformation compared to pressure-induced phase transformation. This behaviour should be observable in other materials. Likewise, the favouring of phase transformation in thin film Ge arises from the geometry of stresses beneath the indenter, and should also be observable in other materials, given a sufficiently thin film and hard underlying substrate. As noted in the introduction (Fig. 1.2), Ge lies particularly close to the boundary between phase transformation and shear deformation. Thus, for other materials, more extreme conditions are likely to be necessary to achieve similar behaviours.

It would be worthwhile to investigate whether other covalent semiconductors showed a similar drop in hardness after ion implantation. The hardness-reduction mechanism proposed in this thesis might be expected to extend to other covalent semiconductors. It would also be interesting to see whether the nature of implantation damage is important, for instance by implanting ions of different masses and carrying out implants at different temperatures.

Finally, one important parameter that has not been investigated in this work is the effect of temperature on the indentation response. Since the pioneering microindentation

studies of Gridneva and co-workers, very little has been done in this area, either for Ge or for any related material. Carrying out nanoindentation tests at low or high temperatures is technically challenging, largely due to thermal drift issues. If these issues were overcome, temperature control would be a powerful means of controlling the deformation response in a given material, opening up many potential applications.

Bibliography

[1] Michael Riordan and Lillian Hoddeson. *Crystal fire : the birth of the information age*. Norton, New York, 1997.

[2] Shu Nakaharai, Tsutomu Tezuka, Naoharu Sugiyama, Yoshihiko Moriyama, and Shin-Ichi Takagi. Characterization of 7-nm-thick strained Ge-on-insulator layer fabricated by Ge-condensation technique. *Appl. Phys. Lett.*, 83(17):3516–3518, 2003.

[3] Yaocheng Liu, Michael D. Deal, and James D. Plummer. High-quality single-crystal Ge on insulator by liquid-phase epitaxy on Si substrates. *Appl. Phys. Lett.*, 84(14):2563–2565, 2004.

[4] J. W. Seo, Ch. Dieker, J.-P. Locquet, G. Mavrou, and A. Dimoulas. HfO_2 high-k dielectrics grown on (100)Ge with ultrathin passivation layers: Structure and interfacial stability. *Appl. Phys. Lett.*, 87(22):221906, 2005.

[5] Douglas D. Cannon, Jifeng Liu, Yasuhiko Ishikawa, Kazumi Wada, David T. Danielson, Samerkhae Jongthammanurak, Jurgen Michel, and Lionel C. Kimerling. Tensile strained epitaxial Ge films on Si(100) substrates with potential application in L-band telecommunications. *Appl. Phys. Lett.*, 84(6):906–908, 2004.

[6] Lorenzo Colace, Gianlorenzo Masini, Stefano Cozza, Gaetano Assanto, Francesco DeNotaristefani, and Valentino Cencelli. Near-infrared camera in polycrystalline germanium integrated on complementary-metal-oxide semiconductor electronics. *Appl. Phys. Lett.*, 90(1):011103, 2007.

[7] S. Minomura and H. G. Drickamer. Pressure induced phase transitions in silicon, germanium and some III-V compounds. *J. phys. chem. sol.*, 23(5):451–456, 1962.

[8] J. C. Jamieson. Crystal structures at high pressures of metallic modifications of silicon and germanium. *Science*, 139(3556):762–764, 1963.

[9] C. S. Menoni, J. Z. Hu, and I. L. Spain. Germanium at high pressures. *Phys. Rev. B*, 34(1):362–367, 1986.

[10] Jing Zhu Hu, Larry D. Merkle, Carmen S. Menoni, and Ian L. Spain. Crystal data for high-pressure phases of silicon. *Phys. Rev. B*, 34:4679–4684, 1986.

[11] S. B. Qadri, E. F. Skelton, and A. W. Webb. High-pressure studies of Ge using synchrotron radiation. *J. Appl. Phys.*, 54(6):3609–3611, 1983.

[12] J. S. Kasper and S. M. Richards. The crystal structures of new forms of silicon and germanium. *Acta Cryst.*, 17:752, 1964.

[13] F. P. Bundy and J. S. Kasper. A new dense form of solid germanium. *Science*, 139(3552):340–341, 1963.

[14] R. J. Nelmes, M. I. McMahon, N. G. Wright, D. R. Allan, and J. S. Loveday. Stability and crystal structure of bc8 germanium. *Phys. Rev. B*, 48(13):9883–9886, 1993.

[15] J. M. Besson, E. H. Mokhtari, J. Gonzalez, and G. Weill. Electrical-properties of semimetallic silicon-III and semiconductive silicon-IV at ambient pressure. *Phys. Rev. Lett.*, 59(4):473–476, 1987.

[16] R. O. Piltz, J. R. Maclean, S. J. Clark, G. J. Ackland, P. D. Hatton, and J. Crain. Structure and properties of silicon XII: A complex tetrahedrally bonded phase. *Phys. Rev. B*, 52(6):4072 – 4085, 1995.

[17] I. V. Gridneva, Yu. V. Milman, and V. I. Trefilov. Phase transition in diamond-structure crystals during hardness measurements. *Phys. Status Solidi A*, 14:177–182, 1972.

[18] A. P. Gerk and D. Tabor. Indentation hardness and semiconductor-metal transition of germanium and silicon. *Nature*, 271:732–733, 1978.

[19] D. R. Clarke, M. C. Kroll, P. D. Kirchner, R. F. Cook, and B. J. Hockey. Amorphization and conductivity of silicon and germanium induced by indentation. *Phys. Rev. Lett.*, 60(21):2156–2159, 1988.

[20] V. Domnich and Y.G. Gogotsi. Phase transformations in silicon under contact loading. *Rev. Adv. Mater. Sci.*, 3:1–36, 2002.

[21] A. Kailer, Y. G. Gogotsi, and K. G. Nickel. Phase transformations of silicon caused by contact loading. *J. Appl. Phys.*, 81(7):3057–3063, 1997.

[22] V. Domnich, Y. Gogotsi, and S. N. Dub. Effect of phase transformations on the shape of the unloading curve in the nanoindentation of silicon. *Appl. Phys. Lett.*, 76(16):2214–2216, 2000.

[23] J. E. Bradby, J. S. Williams, J. Wong-Leung, M. V. Swain, and P. Munroe. Transmission electron microscopy observation of deformation microstructure under spherical indentation in silicon. *Appl. Phys. Lett.*, 77(23):3749–3751, 2000.

[24] Kyoko Minowa and Koji Sumino. Stress-induced amorphization of silicon crystal by mechanical scratching. *Phys. Rev. Lett.*, 69(2):320 LP – 322, 1992.

[25] Peter N. Blake and Ronald O Scattergood. Ductile-regime machining of germanium and silicon. *J. Am. Ceram. Soc.*, 73(4):949–957, 1990.

[26] A. Kailer, K. G. Nickel, and Y. G. Gogotsi. Raman microspectroscopy of nanocrystalline and amorphous phases in hardness indentations. *J. Raman Spectr.*, 30:939–946, 1999.

[27] Y. G. Gogotsi, V. Domnich, S. N. Dub, A. Kailer, and K. G. Nickel. Cyclic nanoindentation and Raman microspectroscopy study of phase transformations in semiconductors. *J. Mater. Res.*, 15(3):871–879, 2000.

[28] G. M. Pharr, W. C. Oliver, R. F. Cook, P. D. Kirchner, M. C. Kroll, T. R. Dinger, and D. R. Clarke. Electrical resistance of metallic contacts on silicon and germanium during indentation. *J. Mater. Res.*, 7:961, 1992.

[29] S. J. Lloyd, J. M. Molina-Aldareguia, and W. J. Clegg. Deformation under nanoindents in Si, Ge, and GaAs examined through transmission electron microscopy. *J. Mater. Res.*, 16(12):3347 – 3350, 2001.

[30] J. E. Bradby, J. S. Williams, J. Wong-Leung, M. V. Swain, and P. Munroe. Nanoindentation-induced deformation of Ge. *Appl. Phys. Lett.*, 80(15):2651–2653, 2002.

[31] J. Jang, M. J. Lance, Songqing Wen, and G. M. Pharr. Evidence for nanoindentation-induced phase transformations in germanium. *Appl. Phys. Lett.*, 86:131907, 2005.

[32] J. J. Gilman. Insulator-metal transitions at microindentations. *J. Mater. Res.*, 7(3):535–538, 1992.

[33] J. E. Bradby, J. S. Williams, J. Wong-Leung, M. V. Swain, and P. Munroe. Mechanical deformation of InP and GaAs by spherical indentation. *Appl. Phys. Lett.*, 78(21):3235–3237, 2001.

[34] J. E. Bradby, S. O. Kucheyev, J. S. Williams, C. Jagadish, M. V. Swain, P. Munroe, and M. R. Phillips. Contact-induced defect propagation in ZnO. *Appl. Phys. Lett.*, 80(24):4537–4539, 2002.

[35] J. E. Bradby, S. O. Kucheyev, J. S. Williams, J. Wong-Leung, M. V. Swain, P. Munroe, G. Li, and M. R. Phillips. Indentation-induced damage in GaN epilayers. *Appl. Phys. Lett.*, 80(3):383–385, 2002.

[36] J. E. Bradby. *Nanoindentation-Induced Deformation of Semiconductors*. PhD thesis, Research School of Physical Sciences and Engineering, Australian National University, September 2002.

[37] Friedrich Mohs. *Treatise on Mineralogy*. A. Constable and co., Edinburgh, 1825.

[38] B. W. Mott. *Micro-indentation hardness testing*. Butterworths Scientific Publications, London, 1956.

[39] David Tabor. *The hardness of metals*. Clarendon Press (Oxford University Press), Oxford, 1951.

[40] X. Cai and H. Bangert. Hardness measurements of thin films - determining the critical ratio of depth to thickness using FEM. *Thin Solid Films*, 264(1):59–71, 1995.

[41] A. C. Fischer-Cripps. *Nanoindentation*. Springer-Verlag, New York, 2002.

[42] W.C. Oliver and G.M. Pharr. An improved technique for determining hardness and elastic modulus using load and displacement sensing indentation experiments. *J. Mater. Res.*, 7(6):1565–1583, 1992.

[43] W.C. Oliver and G.M. Pharr. Measurement of hardness and elastic modulus by instrumented indentation: Advances in understanding and refinements to methodology. *J. Mater. Res.*, 19(1):3–20, 2004.

[44] Ian N. Sneddon. The relation between load and penetration in the axisymmetric boussinesq problem for a punch of arbitrary profile. *Int. J. Eng. Sci.*, 3(1):47, 1965.

[45] J. S. Field and M. V. Swain. A simple predictive model for spherical indentation. *J. Mater. Res.*, 8(2):297–306, 1993.

[46] H. A. Francis. Phenomenological analysis of plastic spherical indentation. *Trans. of the ASME*, 98(3):272–281, 1976.

[47] K.L. Johnson. *Contact Mechanics*. Cambridge University Press, Cambridge, 1985.

[48] B. R. Lawn. *Fracture of Brittle Solids*. Cambridge University Press, Cambridge, 2nd edition, 1993.

[49] R. F. Cook and G. M. Pharr. Direct observation and analysis of indentation cracking in glasses and ceramics. *J. Am. Ceram. Soc.*, 73(4):787–817, 1990.

[50] Brian Lawn and Rodney Wilshaw. Indentation fracture: principles and applications. *J. Mater. Sci.*, 10(6):1049–1081, 1975.

[51] B. R. Lawn and A. G. Evans. A model for crack initiation in elastic/plastic indentation fields. *J. Mater. Sci.*, 12(11):2195, 1977.

[52] A. Arora, D. B. Marshall, B. R. Lawn, and M. V. Swain. Indentation deformation/fracture of normal and anomalous glasses. *J. Non-Cryst. Solids*, 31(3):415, 1979.

[53] B. R. Lawn and D. B. Marshall. Hardness, toughness, and brittleness: An indentation analysis. *J. Am. Ceram. Soc.*, 62(7-8):347–350, 1979.

[54] B. R. Lawn, A. G. Evans, and D. B. Marshall. Elastic-plastic indentation damage in ceramics - the median-radial crack system. *J. Am. Ceram. Soc.*, 63(9-10):574–581, 1980.

[55] G. R. Anstis, P. Chantikul, B. R. Lawn, and D. B. Marshall. A critical-evaluation of indentation techniques for measuring fracture-toughness .1. direct crack measurements. *J. Am. Ceram. Soc.*, 64(9):533–538, 1981.

[56] D. B. Marshall, B. R. Lawn, and A. G. Evans. Elastic plastic indentation damage in ceramics - the lateral crack system. *J. Am. Ceram. Soc.*, 65(11):561–566, 1982.

[57] E. Cottereau. DC accelerators. Technical report, 2001.

[58] J. S. Williams. Materials modification with ion beams. *Rep. Prog. Phys.*, 49:491–587, 1986.

[59] James W. Corbett, James P. Karins, and Teh Y. Tan. Ion-induced defects in semiconductors. *Nucl. Instrum. Methods*, 182-183(1):457–476, 1981.

[60] J.F. Gibbons. Ion implantation in semiconductors - part II: Damage production and annealing. *Proceedings of the IEEE*, 60(9):1062–1096, 1972.

[61] John R. Dennis and Edward B. Hale. Crystalline to amorphous transformation in ion-implanted silicon: a composite model. *J Appl Phys*, 49(3):1119–1127, 1978.

[62] C. V. Raman and K. S. Krishnan. A new type of secondary radiation. *Nature*, 121(3048):501–502, 1928.

[63] G. Lucazeau and L. Abello. Raman spectroscopy in solid state physics and materials science. theory, techniques and applications. *Analusis*, 23:301–311, 1995.

[64] Jun-ichi Takahashi and Takahiro Makino. Raman scattering measurement of silicon-on-insulator substrates formed by high-dose oxygen-ion implantation. *J. Appl. Phys.*, 63(1):87–91, 1988.

[65] D. McMullan. Scanning electron microscopy 1928 - 1965. In *51st Annual Meeting of the Microscopy Society of America*, Cincinnati, 1993.

[66] David B. Williams and C. Barry Carter. *Transmission electron microscopy: a textbook for materials science*. Plenum Press, New York, 1996.

[67] G. Binnig, C. F. Quate, and Ch. Gerber. Atomic force microscope. *Phys. Rev. Lett.*, 56(9):930 LP – 933, 1986.

[68] Peter J. Schultz and K. G. Lynn. Interaction of positron beams with surfaces, thin films, and interfaces. *Rev. Mod. Phys.*, 60(3):701 LP – 779, 1988.

[69] P. Asoka-Kumar, K. G. Lynn, and D. O. Welch. Characterization of defects in Si and SiO_2 - Si using positrons. *J. Appl. Phys.*, 76(9):4935–4982, 1994.

[70] M. Hakala, M. J. Puska, and R. M. Nieminen. Momentum distributions of electron-positron pairs annihilating at vacancy clusters in Si. *Phys. Rev. B*, 57(13):7621 LP – 7627, 1998.

[71] G. D. Quinn, P. J. Patel, and I. Lloyd. Effect of loading rate upon conventional ceramic microindentation hardness. *Journal of Research of the National Institute of Standards and Technology*, 107(3):299–306, 2002.

[72] H. Siethoff, K. Ahlborn, and W. Schroter. New analysis of the yield point of germanium. *Phys. Stat. Sol. A*, 174(1):205–212, 1999.

[73] H. Alexander and P. Haasen. Dislocations and plastic flow in the diamond structure. *Sol. State Phys.*, 22:27, 1968.

[74] F. C. Serbena and S. G. Roberts. The brittle-to-ductile transition in germanium. *Acta Metall. et Mater.*, 42(7):2505–10, 1994.

[75] P. Pirouz, A. V. Samant, M. H. Hong, A. Moulin, and L. P. Kubin. On temperature dependence of deformation mechanism and the brittle-ductile transition in semiconductors. *J. Mater. Res.*, 14(7):2783–2793, 1999.

[76] P. Pirouz and P. M. Hazzledine. Cross-slip and twinning in semiconductors. *Scripta Metall. Mat.*, 25(5):1167–1172, 1991.

[77] Y. Androussi, G. Vanderschaeve, and A. Lefebvre. Slip and twinning in high-stress-deformed GaAs and the influence of doping. *Philos. Mag. A*, 59(6):1189–1204, 1989.

[78] Hiroaki Kishimura and Hitoshi Matsumoto. Effect of phase transition in shock-recovered silicon. *J. Appl. Phys.*, 103(2):023505, 2008.

[79] G. J. Ackland. High-pressure phases of group IV and III-V semiconductors. *Rep. Prog. Phys.*, 64(4):483–516, 2001.

[80] Hannelore Katzke, Ulrich Bismayer, and Pierre Toledano. Theory of the high-pressure structural phase transitions in Si, Ge, Sn, and Pb. *Phys. Rev. B*, 73(13):134105, 2006.

[81] T. O. Mulhearn and D. Tabor. Creep and hardness of metals - a physical study. *Journal of the Institute of Metals*, 89(1):7–12, 1960.

[82] S. Ruffell, J. E. Bradby, N. Fujisawa, and J. S. Williams. Identification of nanoindentation-induced phase changes in silicon by in situ electrical characterization. *J. Appl. Phys.*, 101(8):083531, 2007.

[83] I. Zarudi, L. C. Zhang, and M. V. Swain. Behavior of monocrystalline silicon under cyclic microindentations with a spherical indenter. *Appl. Phys. Lett.*, 82(7):1027–1029, 2003.

[84] R. Rao, J. E. Bradby, and J. S. Williams. Patterning of silicon by indentation and chemical etching. *Appl. Phys. Lett.*, 91(12):123113, 2007.

[85] S. N. Dub. Pressure-induced phase transformations in germanium studied by nanoindentation. *J. Superhard Mater.*, 21(6):32–40, 1999.

[86] G. Carter and W. A. Grant. Amorphisation of solids by ion implantation. *Nuc. Inst. Meth. Phys. Res.*, 199(1-2):17–35, 1982.

[87] T. H. Courtney. *Mechanical behavior of materials*. McGraw-Hill, Boston, 2nd edition, 2000.

[88] D Hull and D J Bacon. *Introduction to Dislocations*. Pergamon Press, Oxford, 3rd edition, 1984.

[89] F. M. Gao, J. L. He, E. D. Wu, S. M. Liu, D. L. Yu, D. C. Li, S. Y. Zhang, and Y. J. Tian. Hardness of covalent crystals. *Phys. Rev. Lett.*, 91(1):015502, 2003.

[90] F. M. Gao. Theoretical model of intrinsic hardness. *Phys. Rev. B*, 73(13):132104, 2006.

[91] Antonin Simunek and Jiri Vackar. Hardness of covalent and ionic crystals: First-principle calculations. *Phys. Rev. Lett.*, 96(8):085501, 2006.

[92] A. Vehanen, K. Saarinen, P. Hautojärvi, and H. Huomo. Profiling multilayer structures with monoenergetic positrons. *Phys. Rev. B*, 35(10):4606 LP – 4610, 1987.

[93] A. Polity and F. Rudolf. Defects in electron-irradiated Ge studied by positron lifetime spectroscopy. *Phys. Rev. B*, 59(15):10025 LP – 10030, 1999.

[94] K. Kuitunen, F. Tuomisto, J. Slotte, and I. Capan. Divacancy clustering in neutron-irradiated and annealed n-type germanium. *Phys. Rev. B*, 78(3):033202, 2008.

[95] S Ruffell, P J Simpson, and A P Knights. The effect of the annealing ramp rate on the formation of voids in silicon. *J. Phys.: Condens. Matter*, (46):466202, 2007.

[96] A.R. Peaker, V.P. Markevich, L.I. Murin, N.V. Abrosimov, and V.V. Litvinov. Ion implantation and electron irradiation damage in unstrained germanium and silicon-germanium alloys. *Mater. Sci. Eng. B*, 124-125:166–169, 2005.

[97] V.P. Markevich, A.R. Peaker, A.V. Markevich, V.V. Litvinov, L.I. Murin, and V.V. Emtsev. Interaction of self-interstitials with oxygen-related defects in electron-irradiated Ge crystals. *Materials Science in Semiconductor Processing*, 9(4-5):613–618, 2006.

[98] T. Akatsu, K. K. Bourdelle, C. Richtarch, B. Faure, and F. Letertre. Study of extended-defect formation in Ge and Si after H ion implantation. *Appl. Phys. Lett.*, 86(18):181910, 2005.

[99] J. J. Gilman. Shear-induced metallisation. *Phil. Mag. B*, 67(2):207–214, 1993.

[100] R. Peierls. The size of a dislocation. *Proc. Phys. Soc.*, 52(1):34, 1940.

[101] F. R. N. Nabarro. Dislocations in a simple cubic lattice. *Proc. Phys. Soc.*, 59(2):256–272, 1947.

[102] A. George and J. Rabier. Dislocations and plasticity in semiconductors. i. dislocation structures and dynamics. *Revue de Physique Appliquee*, 22(9):941–966, 1987.

[103] H. R. Kolar, J. C. H. Spence, and H. Alexander. Observation of moving dislocation kinks and unpinning. *Phys. Rev. Lett.*, 77(19):4031–4034, 1996.

[104] Y. L. Iunin, V. I. Nikitenko, V. I. Orlov, and B. V. Petukhov. Anomalous dislocation kink drift in germanium. *Phys. Rev. Lett.*, 78(16):3137–3140, 1997.

[105] L. Csepregi, R. P. Kullen, J. W. Mayer, and T. W. Sigmon. Regrowth kinetics of amorphous Ge layers created by ^{74}Ge and ^{28}Si implantation of Ge crystals. *Solid State Commun.*, 21(11):1019–1021, 1977.

[106] E. P. Donovan, F. Spaepen, D. Turnbull, J. M. Poate, and D. C. Jacobson. Calorimetric studies of crystallization and relaxation of amorphous Si and Ge prepared by ion-implantation. *J. Appl. Phys.*, 57(6):1795–1804, 1985.

[107] S. E. Donnelly, R. C. Birtcher, V. M. Vishnyakov, and G. Carter. Annealing of isolated amorphous zones in silicon. *Appl. Phys. Lett.*, 82(12):1860–1862, 2003.

[108] R Hill. The elastic behaviour of a crystalline aggregate. *Proceedings of the Physical Society. Section A*, (5):349, 1952.

[109] Hyoung Seop Kim. On the rule of mixtures for the hardness of particle reinforced composites. *Materials Science and Engineering A*, 289(1-2):30–33, 2000.

[110] J. S. Williams, Y. Chen, J. Wong-Leung, A. Kerr, and M. V. Swain. Ultra-micro-indentation of silicon and compound semiconductors with spherical indenters. *J. Mater. Res.*, 14(6):2338–2343, 1999.

[111] S. S. Chiang, D. B. Marshall, and A. G. Evans. The response of solids to elastic plastic indentation .1. stresses and residual-stresses. 53(1):298–311, 1982.

[112] W. H. Zachariasen. Tthe atomic arrangement in glass. *J. Am. Chem. Soc.*, 54(10):3841–3851, 1932.

[113] M. A. Paesler, D. E. Sayers, R. Tsu, and J. Gonzalez-Hernandez. Ordering of amorphous-germanium prior to crystallization. *Phys. Rev. B*, 28(8):4550–4557, 1983.

[114] R. Tsu, J. Gonzalez-Hernandez, and Fred H. Pollak. Determination of the energy barrier for structural relaxation in amorphous Si and Ge by raman scattering. *Solid State Commun.*, 54(5):447–450, 1985.

[115] J. Fortner and J. S. Lannin. Structural relaxation and order in ion-implanted Si and Ge. *Phys. Rev. B*, 37(17):10154–10158, 1988.

[116] I. D. Desnica-Frankovic, K. Furic, U. V. Desnica, M. C. Ridgway, and C. J. Glover. Structural modifications in amorphous Ge produced by ion implantation. *Nucl. Instrum. Meth. B*, 178:192–195, 2001.

[117] D. E. Polk and D. S. Boudreau. Tetrahedrally coordinated random-network structure. *Phys. Rev. Lett.*, 31(2):92–95, 1973.

[118] O. Shimomura, S. Minomura, N. Sakai, K. Asaumi, K. Tamura, Fukushim.J, and H. Endo. Pressure-induced semiconductor-metal transitions in amorphous Si and Ge. *Philos. Mag.*, 29(3):547–558, 1974.

[119] K. Tanaka. Crystallization of amorphous Ge. *Solid State Commun.*, 76(2):213–215, 1990.

[120] K. Tanaka. Amorphous-Ge under pressure. *Phys. Rev. B*, 43(5):4302–4307, 1991.

[121] M. Imai, T. Mitamura, K. Yaoita, and K. Tsuji. Pressure-induced phase transition of crystalline and amorphous silicon and germanium at low temperatures. *High Pressure Research*, 15(3):167–189, 1996.

[122] E. Principi, A. Di Cicco, F. Decremps, A. Polian, S. De Panfilis, and A. Filipponi. Polyamorphic transition of germanium under pressure. *Phys. Rev. B*, 69(20):201201, 2004.

[123] M Durandurdu and DA Drabold. First-order pressure-induced polyamorphism in germanium. *Phys. Rev. B*, 66(4):041201, 2002.

[124] B. Haberl, J. E. Bradby, M. V. Swain, J. S. Williams, and P. Munroe. Phase transformations induced in relaxed amorphous silicon by indentation at room temperature. *Appl. Phys. Lett.*, 85(23):5559–5561, 2004.

[125] B. Haberl, J. E. Bradby, S. Ruffell, J. S. Williams, and P. Munroe. Phase transformations induced by spherical indentation in ion-implanted amorphous silicon. *J. Appl. Phys.*, 100(1):013520, 2006.

[126] G. Patriarche, E. Le Bourhis, M. M. O. Khayyat, and M. M. Chaudhri. Indentation-induced crystallization and phase transformation of amorphous germanium. 96(3):1464–1468, 2004.

[127] G. Schirmer, A. Duparré, W. Heerdegen, H.-J. Kühn, A. Lehmann, W. Richter, B. Schröter, E. Hacker, and J. Meyer. Properties of thin optical Ge films related to their technology dependent structure. *phys. stat. sol. (a)*, 124(1):199–210, 1991.

[128] E. R. Weppelmann, J. S. Field, and M. V. Swain. Observation, analysis, and simulation of the hysteresis of silicon using ultra-micro-indentation with spherical indenters. *J. Mater. Res.*, 8(4):830–840, 1992.

[129] H. J. Leamy, W. L. Brown, G. K. Celler, G. Foti, G. H. Gilmer, and J. C. C. Fan. Explosive crystallization of amorphous-germanium. *Appl. Phys. Lett.*, 38(3):137–139, 1981.

[130] T. Takamori, R. Roy, and R. Messier. New noncrystalline germanium which crystallizes explosively at room-temperature. *Appl. Phys. Lett.*, 20(5):201, 1972.

[131] C. Grigoropoulos, M. Rogers, S. H. Ko, A. A. Golovin, and B. J. Matkowsky. Explosive crystallization in the presence of melting. *Phys. Rev. B*, 73(18):184125, 2006.

[132] D. Bensahel and G. Auvert. Explosive crystallization in a-Ge and a-Si: a review. *Mater. Res. Soc. Symp. Proc.*, 13:165–176, 1983.

[133] R. People and J. C. Bean. Calculation of critical layer thickness versus lattice mismatch for Ge_xSi_{1-x}/Si strained-layer heterostructures. *Appl. Phys. Lett.*, 47(3):322–324, 1985.

[134] J. J. Wortman and R. A. Evans. Young's modulus, shear modulus, and poisson's ratio in silicon and germanium. *J Appl Phys*, 36(1):153–156, 1965.

[135] D. E. Aspnes and A. A. Studna. Dielectric functions and optical-parameters of Si, Ge, GaP, GaAs, GaSb, InP, InAs, and InSb from 1.5 to 6.0 eV. *Phys. Rev. B*, 27(2):985–1009, 1983.

[136] N. Maley, D. Beeman, and J. S. Lannin. Dynamics of tetrahedral networks: Amorphous Si and Ge. *Phys. Rev. B*, 38(15):10611–10622, 1988.

[137] R. J. Kobliska, S. A. Solin, M. Selders, R. K. Chang, R. Alben, M. F. Thorpe, , and D. Weaire. Raman scattering from phonons in polymorphs of Si and Ge. *Phys. Rev. Lett.*, 29(11):725–728, 1972.

[138] David J. Oliver, Jodie E. Bradby, Jim S. Williams, Michael V. Swain, and Paul Munroe. Giant pop-ins and amorphization in germanium during indentation. *J. Appl. Phys.*, 101(4):043524, 2007.

[139] S. V. Hainsworth, A. J. Whithead, and T. F. Page. The nanoindentation response of silicon and related structurally similar materials. In R. C. Bradt, C. A. Brookes, and J. L. Routbort, editors, *Plastic Deformation of Ceramics*, page 173. Plenum, New York, 1995.

[140] P. Pirouz, R. Chaim, U. Dahmen, and K. H. Westmacott. The martensitic transformation in silicon–I experimental observations. *Acta Met. et Mater.*, 38(2):313–322, 1990.

[141] I. Zarudi and L. C. Zhang. Structural changes in mono-crystalline silicon subjected to indentation - experimental findings. *Trib. Int.*, 32:701–712, 1999.

[142] D. B. Ge, V. Domnich, and Y. Gogotsi. High-resolution transmission electron microscopy study of metastable silicon phases produced by nanoindentation. *J. Appl. Phys.*, 93(5):2418–2423, 2003.

[143] S. Ogata, J. Li, and S. Yip. Energy landscape of deformation twinning in bcc and fcc metals. *Phys. Rev. B*, 71(22):224102, 2005.

[144] Z. H. Xie, M. Hoffman, R. J. Moon, and P. R. Munroe. Deformation of a hard coating on ductile substrate system during nanoindentation: Role of the coating microstructure. *J. Mater. Res.*, 21(2):437–447, 2006.

[145] James S. Schilling. The use of high pressure in basic and materials science. *J. Phys. Chem. Solids*, 59(4):553–568, 1998.

[146] D.M. Tanner, J.A. Walraven, K.S. Helgesen, L. W. Irwin, F. Brown, N.F. Smith, and N. Masters. MEMS reliability in a shock environment. In *IEEE 39th Annual International Reliability Physics Symposium Proceedings*, pages 129–138, 2000.

[147] J.A. Walraven. Failure mechanisms in MEMS. In *Test Conference, 2003. Proceedings. ITC 2003. International*, volume 1, pages 828–833, 2003.

[148] T.F. Tan, K. Weber, and C.K.H. Dharan. Failure analysis of thermal actuators, comb drives, and other microelectromechanical elements. *J. Failure Anal. Prevent.*, 7:137–143, 2007.

[149] A. G. Evans and T. R. Wilshaw. Quasi-static solid particle damage in brittle solids – I. observations analysis and implications. *Acta Metallurgica*, 24(10):939–956, 1976.

[150] B. R. Lawn, B. J. Hockey, and S. M. Wiederhorn. Atomically sharp cracks in brittle solids: an electron microscopy study. *J. Mater. Sci.*, 15(5):1207–1223, 1980.

[151] T. B. Light. Density of ”amorphous” Ge. *Phys. Rev. Lett.*, 22(19):999–1000, 1969.

[152] J. T. Hagan. Micromechanics of crack nucleation during indentations. *J. Mater. Sci.*, 14(12):2975–2980, 1979.

[153] J. S. Field, M. V. Swain, and R. D. Dukino. Determination of fracture toughness from the extra penetration produced by indentation-induced pop-in. *J. Mater. Res.*, 18(6):1412–1419, 2003.

[154] M. Tachi, Suprijadi, S. Arai, and H. Saka. On the dislocation mechanism of amorphization of Si by indentation. *Phil. Mag. Lett.*, 82(3):133–139, 2002.

[155] R. Rabe, J. M. Breguet, P. Schwaller, S. Stauss, F. J. Haug, J. Patscheider, and J. Michler. Observation of fracture and plastic deformation during indentation and scratching inside the scanning electron microscope. *Thin Solid Films*, 469-470:206, 2004.

[156] C. M. Lepienski, M. D. Michel, P. J. G. Araujo, and C. A. Achete. Indentation fracture of a-C:H thin films from chemical vapour deposition. *Philos. Mag.*, 86(33 - 35):5397, 2006.